Modelling Novel Photovoltaic Devices

Cave, James

Award date:
2019

Awarding institution:
University of Bath

Modelling Novel Photovoltaic Devices

James Michael Cave

A thesis submitted for the degree of Doctor of Philosophy

University of Bath

Department of Physics

September 2018

DECLARATION

The material presented here for examination for the award of a higher degree by research has not been incorporated into a submission for another degree.

To my parents

He must know mathematics, for at every turn some occasion for them will present itself to him

Don Quixote, on the qualities of a knight-errant
Miguel de Cervantes
Translated by John Ormsby

Abstract

Perovskite solar cells exhibit vacancy-mediated halide motion, leading to reduced performance, inaccurate characterisation and accelerated degradation. To study vacancy motion, a model is built that solves the drift-diffusion equations for vacancies, electrons and holes across the perovskite absorber layer and both charge transport layers, all fully coupled with the Poisson equation. The model agrees with the prevalent theory that vacancies in the perovskite form Debye layers next to the interfaces with the transport layers, building regions of net charge that act to screen the electric field within the bulk of the absorber. The slow charging and discharging of the Debye layers over the course of a current-voltage scan leads to hysteresis in that measurement. The extent to which hysteresis is present depends on the alignment of the timescale of the scan with that of ion motion.

The effects of device properties and experimental protocols are mapped by sweeping over ranges of input parameters using the model. Heating is found to shift ion motion to faster timescales due to its Arrhenius nature, from which activation energies may be extracted. Experimentally obtained activation energies for various perovskites compare well to density functional theory predictions. Reducing vacancy density and recombination improves performance and reduces hysteresis but slowing the ions does not. Increasing the doping and permittivity of the transport layers improves performance, though may increase hysteresis.

Separately, Förster resonance energy transport of excitons in organic solar cells is simulated using a kinetic Monte Carlo model. Modelling shows that transfer between different materials provides a key pathway for exciton dissociation in both binary and ternary devices. The need for energy band offsets that limit photovoltage may be relaxed if an efficient pathway is present. In ternary devices, efficient transfer from the standard wide-bandgap absorber P3HT to the infra-red sensitiser DIBSq allows funnelling of excitons from the bulk of the P3HT to interfacial regions of DIBSq, improving exciton dissociation efficiency further.

Acknowledgements

I would like to take this opportunity to thank the great number of people I have worked alongside over the past four years. First to my supervisor Alison Walker for her advice, support and guidance over the duration of my PhD on all the projects I have worked. I am also grateful to Nicola Courtier, with whom I worked closely to develop the drift-diffusion model, and to Jamie Foster and Giles Richardson for their work on that project.

Many thanks go to Krishna Feron for arranging my numerous visits to CSIRO and the University of Newcastle in Australia, and for his help and guidance while I was there. I also gratefully acknowledge CSIRO and the SuperSolar Hub for financial support for these visits, and to Chris Fell and Greg Wilson at CSIRO and Paul Dastoor at the University of Newcastle for providing me work space and help at their institutions.

With regard to the experiments supporting this work, I again thank Krishna for all the experimental measurements in the organics chapter as well as his leadership of that project. I thank Tim Jones at CSIRO for his leadership of the experimental work obtaining the large set of J-V measurements required to extract activation energies for the perovskite cells, as well as performing the measurements for the $MAPbI_3/SnO_2$ device. I also thank Isabelle Blakborn for the J-V measurements of the $MAPbI_3/TiO_2$ device during her time at CSIRO. Thanks also to Dibyajyoti Ghosh for providing density functional theory calculations for those activation energies.

Finally, I would like to extend my sincere gratitude to Wolf, Dibs, Smithbot and Ria for group ale, stout, cider and wine consumption sessions respectively and to CDT-PV cohort 1 for an entertaining start to my PhD.

Publications

Work done as part of this thesis has led to a number of publications, detailed below.

1. K Feron, **JM Cave**, MN Thameel, C O'Sullivan, R Kroon, MR Andersson, X Zhou, CJ Fell, WJ Belcher, AB Walker and PC Dastoor, 2016. Utilizing energy transfer in binary and ternary bulk heterojunction organic solar cells, *ACS Appl. Mater. Interfaces*, 8 (32), 20928. [1]

2. SEJ O'Kane, G Richardson, A Pockett, RG Niemann, **JM Cave**, N Sakai, GE Eperon, HJ Snaith, JM Foster, PJ Cameron, AB Walker, 2017. Measurement and modelling of dark current decay transients in perovskite solar cells, *J. Mater. Chem. C*, 5 (2), 452. [2]

3. **JM Cave** and AB Walker, 2018. Modelling hysteresis in perovskite solar cells, Chapter 10 *Photovoltaic Modeling Handbook*, ed. MF Müller, pp. 267-278, Scrivener Publishing.

4. NP Holmes, M Marks, **JM Cave**, K Feron, M Barr, A Fahy, A Sharma, X Pan, ALD Kilcoyne, X Zhou, DA Lewis, MR Andersson, C Müller, J van Stam, AB Walker, E Moons, WJ Belcher, PC Dastoor, 2018. Engineering two-phase and three-phase microstructures from water-based dispersions of nanoparticles for eco-friendly polymer solar cell fabrication, accepted into *ACS Chem. Mater.*

5. **JM Cave**, NE Courtier, IA Blakborn, TW Jones, D Ghosh, KF Anderson, L Lin, AA Dijkhoff, GJ Wilson, K Feron, JM Foster, G Richardson, AB Walker, 2018. How to identify and fix losses from ion motion in perovskite solar cells, unpublished.

6. NE Courtier, **JM Cave**, JM Foster, AB Walker, G Richardson, 2018. How transport layer properties affect perovskite solar cell performance: insights from a coupled charge transport/ion migration model, accepted into *Energy Environ. Sci.*

7. J Idígorasa, L Contreras-Bernala, **JM Cave**, NE Courtier, Á Barranco, A Borras, JR Sánchez-Valencia, JA Anta, AB Walker, 2018. The role of surface recombination on the performance and hysteresis of perovskite solar cells: effect of morphology and crystalline phase of TiO_2 contact, accepted into *Adv. Mater. Interfaces.*

Contents

1 Fundamentals of solar cells **15**

2 Introduction **21**
2.1 History . . . 22
2.2 Ion motion . . . 27
2.3 Motivation . . . 31

3 Drift-diffusion model **33**
3.1 Statement of problem . . . 33
3.2 Drift and diffusion . . . 35
3.3 System of equations . . . 36
3.4 Method of Lines . . . 42
3.5 Solver . . . 45
3.6 Stiffness, ill-conditioning and grid choice . . . 48
3.7 Implementation . . . 52
3.8 Summary . . . 55

4 How ion motion controls current, loss and performance **57**
4.1 Steady-state . . . 57
4.2 Current-voltage curve . . . 58
4.3 Quantifying dependence on scan rate . . . 62
4.4 Dependence on temperature – speeding the ions up . . . 65
4.5 Shifting the timescale or reducing loss? . . . 76
4.6 Ion density as a function of temperature . . . 84
4.7 Preconditioning and inverse hysteresis . . . 89
4.8 Conclusion . . . 92

5 Kinetic Monte Carlo Modelling of Energy Transport in Organic Solar Cells **95**
5.1 Introduction . . . 95
5.2 Kinetic Monte Carlo model . . . 103
5.3 Impact of heterotransfer in a binary BHJ . . . 108
5.4 Exciton dissociation in a ternary organic system . . . 111
5.5 Conclusion . . . 113

Chapter 1

Fundamentals of solar cells

Since the industrial revolution, our lives have been powered by fossil fuels. It has since been recognised that large-scale consumption of these resources is unsustainable in the long-term due to finite reserves and the deleterious health and environmental impacts of the combustive waste products. Seeking out practical alternative energy sources, that are ideally both renewable and clean, is thus a major goal for humanity.

Solar energy is becoming increasingly more popular as one such method of producing electricity. As the sun is expected to exist for some time to come, and is going to shine on the earth whether we use that energy or not, solar is certainly renewable. Without any emissions or waste products, it is also clean. For most applications, though, solar cannot compete with fossil fuels on price and convenience – yet.

Silicon based systems have dominated the solar market since its inception. Silicon modules are somewhat costly and, while the cost of solar power has plummeted since the 1960's and has benefited greatly from the economies of scale in recent years, a limiting factor in driving down prices further is the cost and difficulty of refining silicon to the required 99.9999% purity [3]. This has naturally led science and industry to investigate the use of other materials that may be produced more cheaply and easily. Here we consider two such classes of materials: lead halide perovskites and organics.

This chapter consists of a brief overview of the basic underlying principles of photovoltaic (PV) technologies, common to both materials. Chapters 2–4, comprising the main body of work, concerns the phenomenon of ion motion within perovskite solar cells (PSCs). Perovskites offer efficiencies rivalling that of silicon, for use either as their own PV technology or (more likely) together with silicon in tandem devices. The dynamics of both electronic and ionic motion are studied via drift-diffusion modelling, to understand the anomalous behaviour of PSCs and make predictions to help guide future work in the field. Chapter 5 concerns the dynamics of exciton diffusion in organic solar cells (OSCs). Organics offer a low cost alternative to traditional PV, with particularly appealing possibilities in niche applications such as flexible devices. Consideration of exciton transport is a crucial part of designing an efficient OSC, which we treat using a kinetic Monte Carlo (KMC) model.

The working principle of all solar cells is the photovoltaic effect. Upon excitation by an incoming photon, an electron in the valence band (VB) of a semiconductor is promoted across the bandgap (E_{G}) into the conduction band (CB) leaving behind a

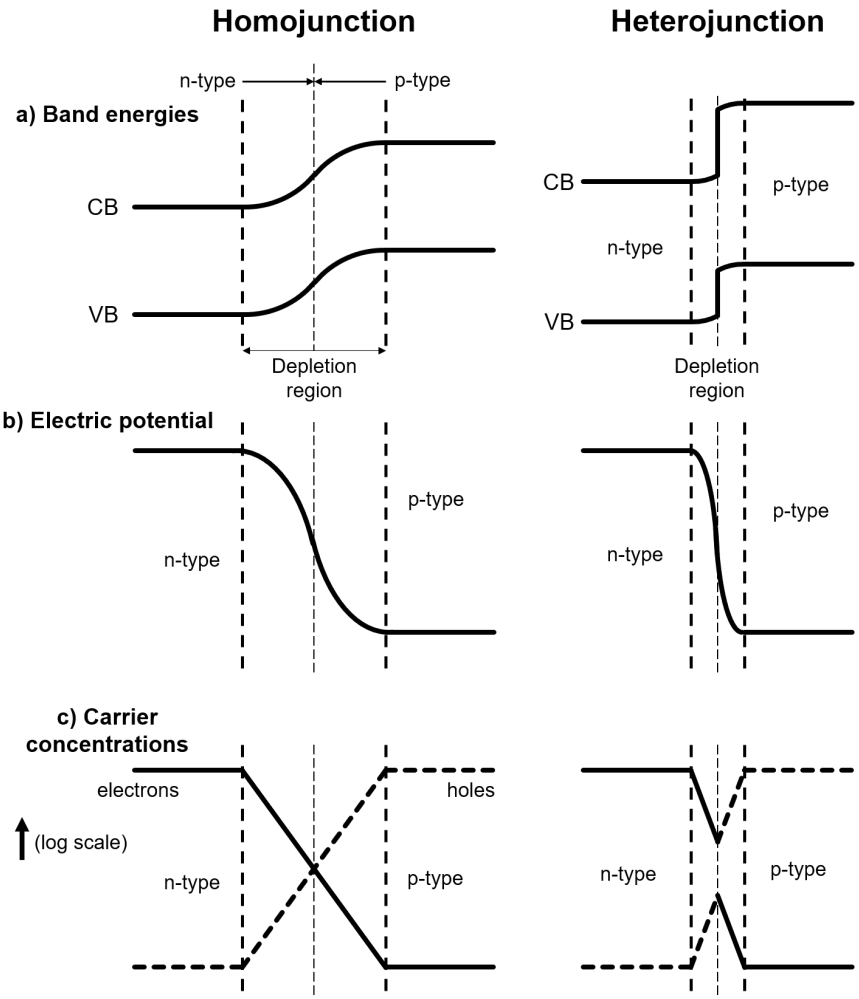

Figure 1.1: (a) Band energies, (b) electric potential and (c) carrier concentrations for (left) an n-p homojunction and (right) a heterojunction.

hole. The coulombically bound electron and hole are then separated from each other via an electric field before they can recombine and are transported to and collected by electrodes. This produces a potential difference between the electrodes, which can be used to do work.

The electric field is produced in one of two ways, depending on the cell. In a homojunction device, layers of the same material with different doping are placed together. Silicon cells, like most inorganic devices, utilise a p-n or p-i-n homojunction to split the photogenerated charge carriers. Contact between an n-doped and a p-doped region leads to the formation of a low carrier density depletion region at the boundary of the two doped regions, with an electric field (the built-in field) pointing from the n-type to the p-type [4]. Electron-hole pairs photogenerated by absorption in the depletion region will be separated by this force, with holes driven into the p-type region and electrons into the n-type region. The charges can then be extracted by the electrodes and fed into an external circuit. The difference in electric potential between one side of the depletion region and the other is called the built-in voltage, V_{bi}. Some important properties of a homojunction are given in the left column of Figure 1.1.

Alternatively, two layers of different materials can be used to form a hetero-

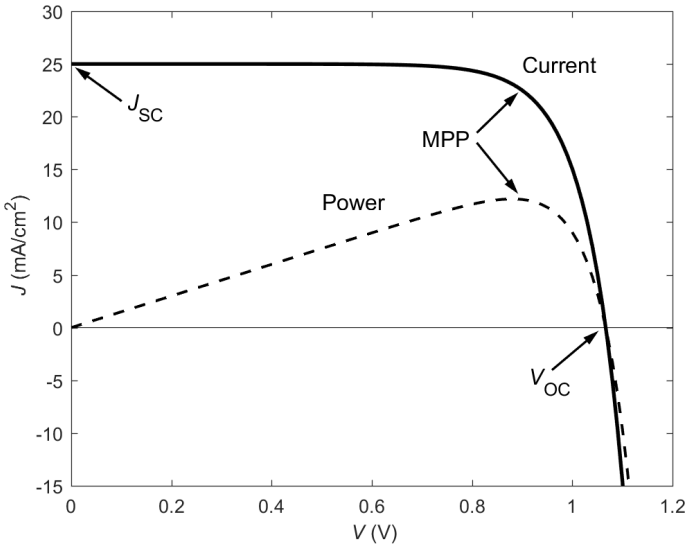

Figure 1.2: A typical J-V curve (solid line). The generated power, the product of J and V, is given as a dashed line. The short-circuit current J_{SC}, open-circuit voltage V_{OC} and maximum power point MPP are labelled.

junction. Both perovskite and organic PV devices employ heterojunctions. At the interface, it is energetically favourable for electrons in the p-type material to transfer to the n-type but not the other way. Similarly for holes, the band offset makes it favourable for holes to transfer from n-type to p-type but not back. A diagram of a heterojunction is shown in the right column of Figure 1.1. The electric field is set up across the device from the difference in band energies.

Perhaps the most important measurement one can make of a solar cell is the J-V curve. J is the current density, or current per unit area of device, as a function of applied voltage V. The conventional unit is mA/cm^2, with most solar cells having current densities in the tens in this unit. The J-V curve is often referred to as the current-voltage characteristic, although strictly this is the I-V curve. It is almost always more useful to normalise the I-V by area of device, as a device twice as large will usually produce twice as much current, so the terms are used interchangably. From the J-V curve, most of the important measures of cell performance can be extracted. A typical J-V curve is shown in Figure 1.2.

Thinking of the solar cell connected up to a load, the resistance of the load determines the potential difference that will develop between the electrodes and also the current driven through the external circuit. In the case where there is zero load resistance, electrons flow unimpeded from one electrode to the other. This situation, known as short circuit, produces the maximum possible photocurrent density, the short-circuit current J_{SC}, although zero potential difference. In the other extreme, where there is infinite resistance between the electrodes, electrons are unable to move from one electrode to the other via the external circuit. Electrons are removed from the cathode (equivalent to hole extraction from the device by the cathode) and pile up in the anode, causing a field cancelling out the built-in voltage and suppressing charge collection. Eventually the rate of charge carrier collection by the electrodes balances with the leakage of carriers from the electrodes back into the cell. This produces the greatest possible photovoltage between the electrodes, the open-circuit voltage V_{OC}, though no current.

In both of these cases no work can be done as the product of J and V is zero. Work can be done by applying a load with a finite, non-zero resistance across the device. By varying the resistance of the load, one can obtain a plot of current against applied voltage. Experimentally the J-V curve is measured by applying a voltage V_{ap} across the device in opposition to the photovoltage, and sweeping over a range of voltages to simulate a range of loads quickly. As we are interested in the photocurrent produced by the cell, it is conventional to plot the value of the current density measured in the opposite direction to the applied voltage. This results in a current-voltage characteristic that is upside-down to one obtained if defining J in the same direction as V, as is usual in other fields. The best power output occurs when the product of voltage and current is maximum, known as maximum power point (MPP). PV systems have a charge controller component that ensures that the load applied to the solar modules keeps them operating near MPP. For a device where the voltage and current at MPP are V_{max} and J_{max} respectively, the power conversion efficiency (PCE or η_{PC}) is given by

$$\eta_{\text{PC}} = \frac{V_{\text{max}} J_{\text{max}}}{P_{\text{inc}}} \tag{1.1}$$

where P_{inc} is the power incident on the cell. A final measure of cell performance is the fill factor (FF), given by

$$\text{FF} = \frac{V_{\text{max}} J_{\text{max}}}{V_{\text{OC}} J_{\text{SC}}}. \tag{1.2}$$

Fill factor is basically a measure of how square the J-V curve is. Low FF is indicative of resistive losses.

It is clear from the above equations that we would like to maximise J_{SC} and V_{OC} in order to get the best possible PCE. Naturally, there is a limit to how well we can do this. The highest possible obtainable efficiency from a purely thermodynamic viewpoint is the Carnot efficiency $\eta_{\text{c}} = 1 - T_c/T_h$. Taking the surface temperature of the sun, 5778 K, as the hot source and 300 K as the temperature of cell as the cold sink, we find $\eta_{\text{c}} = 94.8\%$. However, how solar cells convert light to electric power leads to a far more restricting limit.

When a photon is absorbed, it promotes an electron in the valence band to the conduction band. However, the minimum possible energy photon capable of doing this is one with an energy of exactly the bandgap E_{G}, taking an electron at the valence band maximum (VBM) to the conduction band minimum (CBM). Any photons with energy of less than E_{G} cannot be absorbed, as an electron in the VB would be promoted to a forbidden energy within the bandgap. Therefore, energy carried by photons with energies below E_{G} is unavailable. Furthermore, when a photon with energy in excess of the bandgap is absorbed, the electron quickly drops down through the energy levels until it reaches the CBM. This process is known as thermalisation, as the lost energy is released as heat. Due to the effective continuum of energy states within the CB, this occurs on the timescale of femtoseconds, many orders of magnitude faster than the electron can be extracted from the device. Accordingly, any energy above E_{G} is also unavailable.

Together, this means we can obtain at best E_{G} of energy from photons with at least this energy, and no energy from other photons. The maximum possible PCE

is then

$$\max \eta_{\mathrm{PC}}(E) = \frac{E_{\mathrm{G}} \int_{E_{\mathrm{G}}}^{\infty} I(E)\, \mathrm{d}E}{\int_{0}^{\infty} E\, I(E)\, \mathrm{d}E} \tag{1.3}$$

where $I(E)$ is the number of photons with energy E incident on the device. Due to atmospheric effects, $I(E)$ depends on position. The spectrum of sunlight just above the Earth's atmosphere is known as air mass 0, or AM0, while the spectrum at sea level when the sun is directly overhead is AM1. AM1.5, corresponding to the solar irradiation for the USA, is the standard $I(E)$ spectrum used in photovoltaics.

The photocurrent produced by a PV cell depends on how many photons are absorbed. Photovoltage depends on the size of the bandgap, due to E_{G} being the difference in energy between conduction and valence bands. If E_{G} is extremely small, virtually all photons will be absorbed, giving a large current. Almost all of this energy is thermalised away, so the voltage produced is very small. For a very large E_{G}, each absorbed photon gives a large amount of energy, resulting in a very large photovoltage. However, very few photons have enough energy to be absorbed, resulting in a very small current. Much like the tradeoff between voltage and current in determining the maximum power point, a larger bandgap gives better a voltage at the expense of current. The maximum possible efficiency for a solar cell as a function of absorber layer bandgap is called the Shockley-Queisser (SQ) limit. The ideal bandgap for the AM1.5 spectrum, maximising the product of bandgap and absorbed photons, is for a bandgap of about 1.34 eV with a maximum PCE of about 33.7% [5].

Chapter 2

Introduction

Perovskites are a class of materials that over the last decade have shown real potential to revolutionise photovoltaics. Generally, perovskites are the class of materials with the crystal structure of calcium titanium oxide, $CaTiO_3$, and chemical formula ABX_3. Named after the mineralogist and nobleman Lev Perovski, the prototypical perovskite was first discovered by Gustav Rose in 1839 in the Ural Mountains of the Russian Empire. A perovskite solar cell employs a semiconductor with the perovskite structure as the light-absorbing active layer. The A site cation is typically a unipositive organic molecule such as methylammonium ($CH_3NH_3^+$ or MA) or formamidinium ($HC(NH_2)_2^+$ or FA), or caesium to produce a purely inorganic perovskite. Lead is virtually always used as the B site cation, although other dipositive ions such as tin have been investigated. The X anion is a halogen ion, typically iodide or bromide. High performance cells usually feature perovskites with a mixture of ions for both the A and X sites. An illustration of the perovskite ABX_3 structure is given in Figure 2.1.

Perovskite solar cells offer a number of significant advantages that make them particularly attractive for photovoltaic applications. Manufacturing of the perovskite film itself is relatively simple; the perovskite can be solution processed at comparatively low temperature and then deposited with a variety of techniques including blade coating, slot-die coating, spray coating and inkjet printing [6]. Combined with the low cost of the precursor materials, PSCs have potentially low production costs on an industrial scale. This contrasts with silicon, which has a relatively expensive high temperature purification step. Through engineering the composition of the perovskite, such as by employing a mixture of halide species on the X sites, the bandgap and absorption spectrum can be tuned. Certainly the main allure arises from the astonishing rise in world record PCE, from 3.8% in the seminal paper from 2009 [7] to 20.1% in 2014 [8]. The current record PCE of 22.7% [8, 9] has reached that of commercialised technologies such as CdTe and CIGS and is superior to the most widely deployed technology, multicrystalline silicon. PSCs have also shown excellent performance in tandem with silicon cells, with performance of 25.2% achieved so far [10].

This chapter first details the rise of perovskite photovoltaics from nothing to key contender, with an overview of the current state of the field. Ion motion within perovskite films and its effect on real world devices is then discussed. Finally, the motivation for this work and its contribution to the field is explained.

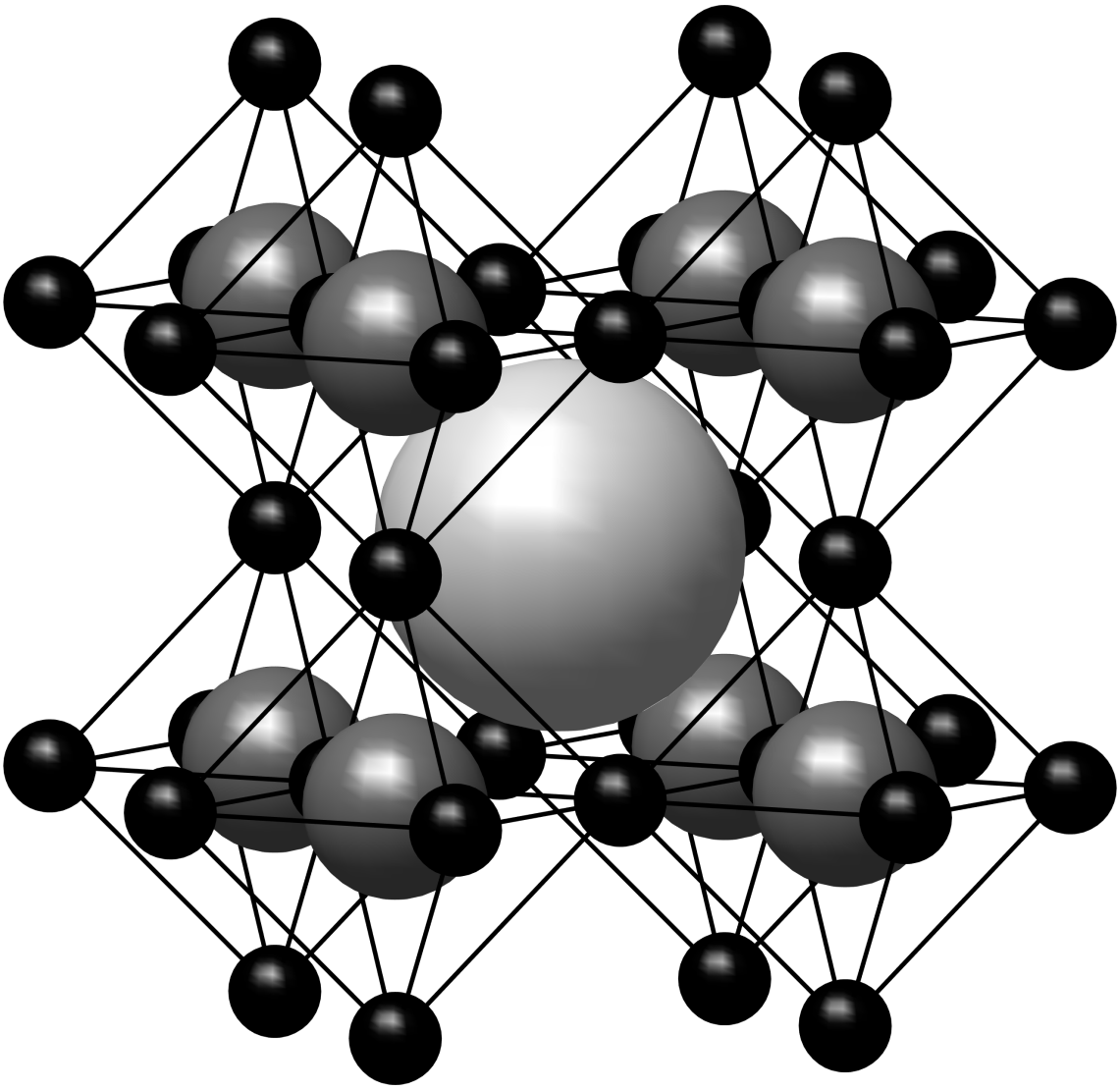

Figure 2.1: Perovskite crystal structure, with A cation (large, light sphere), B cation (medium-sized, dark spheres) and halides (small, black spheres). Halides are conventionally drawn connected with edges to form octahedra. The A site may be a single atom as presented, or a small molecule.

2.1 History

PSCs were born from the earlier technology of dye-sensitised solar cells (DSSCs) [11]. In this design, shown in Figure 2.2a, a scaffold of TiO_2 is coated with a thin layer of absorber material, which is in turn surrounded in a sea of liquid electrolyte. Light is absorbed by the dye, generating a bound electron-hole pair known as an exciton. Organic materials, including photovoltaically active dyes, are excitonic, requiring a heterojunction to separate (dissociate) the electron and hole. Due to the thin dye layer, the electron easily transfers to the TiO_2 and the hole to the electrolyte. The scaffold-sensitiser arrangement is required such that there is a thick enough layer of dye to absorb a significant amount of light, while also maintaining a thin dye thickness on a local level for carrier transfer to the transport materials. In this setup, many micrometres of scaffold-sensitiser architecture is required for a reasonable fraction of incident light to be absorbed.

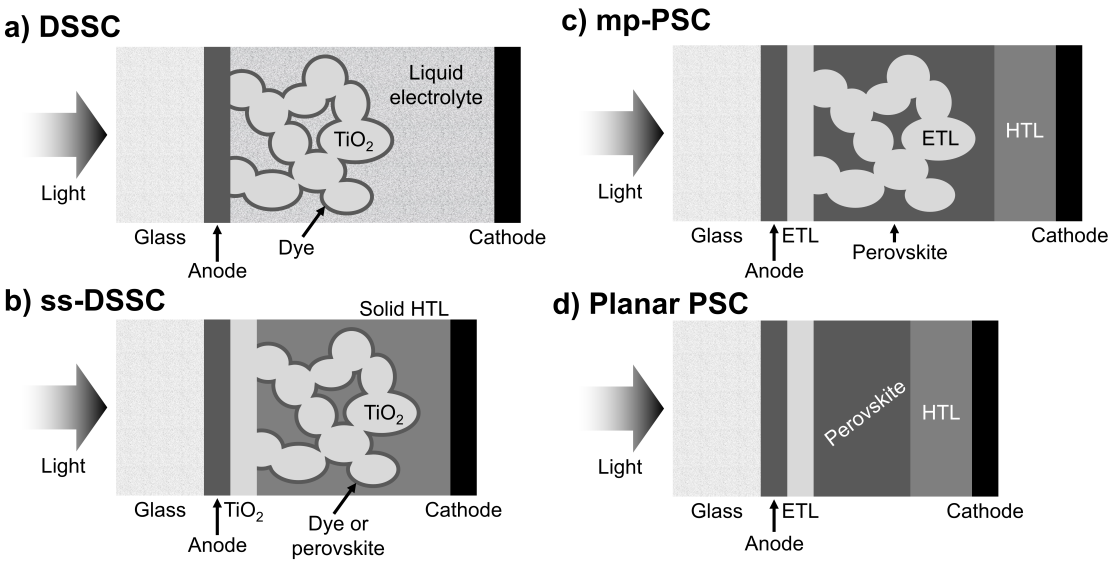

Figure 2.2: Evolution of perovskite solar cells (PSCs) from dye-sensitised solar cells (DSSCs). (a) A DSSC consists of a thin absorber coated onto an electron-transporting scaffold within a sea of hole-transporting liquid electrolyte. (b) A solid-state DSSC (ss-DSSC) swaps the liquid electrolyte for a solid HTL. Early PSCs kept the scaffold-sensitiser morphology, using perovskite as the sensitiser. (c) When it was realised that perovskite conducts both electrons and holes extremely well, the sensitiser morphology was quickly abandoned in favour of the perovskite completely permeating the mesoporous (mp) scaffold. (d) When the scaffold was found to be unnecessary, a planar design was adopted. Note this is not an exhaustive list of cell designs.

Functional DSSCs were first reported in 1991 and broke 10% power conversion efficiency by 1997, but PCEs have largely stagnated since then [8]. The current world record efficiency stands at 11.9%. The use of the liquid electrolyte leads to poor stability [12], and freezing and expansion of the electrolyte often results in catastrophic leakage [13]. In addition, the use of rare metals, such as platinum, as electrodes has kept costs high [14]. Consequently, DSSCs have not achieved widespread commercial use. A menagerie of unlikely materials can function as the dye, such as the juice from crushed berries. This makes DSSCs a popular technology for outreach purposes.

In 2009, methylammonium lead iodide ($MAPbI_3$) was reported for the first time as a sensitiser for a DSSC by Kojima et al. [7] The device exhibited just 3.8% PCE, and the perovskite degraded due to corrosion from the liquid electrolyte within a few minutes. The high open-circuit voltage of the cell and attractive bandgap and very high absorptivity of the perovskite made further study appealing. By 2011, a PCE of 6.5% was achieved for a perovskite DSSC [15].

At the same time, efforts were being made to replace the liquid electrolyte with a solid hole transporter, shown in Figure 2.2b. However, it was found that with the hole conductor spiro-OMeTAD the best efficiency was achieved for a TiO_2-dye thickness of only 2 µm [16]. This was thought to be due to the low charge mobility of spiro or the ability of the spiro to infiltrate the scaffold [13]. However, scaffolds of just a micron or two were not thick enough to absorb a significant proportion

of incident light using existing dyes. It thus became clear that dyes with greatly increased absorptivity were required to properly exploit the solid state (ss-DSSC) design.

Combining these insights, Lee et al. [17], working with Kojima, constructed an ss-DSSC in 2012 using $MAPbI_2Cl$ as the dye with TiO_2 and spiro as the electron-transporting scaffold and hole transport respectively. Due to the high absorptivity of the perovskite, a film as thin as 700 nm is required to ensure proper functionality of the spiro layer while still absorbing most incident light. This device yielded a PCE of 7.8%. Strangely, when the TiO_2 scaffold was replaced by insulating Al_2O_3, keeping TiO_2 as a planar electron transport layer, the PCE improved to 10.9%. Specifically, the J_{SC} remained the same, while V_{OC} improved by over 0.2 V. As the TiO_2 scaffold was intended to transport electrons, one would have expected the cell to be considerably worse, not better. Instead, the unchanged J_{SC} showed that electrons must have have been conducted through the narrow layers of perovskite directly to the planar TiO_2 ETL more efficiently that through the TiO_2 scaffold. This proved that $MAPbI_2Cl$ is an excellent electron conductor.

As a *conductive* scaffold was found to be unnecessary, the need for a scaffold at all was called into question. The other job of the scaffold, besides conducting electrons, was to provide a very large surface area between the absorber and transport layers for efficient charge separation. While the Al_2O_3 architecture removed the large surface area between absorber and ETL, even an inert scaffold provided for a large interface between absorber and HTL. This would still allow for efficient exciton splitting at the perovskite/HTL interface if required, and for reasonably efficient hole conduction within the spiro. Removing the scaffold completely results in a planar PSC, shown in Figure 2.2d, with flat layers of ETL, perovskite and HTL.

Two further properties of the perovskite determined if the scaffold was needed. First, the value of the exciton binding energy E_B. The exciton binding energy is the energy required to split a bound electron-hole pair. If E_B is significantly more than k_BT then excitons are tightly bound, and a heterojunction is required to split them. These materials are termed excitonic. Conversely, if the binding energy is less than k_BT, then the energy from lattice vibrations (phonons) is sufficient to spontaneously split excitons into free charge carriers. These materials are known as non-excitonic. To work well in a planar configuration, with comparatively small interfacial areas of the absorber with the transport layers, perovskite needed to be non-excitonic. The other property determining the necessity of the scaffold is how well perovskite can conduct holes. Once free electrons and holes are produced within the absorber, both types of carrier need to transport efficiently to the transport layers for a complete circuit to be made. Lee et al. had also constructed a planar $TiO_2/MAPbI_2Cl$/spiro PSC, with a 150 nm thick perovskite layer. With a low PCE of 1.8%, this was inconclusive as to whether the reduced efficiency was from the lack of scaffold or from some other factor like poor film quality.

The next year, 2013, Liu et al. [18] produced a planar PSC with a 330 nm thick perovskite layer with a reported efficiency of 15.4%. This paper decisively showed both that perovskite is an excellent hole conductor and that it is non-excitonic. If exciton splitting was only occuring at the interfaces of the perovskite with the transport layers, a PCE of only a few percent could be expected. Most excitons in a planar configuration will be generated within the bulk of the layer, and recombine before reaching an interface to be split. While excitons are in general mobile parti-

cles, typical diffusion lengths are tens of nanometres at best. As neutrally-charged particles, electric fields cannot be used to channel them towards interfaces. For the device to exhibit such a high PCE, excitons must be spontaneously splitting within the bulk. Once free of each other, both types of free carriers are able to travel the hundreds of nanometres required to reach their respective transport layers, demonstrating efficient transport of both carriers. A theoretical value for $E_B \approx 5$ meV came in 2014 [19]. Quantitative evidence was eventually published by two separate groups in 2015 [20, 21]. Both found the binding energy at 300 K to be approximately 2 meV, far smaller than $k_B T = 25.9$ meV.

This finding opened the door to planar PSCs and cells incorporating a planar perovskite aspect. A mesoporous PSC, illustrated in Figure 2.2c, uses an ETL consisting of a compact (planar) layer with a mesoporous scaffold. Perovskite is added to completely fill the pores and also form a compact layer on top. A planar HTL finishes the design. The overwhelming majority of devices produced now are either mesoporous or planar PSCs. Planar devices, as in Figure 2.2d, are easier to make, due to avoiding the need to construct a complex mesoporous layer using high-temperature sintering [22], though mp-PSCs tend to have slightly higher efficiencies. The current world record cell employs a mesoporous TiO_2 layer [9].

While the sharp increase in record PCE may have driven the field initially, there is only so long this can be sustained. In the first five years of the field perovskite rocketed from 3.8% in 2009 to 20.1% in 2014. In the four years since then, the record now stands at 22.7% [8]. Of course, there is only so much further efficiencies can improve as the Shockley-Queisser limit means even a perfect cell cannot surpass 33.7%. Even the very best inorganic PV technology, thin-film gallium arsenide (GaAs), has 'only' reached 28.8%, so it is very unlikely that perovskite will get above the mid-twenties. The challenge now to bringing perovskites into widespread use is to maintain high efficiency while improving stability, scaling-up cell area and driving down material and maufacturing costs. Producing PSCs on an industrial scale is currently possible using a variety of techniques, including roll-to-roll compatible methods, although achievable PCEs on the module scale remain poor (percentages in the low teens) for a commerical technology [23, 24, 25]. The use of costly precious metals as back electrode and even more costly spiro-OMeTAD as HTL means PSCs remain expensive. A cost analysis by Chang et al. [26] notes that with current technology a module PCE of at least 20% and lifetime of at least 20 years would directly compete with silicon and CdTe PV. As the price of silicon PV continues to fall, the required standard will only increase.

With regard to stability, significant advances have been made from the early days. Perovskites are prone to degradation by water, heat, oxygen and, most embarassingly, light. PSCs have the dubious distinction of being the only technology on the NREL Best Research-Cell Efficiencies chart to be qualified as not-stabilised. The lifetimes of modern perovskite devices are difficult to determine, as journal reports usually do not give this information. Generally though, the ballpark figure for the state-of-the-art lifetime is a few months [27]. A mass-manufactured silicon module has a typical lifetime of over a quarter of a century.

Degradation under illumination alone was found to be caused by UV light generating holes within the TiO_2 [28]. This can be solved by using a UV filter, doping with Al [29], adding a layer of Sb_2S_3 [30] or simply by not using a TiO_2 ETL [31]. Water is well known to reduce efficiency [32] and break down perovskites back into

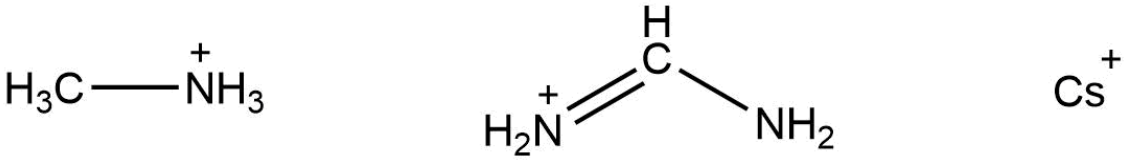

Figure 2.3: The most popular A-site cations: methylammonium, formamidinium and caesium.

its precursors. For example, $MAPbI_3$ breaks down into MAI and PbI_2 [33]. Oxygen that has infiltrated the perovskite, either during fabrication or by diffusion through the outer layers of the device, is readily ionised by incident light into the O_2^- superoxide species that degrades the perovskite [34]. Superoxide formation is not prevented by protecting the device from UV radiation.

Encapsulation of the perovskite, from all layers of the device, is the main avenue of research for protecting the cell from water and oxygen [27], and also UV light depending on the materials used. Bella et al. [35] coated the front of their devices with luminescent photopolymers that formed a hydrophobic barrier to protect from water, which also absorbed UV and re-emitted in the visible. As the re-emitted photons were of a wavelength where the perovskite has higher absorptivity, this boosted performance of the cell while also reducing degradation. Teflon has been used effectively as a hydrophobic coating for the back surface [36]. Some electron and transport layers are better than others at preventing water infiltration to the perovskite, with inorganic layers being generally better [37] and small organic molecules like spiro especially bad [38]. Heat can act to accelerate other degradation pathways, especially moisture-induced breakdown [39]. Incorporating monolayers of perovskite, known as 2D perovskite, has been found to offer some protection from heat related stress [40]. Performance decline from temperature cycling between 10 and 50 °C remains a serious issue, as this is a typical variation experienced by a PV active layer over the course of a day [41].

The main research interest in perovskites is now focused on tackling these problems, especially through new perovskite formulations and transport layers. In the standard PSC architecture, light enters the device through a glass window, passes through the front electrode and the ETL and is then absorbed by the perovskite. The HTL and back electrode complete the stack. A good choice of electron transport layer (ETL) has a conduction band (CB) energy slightly lower than that of the perovskite but a valence band (VB) energy considerably lower than that of the perovskite. In this way, electron extraction is energetically favourable but hole extraction is very unfavourable. Likewise, a good choice of hole transport layer (HTL) has a slightly higher VB energy and a considerably higher CB energy than the perovskite. Additionally, the front transport layer (usually the ETL) needs a large bandgap to transmit the AM1.5 range through to the absorber. Inverted devices with organic transport layers have also been produced, where the window layer that light passes through is the HTL.

With regards choice of perovskite, a massive variety of formulations have been tried. The three popular cations are methylammonium $CH_3NH_3^+$, formamidinium $HC(NH_2)_2^+$ and caesium Cs^+, depicted in Figure 2.3. The popular halides are iodide I^- and bromide Br^-. Lead Pb^{2+} is the only B site cation to yield a high performance perovskite to date, although alternative B site ions such as germanium and tin are

under investigation [42].

For a simple perovskite, with a single ion for each of A, B and X in ABX_3, whether a perovskite structure can form depends on the relative size of the ions. The Goldschmidt tolerance factor, defined as

$$\alpha = \frac{r_A + r_X}{\sqrt{2}\,(r_B + r_X)} \tag{2.1}$$

where r_I is the radius of ion I, needs to be in the range of about 0.8 to 1 [43, 44]. This rule limits the permutations of perovskite that can form.

In practice, simple ABX_3 perovskites tend to be unsuitable due to poor stability. These problems are overcome by employing a mixture of ions for one or more of A, B and X. For best results, mixed-cation lead mixed-halides are used as the active layer. The world record cell employs a $(FAPbI_3)_{0.95}(MAPbBr_3)_{0.05}$ [9]. Typically, one cation forms the majority of A sites with another cation in small quantities. For example, use of 10% Cs^+ or Rb^+ has been found to reduce lattice vibrations in $FAPbI_3$, improving stability and performance [45]. Incorporation of Cs^+ into $FAPbI_3$ has been found to make the bandgap indirect, reducing recombination [46]. $MAPbI_3$ is likewise stabilised by substitution of up to 5% of the cation azetidinium $(CH_2)_3NH_2^+$ [47].

2.2 Ion motion

A major problem in PSCs is pronounced hysteresis in the J-V curve, where the measured current density J depends not just on the applied voltage V_{ap} at the time but also on previously applied voltages. As J-V curves are usually measured by sweeping over a range of voltages quickly, this poses an obvious problem in obtaining reliable and reproducible measures of cell performance. J-V curves tend to improve after the device is held at or above the open-circuit voltage V_{OC} and then swept down to short circuit (known as reverse scan or down scan) compared to starting at or below short circuit and sweeping up (known as forward scan or up scan). This sensitivity of device characteristics to the device history led to concern in the perovskite research community towards the trustworthiness of published measurements as it become common practice to precondition devices at high voltage before measuring the J-V curve and reporting only the better performing reverse scan.

Originally, three theories came to prominence to explain hysteresis [48]. First, trapping and detrapping from defect sites at grain boundaries and at the edges of the perovskite film provides a source and sink of carriers that can add or subtract from the measured current. Traps certainly do affect the J-V characteristics by providing extra pathways for carrier recombination. However, to explain hysteresis they would have to behave in such a way that charges are detrapped when the voltage is decreasing, causing an increase in the cell current, and charges are trapped when the voltage is increasing, with a consequent decrease in cell current. A further argument against this attribution is that hysteresis is present for J-V scans performed over the timescale of minutes or even hours, whereas trapping and detrapping takes place on the carrier timescale of nanoseconds and faster. Sustaining the measured change in current over such a time would require such a large trap density that it is difficult to see how perovskites could function at all as a PV active layer, let alone with the excellent performance they demonstrate. Capacitance based explanations

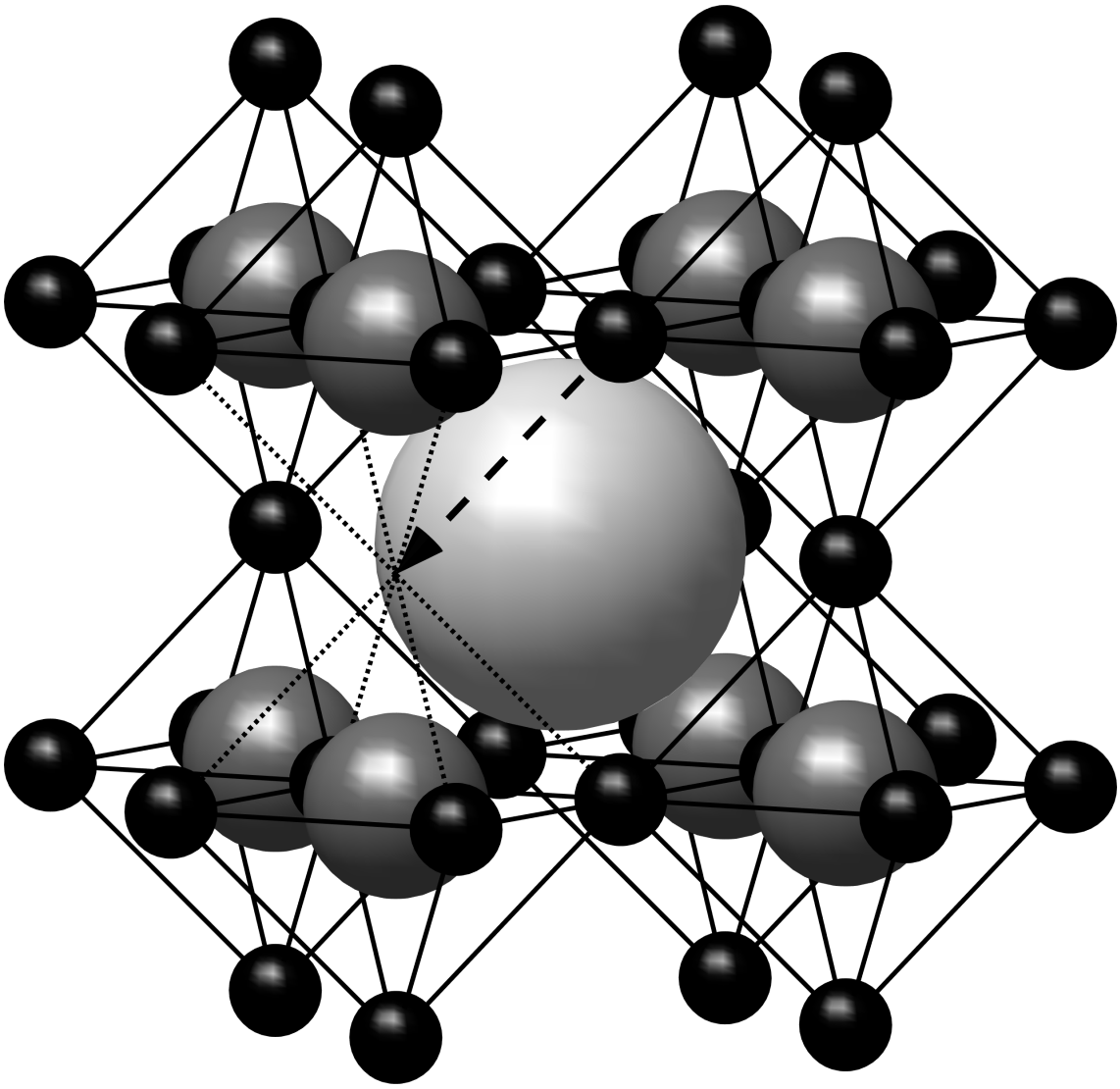

Figure 2.4: Illustration of halide ion motion. A site on the halide sublattice is vacant, depicted by dotted lines connecting to neighbouring halides. A halide can hop from a neighbouring site to the vacancy, shown by the dashed arrow. Note the hopping path is curved [51], not a straight line as illustrated here.

for the time dependent and frequency dependent PSC response also need to allow for the large geometric capacitance of the electrodes [49].

Another possibility floated was ferroelectric polarisation from alignment in the orientation of the dipolar ions on the A site, e.g. methylammonium, MA, in $MAPbI_3$. Dipolar molecules are free to rotate on the A site, and are influenced by electric fields. This suggestion has been ruled out by the presence of hysteresis in $CsPbI_3$ devices, a perovskite without a polar space group, as well as conductance measurements in $MAPbI_3$ demonstrating that the frequency dependence of the hysteresis is not characteristic of a ferroelectric response [50].

The remaining explanation, which now enjoys wide consensus in the field, is the motion of ions within the perovskite film. The perovskite films used in PSCs are extraordinarily soft [45]; as the perovskite is processed from solution, this is not entirely surprising. The formation energy for a Schottky defect in $MAPbI_3$ has been

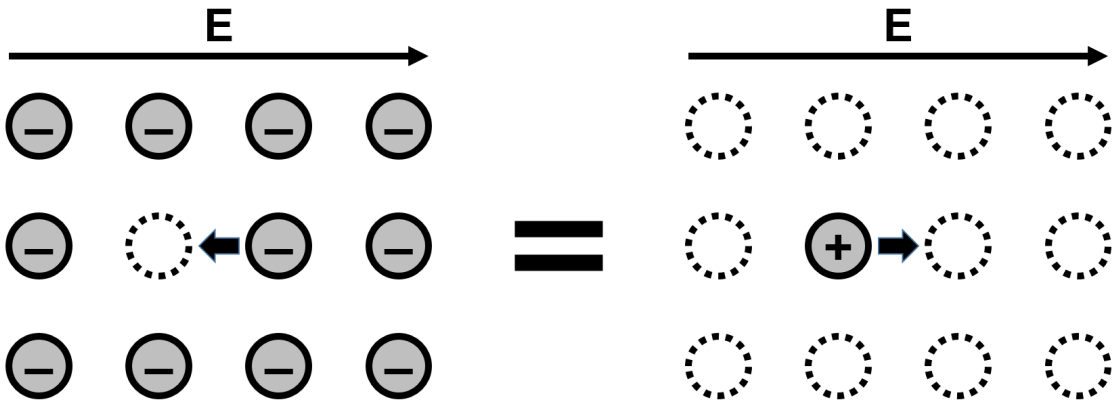

Figure 2.5: Left panel: a negative ion hops against the field into a neighbouring lone vacancy. Right panel: equivalently, a lone positive vacancy hops with the field to a neighbouring available vacancy site. Thinking of the vacancies as quasiparticles is a more convenient method of modelling vacancy-mediate motion. This approach is well-known in semiconductor physics, where motion of electrons in the almost-full valence band via vacancies is more easily treated as the motion of positively-charged hole quasiparticles.

calculated to be only 0.14 eV per defect, corresponding to an exceptionally large vacancy concentration of 0.4% at room temperature [52]. For comparison, the lowest Schottky defect formation energy per defect in the inorganic perovskite $BaTiO_3$ is 2.29 eV. Furthermore, density functional theory (DFT) studies on $MAPbI_3$ have found the activation energy E_A for an iodide to hop to a neighbouring vacant site to be in the relatively low range 0.1-0.6 eV [51, 53, 54]. An illustration of halide motion in a perovskite is shown in Figure 2.4. An activation energy in this range yields behaviour on the timescale of seconds, matching the timescale of hysteresis. Combined with the large vacancy density, this leads to an ionic conductivity that is sufficiently large to affect the internal electric fields within the active layer.

Calculation for the cations in $MAPbI_3$ yield an E_A of 0.84 eV for MA^+ hopping and 2.31 eV for Pb^{2+} [51]. Compared to the E_A of 0.58 eV for I^- from the same reference, this means MA^+ motion is about 20,000 times slower and Pb^{2+} about 10^{29} times slower than iodide – these ions (certainly the lead) are stationary on the timescale of a typical *J-V* curve. Furthermore, electrochemical experiments have shown that it is the iodide *vacancies* that are the mobile species in in $MAPbI_3$ [55].

All PV technologies require efficient separation of the photo-generated electrons and holes. This is accomplished by the built-in field, which sweeps electrons and holes towards their respective transport layers. Being charged particles, ions are also affected by the electric field. As the motion of halide ions via vacancies, it is convenient to consider the motion of the vacancies throughout the film as shown in Figure 2.5. The positively charged halide ion vacancies are swept towards the hole transport layer (HTL), resulting in a net positive space charge next to the HTL. Similarly, the concentration of halide vacancies next to the electron transport layer (ETL) is depleted, resulting in a net negative space charge of equal and opposite charge to the layer by the HTL. This charge accumulation creates a field that acts to screen the field within the bulk of the perovskite layer, and thereby hinder charge

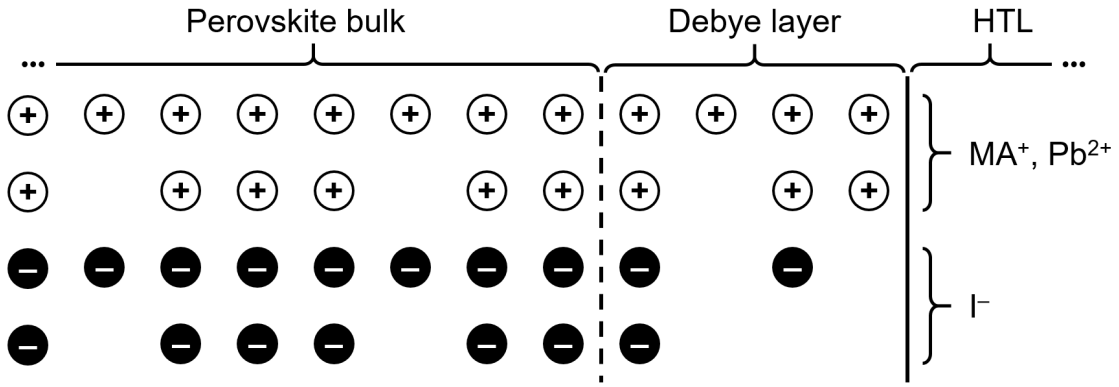

Figure 2.6: Illustration of the ionic Debye layer next to the hole transporting layer (HTL) in $MAPbI_3$. The bulk of the perovskite has no net charge, as cation and anion vacancies cancel. The built-in field causes a build up of anion vacancies (a depletion of anions) next to the HTL, causing a next positive charge to screen the field. Another Debye layer of equal and opposite net charge is formed by anion build up (anion vacancy depletion) next to the ETL.

separation and extraction from this material. From analogies to this effect in electrolytes, the regions of build-up of charge at the edges of the perovskite are termed Debye layers. An illustration of the Debye layer next to the hole transporter is given in Figure 2.6. The weaker the internal electric field, the less efficient the charge separation and the lower the current. Thus, a change in the electric field within the perovskite due to ion motion will change the cell current.

As the applied voltage is varied, the magnitude of the electric potential drop across the perovskite varies. The electric field within the perovskite layer is the driving force for ion motion, so the ions charge/discharge the Debye layers until this bulk field has been fully screened. The larger the potential drop, the more charged the layers need to be. Changes to the applied voltage thus modify the equilibrium ion densities within the Debye layers which charge (or discharge) accordingly towards the new equilibrium.

From the differential form of Ohm's law, valid for the linear response regime, the ionic current density into the layers is proportional to the unscreened electric field within the film. Given sufficient time, the vacancy density throughout the perovskite will reach the steady-state profile for that voltage. However, since halide motion is a relatively slow process this re-equilibriation of the Debye layer charge can take many seconds at room temperature. Over the timescale of a normal J-V scan, carried out over the course of 10-20 seconds, the vacancies are unable to reach their steady-state profile for each measurement point. In effect, the vacancy density profile lags behind the scan. For a reverse scan the Debye layers are less charged than at equilibrium, while for forward scan are more charged than at equilibrium. The measured current for a given voltage then depends on the scan direction, with the reverse scan better than the forward scan.

Of course, a solar module under normal operation is not subjected to a sweeping voltage. A charge controller, usually incorporated within the inverter, is used to apply an appropriate load to the module such that it operates at maximum power point (MPP) where the product of current and voltage is at its highest. It is tempting, then, to dismiss hysteresis as simply making measurement more difficult. However,

ion motion, the process behind hysteresis, also has an effect on performance in the field. When held at MPP, the PCEs of most perovskite devices will tend towards a value better than obtained on the poor forward scan but worse than obtained on the good reverse scan. Understanding ion motion is crucial in order to mitigate – or exploit – its effects.

The movement of vacancies throughout perovskites also has a possible consequence for long-term stability. As perovskite active layers are very soft, the strain on the lattice from extensive ion motion may act as a source of degradation [56, 57, 58]. This strain occurs in the regions of significant build-up and depletion of ion density at the edges of the perovskite. Ion build-up/depletion has also been found to lead to carrier build-up [2, 59, 60], which in turn contributes to additional Ohmic heating and thermal breakdown [61]. This may be especially troublesome if the temperature within the perovskite passes through a phase transition, for example the tetragonal-cubic transition in MAPI around 327 K [62]. Another key degradation pathway in perovskites has been linked to the highly reactive O_2^- superoxide species that is generated from the reaction of free electrons in the perovskite with molecular oxygen. *Ab initio* simulations indicate that iodide vacancies are the preferred site for O_2^- formation [63].

2.3 Motivation

The rapid rise in PSC performance has meant that the field's theoretical understanding of perovskites is still relatively basic. For other photovoltaic technologies, such as silicon, the more modest rise in performance has been accompanied by a theoretical framework explaining why and how each advancement is helpful. Indeed, the extensive body of theory is used to help inform new advancements. By contrast, perovskite research is so fast paced that to remain competitive groups have used trial and error to find the best working perovskite materials, transport layers and device structures. A strong theoretical backing is needed to trust that a perovskite-based device will survive and behave as expected over the 20-30 year lifetime of a PV module, in addition to helping predict new combinations of materials and architectures that will perform well.

As a result, a robust macroscale model that accurately describes the relevant physics of a PSC has so far eluded the field. This is partly due to it not being obvious *a priori* what aspects of the system actually are relevant. With hindsight, perhaps the most significant examples of this are the presence of electronic Debye layers. Upon completing the model, we find the the ionic Debye layers within the perovskite induce counter layers of electronic charge within the transport layers. These layers actually dominate the profile of the electric potential throughout the device, but are only found if the carriers within the transport layers are explicitly modelled and the dynamics of the carriers and ions are solved together.

However, stable numerical solution of even a simplified model is extremely difficult. A full discussion of the problems encountered is provided in the next section. The key difficulties, summarised, are:

1. the huge disparity in timescales of motion between the ions, diffusivity of order 10^{-17} m^2/s, and the carriers, diffusivity of order 10^{-4} m^2/s;

Issue	Richardson et al. [59]	Van Reenen et al. [64]	Calado et al. [60]	Jacobs et al. [65]	**This work**
Explicit transport layers			✓	✓	✓
Accurate ionic timescale	✓		✓	✓	✓
Sufficient grid resolution	✓			✓	✓
Accurate internal interfaces				✓	✓
Band offsets				✓	✓
Coupled particle dynamics			✓		✓

Table 2.1: Features of existing drift-diffusion models.

2. the packing of vacancies and carriers near the interfaces in the narrow Debye layers, width of order nanometres, compared to the width of the device, width of order a micrometre;

3. discontinuities in vacancy and carrier densities at and across the internal interfaces between the perovskite and transport layers; and

4. important processes (e.g. surface recombination) occurring directly at and only at interface regions.

Each of the above points contributes to severe numerical instability. Consequently, every published drift-diffusion paper thus far has neglected one or more of these points. Artifically speeding up the ions reduces the difference in timescales between carrier and ion motion. Discretising the equations of study on too coarse a grid improves simulation time considerably and avoids tight packing of particles near the interfaces. Smearing out interface effects, like surface recombination, over the nearby region and ignoring band offsets between materials avoids numerical difficulties at the interfaces. Modelling the ions and carriers separately, i.e. decoupling these dynamics, completely avoids the timescale disparity. The issue with any of these solutions is that they model the system incorrectly. A selection of prominent drift-diffusion models, and the features of each, is given in Table 2.1.

This ultimate aim of this project has been to construct the first model that can properly simulate a perovskite solar cell, without neglecting any important features. Only then can the effects of ion motion, including hysteresis, be truly understood. In the next chapter, the approach taken to build the model is outlined. Afterwards, the model is used to comprehensively study the consequences of ion motion.

Chapter 3

Drift-diffusion model

In this chapter, we first set out the problem we wish to solve. Then, we derive the equations describing the physics of the system. Next, we devise a novel mathematical scheme to model the system computationally. Finally, we demonstrate how to apply this scheme to obtain a functional and useful model.

3.1 Statement of problem

The key component of any solar cell is the active layer, in this case a lead halide perovskite. The job of the perovskite is to absorb light, generating electrons and holes which are then separated by drift and diffusion to opposite sides of the layer. A schematic showing this and the following is given in Figure 3.1. The perovskite is placed between two charge-selective transport layers (TLs), that allow one species of carrier to be extracted but block the other species. The transport layers are each connected to metallic electrodes, from which the cell can be attached to external circuitry. The difference in Fermi levels between the electrodes causes the built-in field to develop across the cell. Here we consider planar devices, where each layer is a flat slice of material. In most devices light enters the device from the ETL side, although inverted architectures where light enters from the HTL side are also used. Within the perovskite layer mobile halide vacancies can drift and diffuse around, influenced by and interacting with the electric potential throughout the layer.

We would like to be able to calculate the current that will be measured over time from a PSC under some regime of applied voltage and illumination. We also want to know the electric potential and distributions of particle densities within the cell over this time. We are especially interested in the effect of ion motion, as much of the interesting behaviour of PSCs appears to be due to the changing halide vacancy density interacting with the internal electric fields. The choice of transport layers has been found experimentally to affect observed behaviours, so it is desirable to explicitly model both TLs as well. The model needs to be able to accurately describe the device behaviour throughout a J-V curve, where the applied voltage sweeps from forward bias down to short-circuit and back up.

It is necessary, then, to model electrons, holes and halide vacancies, all coupled with the electric potential, across an entire device from electrode to electrode. Rather than modelling particles individually, which would be impractical on the micron scale, we solve for the densities of the particle species as continua. By restricting ourselves to looking at planar devices, we can exploit slab symmetry to

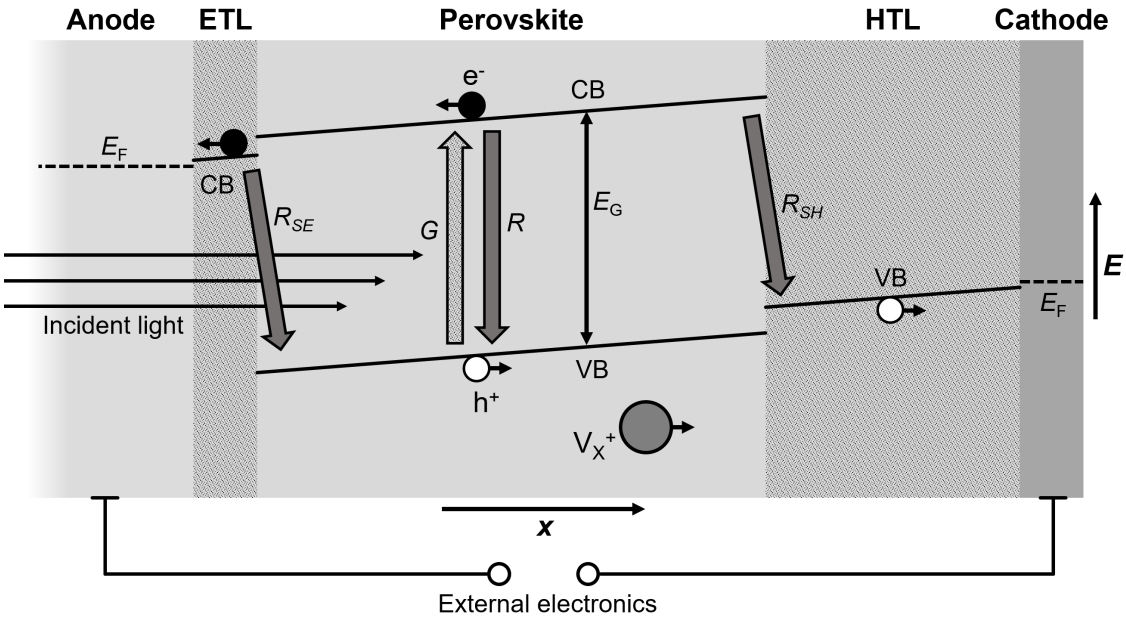

Figure 3.1: Schematic of a typical planar perovskite solar cell, with processes of interest. The perovskite layer is sandwiched between the carrier-selective electron and hole transport layers (ETL, HTL), which are each connected to an electrode. Conduction and valence bands (CB, VB) are denoted by solid lines, Fermi levels (E_F) of the electrodes by dashed lines. Light enters through the anode side, passes through the ETL and is absorbed in the perovskite. The electrons (black circles, e^-) and holes (white circles, h^+) are generated (upward arrow, G) and can recombine (downward arrow, R) in this layer. Carriers drift and diffuse into their respective tranport layers and are collected by the electrodes. Carriers in the transport layers may recombine with carriers in the perovskite, known as surface recombination (downward arrows, R_{SE} and R_{SH}). Halide vacancies (grey circle, $\mathrm{V_X^+}$) also drift and diffuse within the perovskite layer, affecting the electric potential within the cell. Note the given designation of anode and cathode is true for a device under normal PV operating conditions. In far forward bias, when the applied voltage exceeds the open-circuit voltage, the formal designations are swapped.

only need to model one spatial dimension.

The exciton binding energies of perovskites are low [20, 21] ($< k_\mathrm{B}T$) due to the relatively high permittivity of these materials screening the Coulomb attraction between the bound carriers. This means that generated electron-hole pairs readily separate into free electrons and holes. As a result, we can simply model direct generation of free electrons and holes without considering a separate exciton species as would be required in an organic device. Within the ETL, only electrons need to be modelled due to the large VB offset between ETL and perovskite. Likewise, only holes need be modelled in the HTL due to the large CB offset with the perovskite. Halide vacancies are restricted to the perovskite layer, as the TLs do not have halide sublattices.

In summary, we need to model vacancies in the perovskite layer, electrons in the perovskite and ETL, holes in the perovskite and HTL and the electric potential over all three layers – five particle densities and three electric potentials, for a total of

eight quantities.

3.2 Drift and diffusion

For a species of particle in an ideal mixture in one dimension, diffusion will act to spread the particles out as described by Fick's first law,

$$\mathcal{F}_{\text{Diff}} = -D\frac{\partial}{\partial x}c, \tag{3.1}$$

where $\mathcal{F}_{\text{Diff}}$ is the diffusion flux, D the diffusivity, c the number density and x the spatial dimension. Generally speaking the driving force for diffusion is a gradient in chemical potential, which for an ideal mixture is the concentration. If the particles also have a charge q, a drift flux will occur given by

$$\mathcal{F}_{\text{Drift}} = -cq\mu\frac{\partial}{\partial x}\phi, \tag{3.2}$$

where μ is the mobility and ϕ the electric potential. The total particle flux $\mathcal{F}$ can be found by adding the equations together. Using the Einstein relation

$$D = \mu k_{\text{B}}T \tag{3.3}$$

where T is absolute temperature, this yields

$$\mathcal{F} = \mathcal{F}_{\text{Diff}} + \mathcal{F}_{\text{Drift}} = -D\left(\frac{qc}{k_{\text{B}}T}\frac{\partial}{\partial x}\phi - \frac{\partial}{\partial x}c\right). \tag{3.4}$$

We can then substitute the expression into the continuity equation

$$\frac{\partial c}{\partial t} = -\frac{\partial}{\partial x}\mathcal{F} + G - R \tag{3.5}$$

which states that the rate at which the particle density builds up at some point over time t is is equal to the rate at which particles flow into that point plus any sources G and less any sinks R. This yields the drift-diffusion equation

$$\frac{\partial c}{\partial t} = D\frac{\partial}{\partial x}\left(\frac{qc}{k_{\text{B}}T}\frac{\partial}{\partial x}\phi - \frac{\partial}{\partial x}c\right) + G - R. \tag{3.6}$$

Each species of particle, described by $c(x,t)$, will obey its own version of (3.6), with its own values for D and q and forms for G and R. This is the equation we will use for our five particle densities.

The electric potential ϕ at a point is described by the Poisson equation

$$\frac{\partial^2}{\partial x^2}\phi = -\frac{\rho}{\varepsilon}, \tag{3.7}$$

where ρ is the net charge density and ε the permittivity of the material. It is (3.7) that couples the dynamics of the particles to each other, as ρ is the sum of all charge densities

$$\rho = \sum_s q_s c_s \tag{3.8}$$

where s denotes a species with charge q_s and number density c_s. This is the equation we will use for our three electric potentials.

Symbol	Definition
Dimensions	
x	Space
t	Time
Dependent variables	
$\phi,\ \phi_E,\ \phi_H$	Electrostatic potential in the perovskite, ETL, HTL
$n,\ n_E$	Electron density in the perovskite, ETL
$p,\ p_H$	Hole density in the perovskite, HTL
P	Halide vacancy density in the perovskite
Fluxes	
$\mathcal{F}_n,\ \mathcal{F}_{nE}$	Electron flux in the perovskite, ETL
$\mathcal{F}_p,\ \mathcal{F}_{pH}$	Hole flux in the perovskite, HTL
$\mathcal{F}_P$	Halide vacancy flux in the perovskite
Generation and recombination	
G	Generation in the perovskite
R	Bulk recombination in the perovskite
R_{SE}	Surface recombination at the perovskite/ETL interface
R_{SH}	Surface recombination at the perovskite/HTL interface

Table 3.1: Variables in the drift-diffusion equations and boundary conditions.

3.3 System of equations

Now that we know what to model and how to model them, we can write down a set of equations describing how the particle densities and electric potentials evolve over time. Then, we can write the boundary conditions (BCs) that couple them together and complete the problem. For clarity and reference, variables are defined in Table 3.1 and constants and parameters in Table 3.2. We define the widths of the perovskite, electron transport and holes transport layers as b, b_E and b_H respectively. The positions of the layer interfaces are thus defined as anode/ETL at $x = -b_E$, ETL/perovskite at 0, perovskite/HTL at b and HTL/cathode at $b + b_H$. Particle fluxes in the positive x direction, i.e. rightward, are defined as positive.

3.3.1 Dependent variables

Perovskite layer ($0 < x < b$)

Within the perovskite layer, we need to model the moving ion vacancies, electrons and holes, all coupled together with the electric potential.

$$\frac{\partial^2}{\partial x^2}\phi = -\frac{q}{\varepsilon}\left(P - N_0 + p - n\right) \tag{3.9}$$

$$\frac{\partial}{\partial t}P = -\frac{\partial}{\partial x}\mathcal{F}_P \qquad \text{where} \quad \mathcal{F}_P = -D_P\left(\frac{\partial}{\partial x}P - \frac{P}{k_\mathrm{B}T}\frac{\partial}{\partial x}\phi\right) \tag{3.10}$$

$$\frac{\partial}{\partial t}n = -\frac{\partial}{\partial x}\mathcal{F}_n + G - R \quad \text{where} \quad \mathcal{F}_n = -D_n\left(\frac{\partial}{\partial x}n + \frac{n}{k_\mathrm{B}T}\frac{\partial}{\partial x}\phi\right) \tag{3.11}$$

$$\frac{\partial}{\partial t}p = -\frac{\partial}{\partial x}\mathcal{F}_p + G - R \quad \text{where} \quad \mathcal{F}_p = -D_p\left(\frac{\partial}{\partial x}p - \frac{p}{k_\mathrm{B}T}\frac{\partial}{\partial x}\phi\right) \tag{3.12}$$

Parameter	Symbol	Value	
Fundamental constants			
Boltzmann constant	k_B	8.617×10^{-5} eV/K	
Elementary charge	q	1.602×10^{-19} C	
Vacuum permittivity	ε_0	8.854×10^{-12} F/m	
Experimental conditions			
Temperature	T	300 K	
Thermal voltage ($k_\mathrm{B}T/q$)	V_T	25.9 mV	
Properties of the perovskite layer			
Width	b	400 nm	
Permittivity	ε	24.1 ε_0	[66]
Electron diffusivity	D_n	1.7×10^{-4} m^2 s^{-1}	[67]
Hole diffusivity	D_p	1.7×10^{-4} m^2 s^{-1}	[67]
Conduction band energy	E_C	-3.7 eV	[68]
Valence band energy	E_V	-5.4 eV	[68]
Bandgap ($E_C - E_V$)	E_G	1.7 eV	
Conduction band density of states	g_c	8.1×10^{24} m^{-3}	[66]
Valence band density of states	g_v	5.8×10^{24} m^{-3}	[66]
Halide vacancy equilibrium density	N_0	1.6×10^{25} m^{-3}	[52]
Halide vacancy diffusivity	D_P	1.8×10^{-17} m^2 s^{-1}	[51]
Properties of the electron transporting layer (ETL)			
Width	b_E	50 nm	
Permittivity	ε_E	40 ε_0	
Electron diffusivity	D_{nE}	1.5×10^{-5} m^2 s^{-1}	
Doping density	d_E	1.7×10^{24} m^{-3}	
Conduction band/LUMO energy	E_{FE}	-3.95 eV	[68]
Properties of the hole transporting layer (HTL)			
Width	b_H	200 nm	
Permittivity	ε_H	3 ε_0	
Hole diffusivity	D_{pH}	1.5×10^{-5} m^2 s^{-1}	
Doping density	d_H	8×10^{23} m^{-3}	
Valence band/HOMO energy	E_{FH}	-5.0 eV	[68]
Generation parameters			
Incident photon flux (with energy $> E_\mathrm{G}$)	F_{ph}	1.4×10^{21} m^{-2} s^{-1}	
Perovskite absorptivity	α	1.3×10^{7} m^{-1}	[69]
Bulk recombination parameters			
Bimolecular recomb. coefficient	β	4×10^{-11} m^3 s^{-1}	
SRH electron pseudolifetime	τ_n	5×10^{-12} s	
SRH hole pseudolifetime	τ_p	5×10^{-10} s	
Surface recombination parameters			
Electron rec. velocity at perov/ETL interface	v_{nE}	1×10^{5} m s^{-1}	
Hole rec. velocity at perov/ETL interface	v_{pE}	1 m s^{-1}	
Electron rec. velocity at perov/HTL interface	v_{nH}	0.01 m s^{-1}	
Hole rec. velocity at perov/HTL interface	v_{pH}	1×10^{5} m s^{-1}	

Table 3.2: Constants and parameters in the drift-diffusion equations and boundary conditions. The usual values used for each in the following simulations is given; unless otherwise stated, these values are used.

The constant N_0 term represents static negatively charged cation vacancies, as all defects are assumed to come in charge neutral groups (e.g. V_{MA}^{-} and V_{X}^{+}, or V_{Pb}^{2-} and $2V_{X}^{+}$). Vacancies are assumed to neither generate nor recombine, and so G and R are 0 in (3.10). The generation term G is the same for electrons and holes as they are generated in pairs and varies with x due to the attenuation of light throughout the layer. G may in principle be a function of t if the illumination is varied with time, such as from the light being turned on and off. The recombination rate R is also the same for both electrons and holes as these particles recombine in pairs. How R depends on the concentration of the carriers itself depends on the recombination mechanism(s). In principle, R may depend on other parameters. It has been suggested [70] that vacancies may act as recombination centres so that R is also a function of P, although we do not consider this here.

Generation occurs according to the Beer-Lambert law

$$G(x) = F_{ph}\alpha \exp\left(-\alpha x\right), \tag{3.13}$$

where α is the perovskite absorptivity and F_{ph} is the flux of incident photons on the perovskite layer. Only photons with an energy greater than the bandgap E_{G} need be considered, as those with an energy less than the bandgap cannot be absorbed.

Recombination within the bulk of the perovskite is modelled using both the Shockley-Read-Hall (SRH) and bimolecular (band to band) schemes, such that

$$R(n,p) = R_{\mathrm{SRH}}(n,p) + R_{\mathrm{B}}(n,p) \tag{3.14}$$

where $R_{\mathrm{SRH}}(n,p)$ is the SRH contribution and $R_{\mathrm{B}}(n,p)$ the bimolecular contribution. SRH recombination is a trap-based mechanism, whereby one carrier relaxes into a trap state within the bandgap (trap energy between E_V and E_C) until an opposite carrier later relaxes into the same trap. Here we consider traps in the middle of the bandgap, i.e. with energy $\frac{1}{2}(E_C + E_V)$. The extent to which SRH recombination occurs depends critically on the trap density, and therefore on material quality. Bimolecular recombination is direct relaxation of an electron into a hole across the bandgap. This is the opposite process to generation, and is unavoidable. The measured ideality factors of PSCs indicate that SRH is the dominant recombination mechanism in the bulk. This is often the case in photovoltaics, as one relaxation process is generally slower than multiple relaxations of the same total energy change.

The equation for the rate of Shockley-Read-Hall recombination is

$$R_{\mathrm{SRH}}(n,p) = \frac{np - n_i^2}{\tau_p(n + n_i) + \tau_n(p + n_i)} \tag{3.15}$$

where τ_n and τ_p are the representative times for the electrons and holes to be captured by the traps, termed pseudolifetimes. Longer lifetimes yield less recombination. The term n_i is the intrinsic carrier density, given by

$$n_i = g_c g_v \exp\left(-\frac{E_G}{2k_{\mathrm{B}}T}\right) \tag{3.16}$$

where g_c and g_v are the conduction and valence band densities of states and E_{G} the bandgap. The bimolecular recombination rate is (comparatively) simply

$$R_{\mathrm{B}}(n,p) = B\left(np - n_i^2\right), \tag{3.17}$$

where B is the bimolecular recombination rate constant and n_i again the intrinsic carrier density.

Surface recombination at each internal interface also occurs according to an SRH mechanism. At the perovskite/ETL interface, the rate of recombination between electrons in the ETL (density n_E) with holes in the perovskite (density p) is

$$R_{\mathrm{SE}}(n_E, p) = \frac{n_E p - n_i^2}{(n_E + n_i)/v_{nE} + (p + n_i)/v_{pE}} \tag{3.18}$$

where v_{nE} and v_{pE} are electron and hole surface recombination velocities at the ETL/perovskite interface. Similarly for the perovskite/HTL interface, the recombination rate between holes in the HTL (density p_H) with electrons in the perovskite (density n) is

$$R_{\mathrm{SH}}(p_H, n) = \frac{n p_H - n_i^2}{(n + n_i)/v_{nH} + (p_H + n_i)/v_{pH}}. \tag{3.19}$$

where v_{nH} and v_{pH} are electron and hole surface recombination velocities at the perovskite/HTL interface. The surface recombination velocities are constants describing the rate at which carriers move toward the interface. Lower velocities yield less surface recombination.

Electron transport layer ($-b_E < x < 0$)

Within the ETL, we need to model electrons and the electric potential.

$$\frac{\partial^2}{\partial x^2}\phi_E = -\frac{q}{\varepsilon_E}\left(d_E - n_E\right) \tag{3.20}$$

$$\frac{\partial}{\partial t}n_E = -\frac{\partial}{\partial x}\mathcal{F}_{nE} \quad \text{where} \quad \mathcal{F}_{nE} = -D_{nE}\left(\frac{\partial}{\partial x}n_E + \frac{n_E}{k_{\mathrm{B}}T}\frac{\partial}{\partial x}\phi_E\right) \tag{3.21}$$

There is no generation term as the ETL does not absorb, and no bulk recombination as holes are not permitted into this layer.

Hole transport layer ($b < x < b + b_H$)

Within the HTL, we need the holes and electric potential.

$$\frac{\partial^2}{\partial x^2}\phi_H = -\frac{q}{\varepsilon_H}\left(p_H - d_H\right) \tag{3.22}$$

$$\frac{\partial}{\partial t}p_H = -\frac{\partial}{\partial x}\mathcal{F}_{pH} \quad \text{where} \quad \mathcal{F}_{pH} = -D_{pH}\left(\frac{\partial}{\partial x}p_H - \frac{p_H}{k_{\mathrm{B}}T}\frac{\partial}{\partial x}\phi_H\right) \tag{3.23}$$

Like the ETL, there is no generation or bulk recombination.

3.3.2 Boundary conditions

To fully close the problem, we require two boundary conditions (BCs) for each dependent variable. This is because each variable needs a BC at its leftmost limit and another at its rightmost limit. As we have four variables within the perovskite and two in each transport layer, we require two BCs at each electrode and six at each internal boundary.

Electrode/ETL interface ($x = -b_E$)

The difference in potentials between electrodes is defined as $V_{\text{bi}} - V_{\text{ap}}$, where V_{bi} is the built-in voltage and V_{ap} the applied voltage. Provided this is satisfied, we have freedom to choose where the potential is zero. Here we choose to make the BCs symmetrical, so

$$\phi_E = \frac{(V_{\text{bi}} - V_{\text{ap}})}{2}. \tag{3.24}$$

A similar equation appears for the potential at the right electrode (3.38), hence the denominator 2. The electron density by the left electrode is fixed to d_E, the doping density of the ETL.

$$n_E = d_E \tag{3.25}$$

ETL/perovskite interface $x = 0$

Both potential and displacement field must be continuous over an interface.

$$\phi_E = \phi \tag{3.26}$$

$$\varepsilon \frac{\mathrm{d}\phi}{\mathrm{d}x} = \varepsilon_E \frac{\mathrm{d}\phi_E}{\mathrm{d}x} \tag{3.27}$$

Halide ions may not leave the perovskite, so the flux next to the boundary must be zero.

$$\mathcal{F}_P = 0 \tag{3.28}$$

Electron flux (and therefore charge) must be conserved, taking account of surface recombination. Any electron flux toward the boundary from the ETL side may either transfer to electron flux within the perovskite or become surface recombination flux.

$$\mathcal{F}_{nE} = \mathcal{F}_n + R_{SE} \tag{3.29}$$

The electron densities across the energy barrier can be calculated from the Boltzmann distribution. The ratio of probabilities that an electron will be on the (lower-energy) ETL side of the interface compared to the (higher-energy) perovskite side, or Boltzmann factor, is $\exp\left(\frac{E_C - E_{FE}}{k_{\text{B}}T}\right)$. Taking account of the densities of states in each layer, we find the boundary condition

$$n_E = n \frac{d_E}{g_c} \exp\left(\frac{E_C - E_{FE}}{k_{\text{B}}T}\right). \tag{3.30}$$

This equations ensures that the Fermi levels immediately on each side of the interface are equal. Finally, holes may not freely enter the electron transport layer but may recombine with electrons in the ETL, so any flux towards the interface must be recombination flux.

$$-\mathcal{F}_p = R_{SE} \tag{3.31}$$

Perovskite/HTL interface ($x = b$)

The BCs at the perovskite/HTL interface follow the same logic as for the ETL/perovskite interface. Both potential and displacement field must be continuous over the interface.

$$\phi = \phi_H \tag{3.32}$$

$$\varepsilon \frac{\mathrm{d}\phi}{\mathrm{d}x} = \varepsilon_H \frac{\mathrm{d}\phi_H}{\mathrm{d}x} \tag{3.33}$$

Halide ions may not leave the perovskite.

$$\mathcal{F}_P = 0 \tag{3.34}$$

To conserve holes, any hole flux toward the interface must either transfer to hole flux within the HTL or become surface recombination flux.

$$\mathcal{F}_p = \mathcal{F}_{pH} - R_{SH} \tag{3.35}$$

Hole densities across the energy barrier are related by the Boltzmann factor to ensure continuity of Fermi level.

$$p_H = p \frac{d_H}{g_v} \exp\left(\frac{E_{FH} - E_V}{k_\mathrm{B} T}\right) \tag{3.36}$$

Electrons may not freely enter the hole transport layer but may recombine with holes in the HTL, so any flux towards the interface must be recombination flux.

$$\mathcal{F}_n = R_{SH} \tag{3.37}$$

HTL/Electrode interface ($x = b + b_H$)

The potential here must be

$$\phi_H = -\frac{(V_\mathrm{bi} - V_\mathrm{ap})}{2} \tag{3.38}$$

to ensure the total voltage across the cell is $V_\mathrm{bi} - V_\mathrm{ap}$ when combined with (3.24). The hole density by the right electrode is fixed to d_H, the doping density of the HTL.

$$p_H = d_H \tag{3.39}$$

As yet, we have introduced no new concepts – only standard physics and equations have been used up to this point. However, as discussed at the end of the previous chapter, the nature of the problem means a number of mathematical phenomena conspire to make solution very difficult. An out-of-the-box solution is not able to cope with the stiffness and discontinuities. The remainder of this chapter details how these problems were overcome to build a working simulation framework.

3.4 Method of Lines

Collecting all these equations together, we have a set of PDEs. The drift-diffusion equations have both a temporal and a spatial dimension as independent variables, and the Poisson equation has just a spatial dimension. To model these coupled equations computationally, we employ the *method of lines*. In this case we discretise in space using a centred finite difference (FD) scheme, leaving a set of coupled ODEs in time only. For a function y, the gradient at the point a is approximated by

$$\frac{\mathrm{d}}{\mathrm{d}x}y(a) \approx \frac{y(a+h) - y(a-h)}{2h} \tag{3.40}$$

where h is the (small) finite difference. This equation will be required to discretise the drift-diffusion equations. Derivation of (3.40) from drawing a right-angled triangle is trivial. Alternatively, derivation can also be accomplished only slightly less easily from rearranging and summing two Taylor series to show that there is $O(h^2)$ error.

We obtain the second derivative of y at a by noting that by (3.40) implies

$$\frac{\mathrm{d}^2}{\mathrm{d}x^2}y(a) \approx \frac{\frac{\mathrm{d}}{\mathrm{d}x}y(a+\frac{1}{2}h) - \frac{\mathrm{d}}{\mathrm{d}x}y(a-\frac{1}{2}h)}{h}, \tag{3.41}$$

and then substituting (3.40) into (3.41) twice with the appropriate choice of h yields

$$\frac{\mathrm{d}^2}{\mathrm{d}x^2}y(a) \approx \frac{y(a-h) - 2y(a) + y(a+h)}{h}, \tag{3.42}$$

which also has $O(h^2)$ error.

A limitation of the equations (3.40) and (3.42) as written is the use of a single finite difference h on each side of a. When we discretise equations on a grid, we select a *mesh* of points on which to solve the equations. The values of h are then determined by the spacing between mesh points. Therefore, the equations written above constrain us to using a uniform mesh, with all solution points evenly spaced by h.

For a wide range of applications, a uniform mesh is acceptable. The choice of mesh spacing h is determined by how quickly the function being approximated varies. The more severe the variation in y, the smaller h must become to properly approximate $\frac{\mathrm{d}}{\mathrm{d}x}y$. As h is reduced, more mesh points are required to model the same span of y, increasing computational expense.

Uniform meshes become inappropriate when y varies significantly more quickly in some regions of x than others. To accurately model the solution in the quickly varying region, h must be made very small over the entire solution region, even where such resolution is unnecessary. As discussed later, the ion vacancy density in a PSC is flat for the majority of the perovskite layer (the bulk) but varies quickly over just a few nanometres next to the interfaces with the transport layers. Worse, due to the band bending caused by the ionic Debye layers and the charge-selective nature of the transport layers, the carrier densities vary by many orders of magnitude within the space of these same few nanometres. Counter layers of electronic charge build-up within the transport layers next to the interface with the perovskite, causing yet more variation in density. To model the difficult regions near material interfaces accurately, mesh points need to be packed extremely tightly. With a uniform mesh,

the points must be packed uniformly tightly even within the bulk regions of the layers that account for the majority of the device yet where the solution varies slowly. In fact, the total number of mesh points required for integration becomes so large that a desktop computer does not have enough memory to store the solution.

A better choice for this problem is a non-linear mesh, with points packed much more tightly at the interfaces that within the bulk. This means we must reformulate the finite difference equations to account for different spacings on each side. Denoting the mesh spacing on the negative and positive side of the point a as h_- and h_+ respectively, then adding the Taylor series for $y(a+h_+)$ and $y(a-h_-)$ and rearranging, (3.40) becomes

$$\frac{\mathrm{d}}{\mathrm{d}x}y(a) \approx \frac{y(a+h_+) - y(a-h_-)}{h_+ + h_-}. \tag{3.43}$$

In the same fashion as before, by noting

$$\frac{\mathrm{d}^2}{\mathrm{d}x^2}y(a) \approx \frac{\frac{\mathrm{d}}{\mathrm{d}x}y(a+\frac{1}{2}h_+) - \frac{\mathrm{d}}{\mathrm{d}x}y(a-\frac{1}{2}h_-)}{\frac{1}{2}(h_+ + h_-)}, \tag{3.44}$$

it follows by substituting (3.40) into (3.44) twice with the appropriate choices of h that

$$\frac{\mathrm{d}^2}{\mathrm{d}x^2}y(a) \approx \frac{2}{h_-(h_- + h_+)}y(a-h_-) - \frac{2}{h_-h_+}y(a) + \frac{2}{h_+(h_- + h_+)}y(a+h_+). \tag{3.45}$$

Armed with equations (3.43) and (3.45), we can construct versions of the Poisson and drift-diffusion equations discretised in space. For the Poisson equation at mesh point i with spatial position x_i, this yields

$$0 = \frac{2}{h_i(h_i + h_{i+1})}\phi_{i-1} - \frac{2}{h_ih_{i+1}}\phi_i + \frac{2}{h_{i+1}(h_i + h_{i+1})}\phi_{i+1} + \frac{\rho_i}{\varepsilon_i} \tag{3.46}$$

where ϕ_i is the potential at point i and $h_i = x_i - x_{i-1}$. We can use (3.46) for our three sets of Poisson equations in Section 3.3.

Before jumping straight into applying the same approach on (3.4) to obtain a discretised expression for particle flux at point i, we should remember that the reason we are calculating flux is to put this straight back into a discretised version of (3.5) for the particle density. As flux describes flow from one point to another, it is really more sensible to calculate fluxes at half points. We can then apply expressions for fluxes at the half points into the continuity equation.

There is, in fact, a difficult consequence from *not* doing this. If we had calculated fluxes at the integer points and substituted this into the continuity equation, the solution for particle densities would consist of unphysical quick oscillations between grid points as in Figure 3.2. This type of numerical artefact is known as odd-even decoupling or checkerboarding. Consider the equation $\mathrm{d}u/\mathrm{d}x = 0$, which has the obvious solution of u is constant. With finite differences on a discrete uniform grid of spacing h, the derivative at the ith point $\mathrm{d}u/\mathrm{d}x|_i$ is approximated to $(u_{i+1} - u_{i-1})/2h$. The values for the derivative on odd-numbered nodes depend only the values of the solution on even-numbered nodes, and vice versa. As a result, to satisfy the system of equations, we only need the odd nodes to have the same value and separately for the even nodes to have the same value. The odd and even values

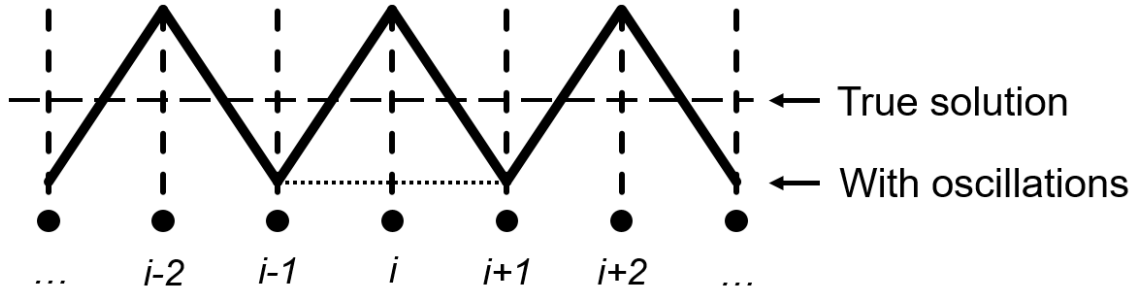

Figure 3.2: Illustration of the cause of odd-even decoupling when solving for the equation $\mathrm{d}u/\mathrm{d}x = 0$ on a discrete grid. The true solution is given by the flat dashed line. When solving on a mesh an oscillation (solid line) also satisfies the equation, as the gradients as calculated by finite differences are still flat (gradient for point i given by the dotted line). The values for the solution for odd nodes and for even nodes can diverge.

need not be the same, however. The zig-zag pattern in Figure 3.2 is exhibited in this case. For true solutions that are not flat the calculated solutions may still zig-zag, but veer up and down to track the true solution. This may happen for some or all of the densities for the PSC system for some periods of time during the solve. This effect is well known in computational fluid dynamics, where it can manifest in the calculation of pressure. As velocity is proportional to the spatial derivative of pressure, in this context it may be referred to as pressure-velocity decoupling.

Calculating the spatial derivatives at half points avoids this issue. Note we have already applied this approach to the formulation of the discretised Poisson equation (3.46) from using the points $a + h_+$ and $a - h_-$ to calculate first derivatives in the discretised second derivative operator in (3.44). Defining point $i+\frac{1}{2}$ as being halfway between points i and $i+1$, with spatial position $x_{i+\frac{1}{2}} = \frac{1}{2}(x_i + x_{i+1})$, we obtain an expression for the particle flux at point $i + \frac{1}{2}$ as

$$\mathcal{F}_{i+\frac{1}{2}} \approx -D\left[\frac{q}{k_\mathrm{B}T}\frac{c_i + c_{i+1}}{2}\frac{\phi_{i+1} - \phi_i}{h_{i+1}} - \frac{c_{i+1} - c_i}{h_{i+1}}\right] \tag{3.47}$$

where we have interpolated the particle densities at the integer points i and $i+1$ to obtain the density at the halfway point $c_{i+\frac{1}{2}} = \frac{1}{2}(c_i + c_{i+1})$. This then substitutes into (3.5) to give

$$\frac{\mathrm{d}}{\mathrm{d}t}c_i \approx -\frac{\mathcal{F}_{i+\frac{1}{2}} - \mathcal{F}_{i-\frac{1}{2}}}{\frac{1}{2}(h_i + h_{i+1})} + G_i - R_i \tag{3.48}$$

or in full

$$\begin{aligned}\frac{\mathrm{d}}{\mathrm{d}t}c_i \approx \frac{D}{h_i + h_{i+1}}\Bigg(&\frac{(c_{i+1} + c_i)(\phi_{i+1} - \phi_i) - 2(c_{i+1} - c_i)}{h_{i+1}} \\ &- \frac{(c_i + c_{i-1})(\phi_i - \phi_{i-1}) - 2(c_i - c_{i-1})}{h_i}\Bigg) + G_i - R_i\end{aligned} \tag{3.49}$$

where G_i and R_i are the generation and recombination at point i. We will use this for our five sets of equations of particle densities from Section 3.3.

Now that we have discretised away the spatial derivatives, we are left with a set of coupled ODEs in time for particle densities and a set of algebraic equations for

potential. In general, a system of N coupled first-order ODEs is written as

$$\begin{aligned} \frac{\mathrm{d}}{\mathrm{d}t}u_1 &= f_1(u_1) \\ \frac{\mathrm{d}}{\mathrm{d}t}u_2 &= f_2(u_2) \\ &\vdots \\ \frac{\mathrm{d}}{\mathrm{d}t}u_N &= f_N(u_N) \end{aligned} \tag{3.50}$$

where the u's describe the state of the system and the f's describe how the u's change with time. We can write this more succinctly as

$$\frac{\mathrm{d}}{\mathrm{d}t}\mathbf{u} = \mathbf{f}(\mathbf{u}) \tag{3.51}$$

where the vector $\mathbf{u}(t)$ is a vector describing the state of the system at time t and $\mathbf{f}$ is a function describing how the system changes with time. Being able to express the system in this form is extremely convenient, as a great many solvers exist for integrating such a system over time. Examples include the `integrate.ode` function in the open-source `scipy` library [71] for the Python programming language, and the entire suite of MATLAB ODE solvers [72].

Unfortunately, we don't quite have this as the Poisson equations (3.46) contain no time derivative. This is why (3.46) is written in the form $0 = ...$, with the (lack of) time derivative on the left hand side. Instead, we have a system of differential and algebraic equations – a *differential-algebraic system of equations*, or DAE system. This system may be expressed as

$$\mathbf{M} \cdot \frac{\mathrm{d}}{\mathrm{d}t}\mathbf{u} = \mathbf{f}(\mathbf{u}) \tag{3.52}$$

where $\mathbf{M}$ is a matrix known as the *mass matrix*. For a semiexplicit problem, such as this one, $\mathbf{M}$ is diagonal. Put simply, element $M_{i,i}$ is 1 if the equation has a time derivative and zero if not. If all equations have a time derivative then $\mathbf{M}$ is the identity matrix and we recover (3.51). For our system, $M_{i,i}$ will be 1 if equation i corresponds to a drift-diffusion equation (3.49) or 0 if i corresponds to a Poisson equation (3.46).

3.5 Solver

A DAE system with the form of (3.52) is less convenient than a coupled ODE system with form (3.51) as most ODE solvers cannot handle a DAE system out of the box. The MATLAB solver `ode15s` can [73], so we use it for this problem. This solver is an implicit, variable-step, variable-order (VSVO) algorithm.

An explicit solver integrates over time by calculating the new state of the system from an equation of the form

$$\mathbf{u}(t + \Delta t) = \mathbf{F}_{\text{explicit}}(\mathbf{u}(t)), \tag{3.53}$$

where $\mathbf{u}(t)$ is the state of the system at time t and Δt is the timestep. By contrast, an implicit method integrates by solving an equation involving the state of the system

at the current time and the state of the system being solved for, i.e.

$$0 = \mathbf{F}_{\text{implicit}}(\mathbf{u}(t), \mathbf{u}(t + \Delta t)). \tag{3.54}$$

For non-trivial problems it is often mathematically impossible to find an analytic solution for $\mathbf{u}(t + \Delta t)$, requiring an expensive numerical solution for each timestep. While explicit solvers are then clearly faster than implicit methods at calculating a single step due to their relative simplicity, implicit methods are generally more accurate and more stable for most systems (including this one). This means the explicit method generally needs to take significantly smaller timesteps to obtain the same accuracy as an implicit solver. For complex problems, especially stiff problems like ours, implicit solvers perform better by performing more work per timestep, but taking far fewer steps overall. `ode15s` is an implicit solver at it solves a system of linear equations for each timestep.

Variable-step means that the solver can adapt the timestep (Δt in (3.54)) used as integration progresses. A variable-step solver normally implements this by performing a trial step and checking if the calculated $\mathbf{u}(t+\Delta t)$ is within an acceptable error tolerance. If the step is too big, the trial step is attempted again with a smaller Δt. This again increases the amount of work done by the solver per step, as the solver needs to calculate the appropriate step size. However, much like the rationale for using a variable mesh spacing, the solver can take extremely fine timesteps when $\mathbf{u}$ varies rapidly to preserve accuracy and larger steps when $\mathbf{u}$ varies slowly for speed.

Order in this context refers to the order of the error in the numerical differentiation formulae used. The `ode15s` solver uses formulae with error of order between $\mathrm{O}(h)$ and $\mathrm{O}(h^5)$ and is specifically designed to work for stiff problems, hence the `15s` in the name. The advantage of calculating the same timestep multiple times using formulae with different order is that the difference in the solutions from each formula can be used to estimate the truncation error for that timestep, as we expect formulae with higher orders to be successively more accurate. This feeds back into the choice of step size: if the estimated error is unacceptably large the timestep is reduced, while if the error is safely below tolerance the timestep may be lengthened.

Discussion of exactly what `ode15s` does is beyond the scope of this thesis. Indeed, a major advantage of using a well-established solver, alongside the efficiency that comes from the code being written and optimised for years by experts in numerics, is that it is unnecessary understand the minutae of the solver's operation. However, knowledge of broadly what the solver is doing is critical to using it efficiently.

Consider again the DAE system $\mathbf{M} \cdot \frac{\mathrm{d}}{\mathrm{d}t}\mathbf{u} = \mathbf{f}(\mathbf{u})$, where we define n as the length of $\mathbf{u}$ ($\mathbf{f}$ is therefore also length n and $\mathbf{M}$ is $n \times n$). The Jacobian $\mathbf{J}$ for this system is defined as the derivative of $\mathbf{f}$ with respect to $\mathbf{u}$,

$$\mathbf{J} = \frac{\partial \mathbf{f}}{\partial \mathbf{u}} = \begin{pmatrix} \dfrac{\partial \mathbf{f}}{\partial u_1} & \dfrac{\partial \mathbf{f}}{\partial u_2} & \cdots & \dfrac{\partial \mathbf{f}}{\partial u_n} \end{pmatrix} = \begin{pmatrix} \dfrac{\partial f_1}{\partial u_1} & \dfrac{\partial f_1}{\partial u_2} & \cdots & \dfrac{\partial f_1}{\partial u_n} \\ \dfrac{\partial f_2}{\partial u_1} & \dfrac{\partial f_2}{\partial u_2} & \cdots & \dfrac{\partial f_2}{\partial u_n} \\ \vdots & \vdots & \ddots & \vdots \\ \dfrac{\partial f_n}{\partial u_1} & \dfrac{\partial f_n}{\partial u_2} & \cdots & \dfrac{\partial f_n}{\partial u_n} \end{pmatrix} \tag{3.55}$$

or equivalently elementwise as

$$J_{i,j} = \frac{\partial f_i}{\partial u_j}. \tag{3.56}$$

As seen easily from the latter definition of $\mathbf{J}$ in (3.56), the Jacobian describes how sensitively the time derivative for the ith variable depends on a change in the jth variable.

For example, from the definition of the discretised drift-diffusion equation (3.49), the rate of change of the concentration of a particle species at point i, $\frac{\mathrm{d}}{\mathrm{d}t}c_i$, depends on the concentration of that species and the electric potential at the points $i-1$, i and $i+1$ and possibly the concentration of other species at i via the generation and recombination terms. Only varying these terms directly has an effect on the element of $\mathbf{f}$ corresponding to $\frac{\mathrm{d}}{\mathrm{d}t}c_i$. Therefore, the row of the Jacobian corresponding to $\frac{\mathrm{d}}{\mathrm{d}t}c_i$ will have non-zero elements only for columns corresponding to the aforementioned concentrations and potentials. The values of other variables do not directly feed in to the calculation of $\frac{\mathrm{d}}{\mathrm{d}t}c_i$, and so $\mathbf{J}$ has zeros as entries for other columns.

It is clear that the Jacobian for our system is extremely sparse. Continuing with the drift-diffusion equation example, only 8 or so elements in a row of $\mathbf{J}$ will be non-zero, depending on the form of R. For a u with length of around 2000, as we will use later, then we expect only about 0.4% of $\mathbf{J}$ elements to be non-zero. In addition, because the time derivative of each element of u depends only on values of u corresponding to nearby spatial positions (i.e. immediately left and right), the non-zero elements of $\mathbf{J}$ will be clustered in an *a priori* predictable pattern. We say the Jacobian will have a banded structure, as non-zero terms form diagonal bands.

As an implicit solver, `ode15s` iteratively solves linear systems of the form

$$(\mathbf{M} - h\gamma\mathbf{J})\boldsymbol{\Delta} = \mathbf{r} \tag{3.57}$$

for $\boldsymbol{\Delta}$ where other values are known [74]. The residual $\mathbf{r}$ is initially calculated from $\mathbf{f}(\mathbf{u}(t))$, then the calculated correction $\boldsymbol{\Delta}$ is added to $\mathbf{r}$. $\mathbf{M}(t)$ and $\mathbf{J}(t)$ are the mass matrix and Jacobian, h is the timestep and γ is a constant scalar parameter used to speed up convergence. Solution of this system iterates until $\mathbf{r}$ is a sufficiently accurate approximation to $\mathbf{u}(t+h)$. For our system, $\mathbf{M}$ is constant throughout the simulation. $\mathbf{J}(t)$ is calculated at the start and reused as often as possible to improve speed. If `ode15s` detects that it will not be able to calculate $\mathbf{u}(t+h)$ within 4 iterations of (3.57), $\mathbf{J}$ is recalculated [72]. If $\mathbf{J}$ is already up to date, h is reduced. If h becomes too small, the solver fails.

The performance and stability of the solver depend heavily on efficient (and possible) repeated solution of (3.57). `ode15s` obtains $\mathbf{J}$ by calling `numjac`, another MATLAB function. `numjac` calculates an approximation to $\mathbf{J}(t)$ using numerical differentiation. At its heart, this scheme basically calculates the change in $\mathbf{f}(\mathbf{u})$ for small changes in each element of $\mathbf{u}$. As mentioned above, calculation of $\mathbf{J}$ occurs many times during the solve. For a typical $\mathbf{u}$ of length 2000, the Jacobian has 4 million elements. Most of these elements are zero, although `numjac` has no way of knowing this in advance. One way of helping the solver is by providing the sparsity pattern of $\mathbf{J}$. The sparsity pattern $\mathbf{S}$ is defined as

$$S_{i,j} = \begin{cases} 0 & \text{if } J_{i,j} = 0 \\ 1 & \text{otherwise.} \end{cases} \tag{3.58}$$

While **J** is a function of time, **S** is constant. Knowledge of **S** means `numjac` only needs to calculate the elements of **J** that are non-zero. We can calculate **S** by inspection beforehand with a simple routine that calculates $\mathbf{f}(\mathbf{u})$ for some **u** and checking if there is a difference when each element of **u** is changed by a small amount. This can be done for a toy system with very few grid points (e.g. a couple of dozen across the entire device) and extrapolated up for a general number of grid points as points within the bulk of each layer follow a predictable pattern. Providing **S** was found to speed up the overall integration by several orders of magnitude for simulation of a typical *J*-*V* curve.

3.6 Stiffness, ill-conditioning and grid choice

If we now continue straight to implementing the model for real parameter values on a uniform grid, we will find that `ode15s` is unable to find a solution. The timestep will shrink extremely rapidly as the solver attempts to maintain stability, and will eventually crash. The phenomenon being exhibited here is *stiffness*. While there is no consensus on the exact definition of stiffness [75], the relevance here is that stiffness is a phenomenon exhibited by a system of equations whereby numerical integration methods need to take extremely small timesteps in order to remain stable.

What is causing this, and how can we stop it? An intimately linked concept that is crucial to understanding stiffness is *ill-conditioning*, specifically of the iteration matrix $\mathbf{M} - h\gamma\mathbf{J}$. The Euclidean norm of some matrix **A** is

$$\|\mathbf{A}\| = \max_{|\mathbf{x}|=\mathbf{1}} |\mathbf{A}.\mathbf{x}| \tag{3.59}$$

where as usual

$$|\mathbf{x}| = \sqrt{\mathbf{x}^{\mathrm{T}}.\mathbf{x}}. \tag{3.60}$$

The norm describes the maximum stretching that **A** applies to a vector, and is the matrix equivalent to vector length. From the norm, we can then define the condition number of the matrix **A** as

$$K(\mathbf{A}) = \|\mathbf{A}\|.\|\mathbf{A}^{-1}\|. \tag{3.61}$$

Furthermore, it can be shown [76] that the condition number is the ratio of smallest to largest singular value for the matrix. The condition number represents then the greatest possible distortion **A** can apply to a unit sphere; for example, if $K(\mathbf{A}) = 10^3$ then **A** stretches one thousand times more in one direction than another. Specifically, K represents the ratio of the largest scaling to the smallest scaling applied to a vector by the matrix. K, then, is a measure of how close a matrix is to being singular. A unit matrix or scalar multiple thereof stretches all directions equally, and so $K = 1$. A singular matrix collapses one or more directions completely, so $K = \infty$.

K has an important implication for the error in solving linear systems. For a rigorous treatment see Forsythe and Moler [76], but the general idea is that any uncertainty or error in elements of **y** may be multiplied by K when solving $\mathbf{A}.\mathbf{x} = \mathbf{y}$ for **x**. The larger the condition number, the larger the numerical errors when computing the inverse. If $K(\mathbf{A}) = 10^k$ then you expect to lose up to k digits of precision due to

numerical error. A matrix with a large K is known as ill-conditioned. This differs from an ill-posed problem, where the matrix is genuinely singular and $K = \infty$.

One can intuit from this reasoning and from the definition of the mass matrix $\mathbf{M}$ and Jacobian $\mathbf{J}$ why solving a linear system with the matrix $\mathbf{M} - h\gamma\mathbf{J}$ is difficult. Our physical system contains particles moving on extremely disparate timescales, with the carrier diffusivities typically 10^{12} times greater than the vacancy density, introducing temporal stiffness to the system. Elements of $\mathbf{J}$ corresponding to rates of change in carrier densities will therefore typically be much larger than those for rates of change in ion density, and so $K(\mathbf{J})$ is extremely large. In addition, quantities in the Debye layers typically vary more rapidly than in the bulk, adding spatial stiffness to the problem. Reducing h will decrease the contribution of $\mathbf{J}$ and make the matrix tend towards $\mathbf{M}$, but $\mathbf{M}$ is analytically singular itself so this does not help.

Once a simulation is run, $K(\mathbf{M} - h\gamma\mathbf{J})$ is quickly found to be greater than 10^{16} for any value of h that satisfies even a lax error tolerance. Double precision floating point stores about 16 decimal digits of precision, and we are losing more than 16 due to numerical error from the matrix alone! This is further compounded by rounding and truncation errors. `ode15s` recognises that, because K is singular to working precision, the system cannot be solved and gives up.

Another way of thinking about this problem is in terms of the size of timestep required to model a small change in carrier and vacancy densities over a small timestep. In order to model a change in a carrier density properly, the solver must take a small timestep. However, over that same tiny timestep the change in ion density is much smaller. If the change in ion density is of the order of the machine precision, rounding error will quickly blow out of control.

Mathematical Methods for Physicists by Arfken and Weber [77] offers two suggestions to solve an ill-conditioned system: 'try a different mathematical attack', and 'arrange to carry more significant figures and push through by brute force'. We utilise both of these suggestions.

Reformulating the system is perhaps the more elegant answer. Stiffness is a property of the system of equations, not the physical system itself, so a thoughtful reformulation of the equations can allow us to model the exact same physics but more easily. As alluded to in Section 3.4, the solution here is a variable mesh spacing. The spatial stiffness may be eased by packing grid points more tightly where solution components are likely to change rapidly, and placing fewer points in the bulk of the layers where the components vary more smoothly.

The general idea here is demonstrated in Figure 3.3. Non-zero elements of the Jacobian depend strongly on how quickly the solution varies in space, due to the spatial derivatives. However, because the spatial derivatives have been discretised away, what is really important is the difference in solution between neighbouring points. From finite differences, the difference in the ith solution component u_i between neighbouring points at around some position a is simply

$$\Delta u_i|_a \approx h \left.\frac{\partial u_i}{\partial x}\right|_a \tag{3.62}$$

where h is the x spacing between the points and $\partial u_i/\partial x$ is the 'true' derivative of u_i. For a uniform mesh, Δu is large in regions where $\partial u_i/\partial x$ is large and small in regions where $\partial u_i/\partial x$ is small. If $\partial u_i/\partial x$ varies significantly over the solution region, then this contributes to a large disparity between elements in the Jacobian which will have a large condition number.

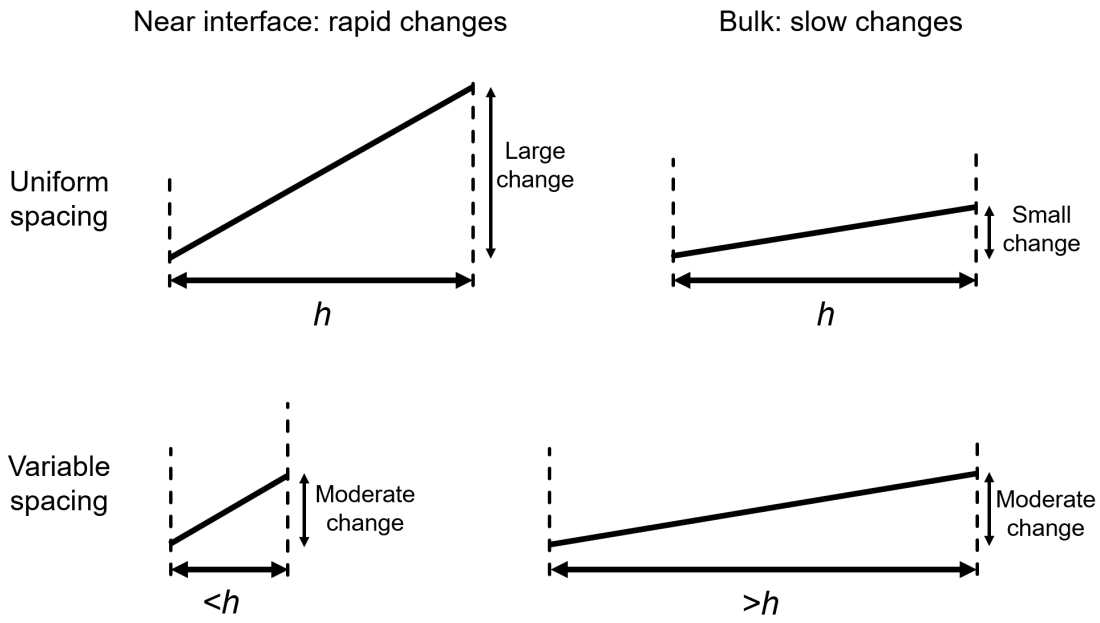

Figure 3.3: Representation of the advantage of variable mesh spacing (h) over uniform for this problem. As the solution varies far more rapidly in space near the interfaces than in the bulk, for a uniform grid the difference in solution components between neighbouring grid points is much greater near the interfaces. Differences between neighbouring points can be made more regular across the device by placing points more closely together where the solution changes rapidly.

While we cannot change the actual spatial derivative $\partial u_i/\partial x$ of any solution component without modelling a different physical system, we can choose the distance between neighbouring points. In fact, if we could choose h to be roughly inversely proportional to the true derivative, we could get a roughly constant Δu_i values throughout the solution region. This reduces the Jacobian condition number of the system, aiding integration. Note however that we need to take all solution components (all i) into account to make a difference. For our physical system, we know from previous work [59] that large spatial derivatives for all solution components only ever occur near the interfaces and not in the bulk, so we know to place more points near the interfaces and fewer in the middle of layers.

Choosing a sensible fixed distribution of grid points like this requires some *a priori* knowledge of which regions in space are troublesome. In principle it is possible to have an adaptive grid, when points are moved on the fly to obtain the best conditioned Jacobian. As we do know beforehand where large derivatives occur, an adaptive mesh is not worth the extra computational effort. Of course, in principle the solution components may be stiff in different locations in space, complicating the adaptive approach.

In a uniform spacing scheme of n points between 0 and 1, the position of point i can be expressed as

$$x_i = \frac{i-1}{n-1} \quad \text{for } i = [1, n]. \tag{3.63}$$

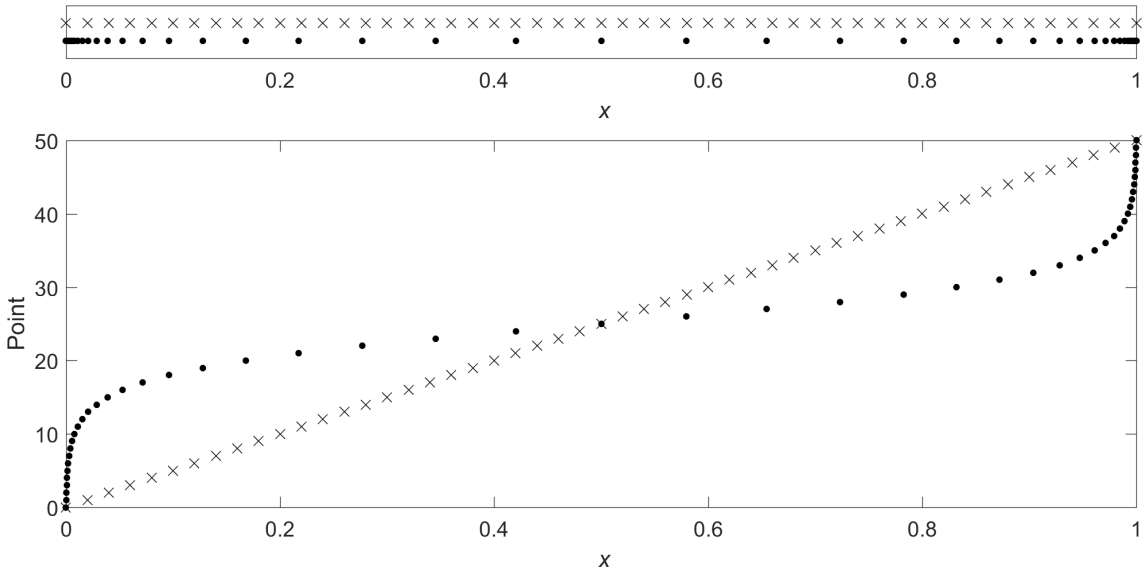

Figure 3.4: a) Illustration of a uniform grid spacing (crosses) and a variable mesh (dots) using the tanh spacing scheme in x, each for N=51 points between 0 and 1. b) As for (a), but with the points spaced evenly along the vertical axis to demonstrate the underlying linear and tanh behaviours of the spacings.

For this problem we choose a spacing given by

$$x_i = \frac{\tanh(8\frac{i-1}{n-1} - 4)}{2\tanh(4)} + \frac{1}{2} \quad \text{for } i = [1, n]. \tag{3.64}$$

This spacing uses utilises the properties of the hyperbolic tangent function to pack points more tightly near 0 and 1. This is an arbitrary choice, however, and other functions could easily be used. Both the uniform and tanh grid spacing schemes are illustrated in Figure 3.4. From our choice of (3.64), we also define the half-points of the staggered grid on which first spatial derivatives are solved as

$$x_{i+\frac{1}{2}} = \frac{x_i + x_{i+1}}{2} \quad \text{for } i = [1, n-1]. \tag{3.65}$$

A naïve approach might be to use a coarse uniform spacing in the bulk and a finer uniform spacing near the interfaces. In this way there are indeed more points near the interface as required. There are two issues with this approach. Firstly, how rapidly the solution varies increases monotonically as you approach the boundaries. Therefore, a grid which with a monotonically decreasing spacing as you approach the boundaries is best suited to modelling this problem. Secondly, the transition point between fine and coarse mesh will have a very small spacing on the fine side and a large spacing on the coarse side. This sudden change in spacing in the finite differences may contribute to numerical instability and cause artefacts in the solution. In the tanh approach, the grid spacing changes gradually such that the spacings between any point and each of its two neighbours are approximately the same.

The variable mesh will not fix stiffness from the disparity between ion and carrier timescales. However, Arfken and Moler's other suggestion, just using more digits, does tackle this. Upon investigation, it was found that the condition number with

the variable mesh was in the range $10^{16} < K < 10^{34}$ – too poorly conditioned for 16 digit double precision to handle, but managable using 34 digit quadruple precision. The Advanpix Multiprecision Computing Toolbox [78] for MATLAB was used to obtain a quadruple precision enabled version of `ode15s`. This version works in the same manner as the built-in MATLAB function, but with support for higher precision in general and special optimisation for quadruple precision.

3.7 Implementation

We need to choose specifically how to write the problem in a form `ode15s` can accept. This solver integrates a problem of the form given in (3.52) where the user provides the function $\mathbf{f}(\mathbf{u}(t))$, mass matrix $\mathbf{M}$, a range of t over which to integrate and the initial conditions $\mathbf{u}(0)$. Various other arguments may also be optionally passed in – the truly important one is the Jacobian sparsity, as discussed earlier.

The first thing to do is to decide on a convention for the state vector $\mathbf{u}$. Given that our problem consists of eight groups of equations, it is natural to define our mathematical system in blocks. We can choose a definition of $\mathbf{u}$ that groups like equations together. By defining $\mathbf{P}$ as the (column) vector of values of vacancy density in the perovskite, ϕ as the vector of electric potentials in the perovskite and so on we can then define

$$\mathbf{u} = \begin{pmatrix} \mathbf{P} \\ \phi \\ \mathbf{n} \\ \mathbf{p} \\ \phi_{\mathbf{E}} \\ \mathbf{n_E} \\ \phi_{\mathbf{H}} \\ \mathbf{p_H} \end{pmatrix}. \tag{3.66}$$

To populate $\mathbf{u}$, we need to decide whether to solve for each quantity on the main grid (x_0, x_1, ...) or the half grid ($x_{\frac{1}{2}}$, $x_{1+\frac{1}{2}}$, ...). The general principle to avoiding odd-even decoupling is to define a staggered grid as discussed in Section 3.4, and that if a quantity is calculated and/or stored on one grid then its first derivative should be on the other grid. We have choice, however, as to whether to calculate each of the above eight sets of dependent variables on the main grid (where i is an integer) or the half-grid (i is an integer plus $^1/_2$). While this may not at first glance seem like a useful decision, and it is tempting to just define everything on the main grid for 'simplicity', this choice influences how easy it is to implement the boundary conditions (3.24)-(3.39). The best way to choose a grid is to consider how the boundary conditions will be implemented, which requires us to think about is how to formulate $\mathbf{f}$.

The elements of $\mathbf{f}$ corresponding to bulk equations are simply implementations of the Poisson equation (3.46) and drift-diffusion equation (3.49). For drift-diffusion equations we put a 1 in $\mathbf{M}$, and for Poisson equations we put a 0. Elements at the boundaries need a little more thought, but the principle is the same. There are 16 boundary conditions in total, 2 for each of the 8 types of variable. Of these 16, 8 are Dirichlet, where the value is set, and the remaining 8 are Neumann, where the spatial derivative is set.

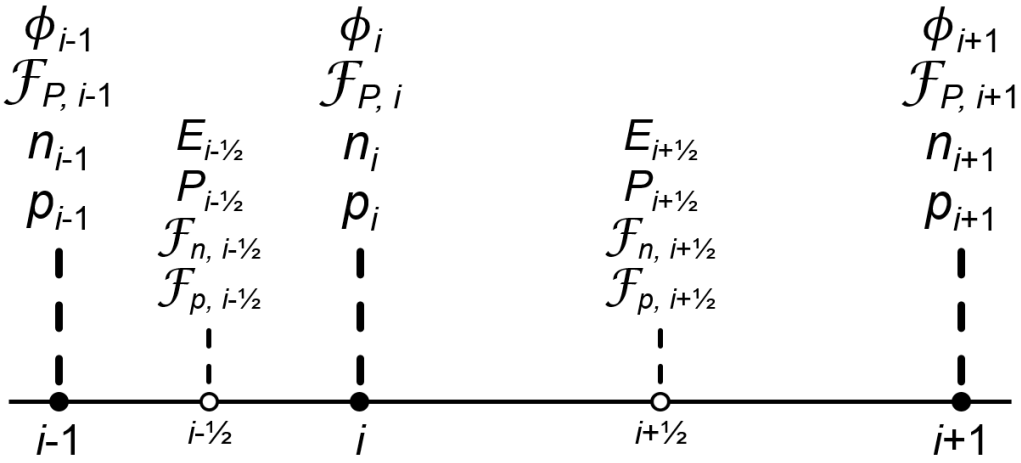

Figure 3.5: Points for the main grid (integer indixes, solid points) and half grid (integer plus a half indices, hollow points) in the perovskite layer. The spacing for the main grid varies according to a tanh function (3.64); half grid points are halfway between the two neighbouring main grid points. On the main grid, we solve for the electric potential ϕ, vacancy flux $\mathcal{F}_P$, electron density n and hole density p. On the half grid, we solve for electric field E, vacancy density P, electron flux $\mathcal{F}_n$ and hole flux $\mathcal{F}_p$. By calculating derivatives on a staggered grid, odd-even decoupling is avoided.

The 4 Dirichlet conditions at the TL/electrode boundaries are easiest, as they do not even have to be solved: wherever one of these 'variables' appears in an equation, we can simply write the constant or function that it is equal to. For the condition $n_E(x = -b_E) = d_E$, for example, wherever $n_E(x = -b_E)$ appears in an equation we can replace it with d_E. For each of the 4 Dirichlet conditions at the internal boundaries, we have two variables that are equal or proportional to the other. We therefore need to solve for only one of these variables from each of these equations, and can use these equations to substitute away the other. For (3.30) for example, we choose to solve for $n(x = 0)$ and replace references to $n_E(x = 0)$ with $n(x = 0)\frac{d_E}{g_c}\exp\left(\frac{E_C - E_{FE}}{k_B T}\right)$.

The Neumann conditions cannot be satisfied in this way, and must be included explicitly. Fortunately, as `ode15s` solves system of DAEs, these can be included in the equations in the exact same way as the Poisson equations. As none of the boundary conditions have time derivatives, we simply rewrite each equation in the form $0 = ...$ and place a 0 in the corresponding entry of the leading diagonal of $\mathbf{M}$. The solver will ensure that these equations are satisfied when integrating.

Now we have an idea of how the boundary conditions are implemented, we can choose which grid to solve each variable on. All boundaries coincide with points on the main grid, so variables with conditions depending on the value of the variable should be also solved on the main grid. Variables with Neumann boundary conditions will be easiest to solve on the half grid, so that their derivatives are on the main grid. In this way we avoid needing to interpolate as much as possible. The electric potential has 4 Dirichlet conditions, one at each boundary, and 2 Neumann conditions, one at each internal boundary. Therefore, it makes sense to define ϕ, ϕ_E and ϕ_H on the main grid, allowing easiest implementation of the Dirichlet conditions as discussed above. The vacancy density, on the other hand, only has

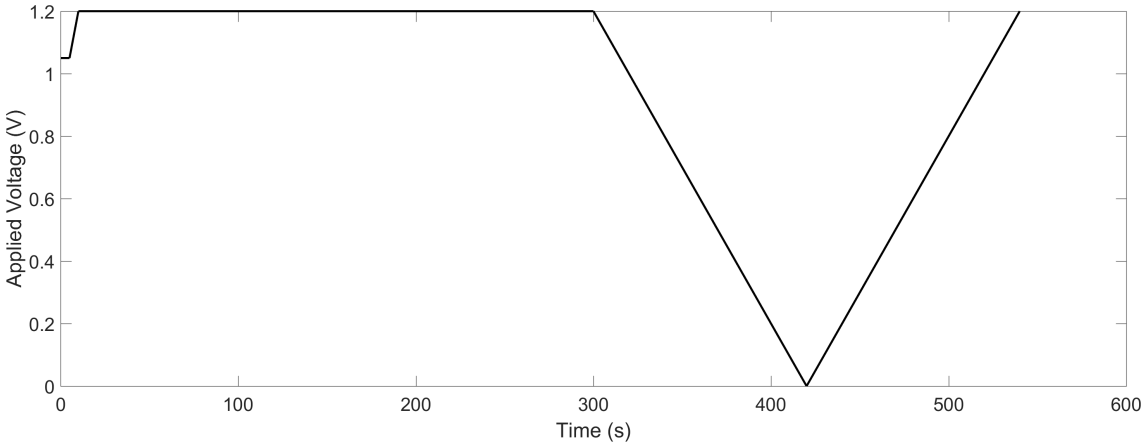

Figure 3.6: Voltage regime for a J-V curve from 1.2 V with scan rate 10 mV/s. $V_{\text{ap}}(t = 0) = V_{\text{bi}} = 1.05$ V to satisfy the ICs.

Neumann boundary conditions, namely zero flux at the internal interfaces. Thus, it makes sense to define P on the half grid, such that the flux of P is on the main grid. The choice for the electron and hole densities is less clear cut, as each has 2 Dirichlet and 2 Neumann conditions. However, the 2 Neumann conditions on the carrier fluxes each depend on surface recombination, which in turn depends on the carrier densities at the interfaces. Therefore, solving for n, p, n_E and p_H on the main grid is the best choice. The variables solved for on each grid are summarised in Figure 3.5.

We also require an initial condition (IC) $\mathbf{u}(0)$. Choice of $\mathbf{u}(0)$ is actually not that important, as we can simply run the solve for a few simulated minutes under constant illumination and voltage to let $\mathbf{u}$ naturally relax to a physical state. What is important is choosing the initial conditions to be roughly consistent with the equations. If the IC is not exactly consistent, `ode15s` will adjust some of the values to make it constent for us. We will just choose something easy to implement, let the solver fix any inconsistencies for us and integrate for a short time to get a useful IC. If we always start simulations at $V_{\text{ap}} = V_{\text{bi}}$, then the boundary conditions on the electric potential at each electrode $\phi_E(x = -b_E)$ and $\phi_H(x = b + b_H)$ are both zero. We can then simply have $\phi_E = \phi = \phi_H = 0$ over the whole device. For each particle density, we just choose uniform densities in each layer.

Measurements are made on the simulated device by varying the simulated V_{ap} which feeds into the boundary conditions on the electric potential (3.24) and (3.38). The $V_{\text{ap}}(t)$ for a typical J-V curve, with scan rate 10 mV/s is shown in Figure 3.6. $V_{\text{ap}} = V_{\text{bi}}$ for the first 5 s to allow the solver to settle. Then, the voltage is changed to 1.2 V (a standard starting voltage) over the period of another 5 s, and allowed to equilibrate at 1.2 V for 290 s. The voltage is then swept down to 0 V ($=J_{\text{SC}}$) and back up. The total current through the device at any time is calculated from the sum of the electron, hole and displacement currents using the equation

$$\begin{aligned} J &= J_n + J_p + J_d \\ &= -q\mathcal{F}_n + q\mathcal{F}_p + \frac{\partial D}{\partial t} \\ &= D_n\left(\frac{\partial n}{\partial x} + \frac{n}{k_{\text{B}}T}\frac{\partial \phi}{\partial x}\right) - D_p\left(\frac{\partial p}{\partial x} - \frac{p}{k_{\text{B}}T}\frac{\partial \phi}{\partial x}\right) - \varepsilon\frac{\partial}{\partial t}\frac{\partial \phi}{\partial x} \end{aligned} \tag{3.67}$$

where D is the displacement field and other symbols have their usual meanings. This equation is true at any point in the perovskite due to conservation of charge, but is easiest to calculate in the middle of the perovskite due to the slow variation of all variables in the bulk.

The solver is actually called three times for a J-V sweep as depicted in Figure 3.6 – once for the equilibration region, once for the down scan and once for the up scan. This is because once the particle densities have settled during the equilibration period, the solver can take very large timesteps without compromising accuracy due to the vary small time derivatives. For fast scan rates, the solver may actually step over the entire J-V sweep and report nothing. By stopping the solver at the end of the equilibration time and feeding the final state as the initial conditions of another solve, the J-V sweep cannot be missed. Performing the same procedure when the scan changes direction ensures a time point is taken at exactly V_{ap}=0, avoiding any numerical issues where the solver may cut across the sharp reversal in V_{ap} and not simulate short-circuit correctly.

3.8 Summary

In this chapter, we have constructed a custom drift-diffusion model of all three particle species across the perovskite and both transport layers. Rather than modelling particles individually, we solve for the densities of the particle species as continua. Using this method we are able to model the entire device, from electrode to electrode, throughout a typical J-V curve within a few minutes on a desktop computer. For slower scan rates, the simulation is faster than real time.

Development of this model to the current state comprised a large portion of the project. While drift-diffusion as a method is not new, there is no other drift-diffusion model in published literature capable of modelling a perovskite device correctly. Other methods either neglect the transport layers, neglect difficult boundary conditions or use unrealistic parameters to obtain convergence, losing the physicality of the underlying system in the process.

Chapter 4

How ion motion controls current, loss and performance

In this chapter, the basis of ion motion theory is laid out. First, we look at the distributions of the electric potential and particle densities throughout the device at steady-state. Then we explore the ubiquitous measurement of electrical and electronic devices, the current-voltage characteristic or J-V curve. Through a quantitative approach, we construct a robust theory as to explain why J-V hysteresis occurs and when to expect it, then use the J-V curve as a tool to analyse the effect of ion motion on the performance of typical PSCs. We first quantify how performance loss and hysteresis varies with scan rate with temperature. From the Arrhenius variation with temperature of these key behaviours, we extract the activation energy for ion motion – a remarkably direct demonstration that ion motion is responsible for anomalous behaviours in PSCs. Next, we evaluate a number of potential strategies to reduce loss from ion motion using the methods developed in these earlier sections. Finally, we discuss how preconditioning affects measurements and situations where ion motion may improve device performance.

4.1 Steady-state

The basis of the ion motion theory of perovskite solar cells (PSCs) is the interaction of ions with the built-in field within the perovskite layer. To demonstrate the effect of moving ions, Figure 4.1 shows the same perovskite solar cell held at short-circuit (applied voltage $V_{\text{ap}} = 0$) for ions that are either fixed or mobile. In the left panel, positively-charged halide ion vacancies are stationary, fixed in a uniform distribution. As the negatively-charged cation vacancies are also fixed in a uniform distribution, ionic contributions to the potential landscape cancel out. Note the existence of vacancies may affect the device in other ways, such as by weakening the lattice or acting as recombination sites, but we do not directly consider this here. In the absence of moving ions, a strong electric field develops within the perovskite layer, as can be seen by the tilted conduction and valence bands. This field acts to separate electrons and holes, sweeping them into their respective transport layers.

When the halide vacancies are allowed to move, a layer of vacancies forms next to the interface with the HTL and another layer depleted of vacancies forms next to the ETL. These ionic layers, known as Debye layers, are of equal and opposite charge. The charge in each ionic Debye layer induces electronic Debye layers to

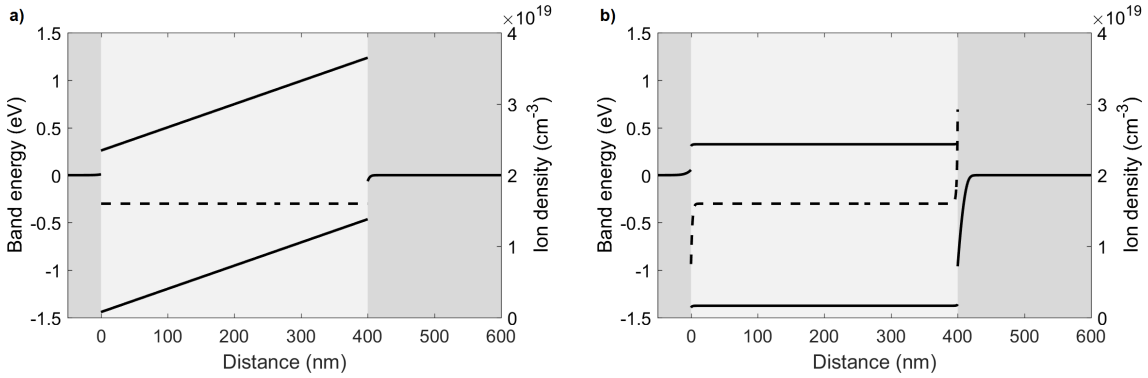

Figure 4.1: Band energies relative to the left electrode (solid lines) and halide vacancy density (dashed lines) for a PSC held at short-circuit, calculated using the model. Perovskite layer denoted by light grey, ETL and HTL by darker grey. Left panel: halide vacancies are fixed in a uniform distribution. A large electric field exisits within the perovskite layer which acts to separate electrons and holes. Right panel: halide vacancies are mobile. Debye layers have formed, screening the electric field within the bulk of the perovskite layer.

form within the transport layers. Note *electronic* in this sense includes holes. The combination of ionic and electronic Debye layers screen the built-in field within the perovskite. While the total potential difference between electrodes is the same, the locations in the device where the drops occur change. Without moving ions there was a roughly linear potential change across the entire perovskite layer, whereas with moving ions the majority of the drop occurs at the interfaces with roughly flat bands within the perovskite bulk. For this device, most of the drop occurs within the HTL, due to a combination of the low permittivity and low doping of this layer.

The ions have an equilibrium distribution where the built-in field within the perovskite bulk is fully screened for any applied voltage. Any unscreened bulk field drives more ions into the Debye layers until the field is fully screened. The vacancy distribution will always relax towards the equilibrium of no bulk field. This lack of bulk field impedes carrier separation and extraction from the active layer. If the applied voltage is reduced, so that the layers are charged more than the equilibrium for that voltage, the bulk field will point in the opposite 'wrong' direction. This negative bulk field drives the ions out of the layers and back into the bulk until the new equilibrium is reached with zero bulk field. In the meantime, the negative field pushes carriers towards the wrong sides of the active layer, making separation very inefficient.

4.2 Current-voltage curve

Ion motion becomes considerably more interesting with the appreciation that the Debye layers do not form instantly. The ion distribution in Figure 4.1 takes time of the order of seconds to minutes to fully form. Ion motion alone is not enough to cause hysteresis – it is the lag between the applied voltage as a function of time and how charged the layers are that does. Figure 4.2 shows simulated J-V curves for a TiO_2/$MAPbI_3$/spiro PSC at 300 K for scans that are very slow (1 mV/s), very fast (100 V/s) and typical of a standard laboratory measurement (320 mV/s). To

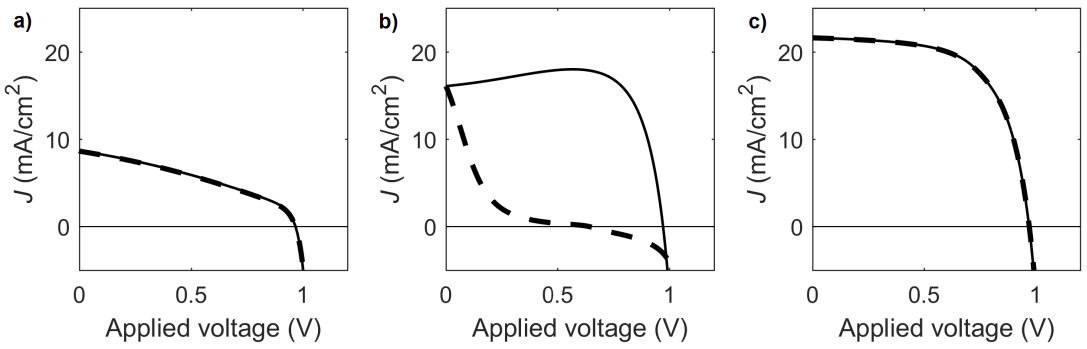

Figure 4.2: Simulated J-V scans for a TiO_2/$MAPbI_3$/spiro PSC at 300 K at (a) 1 mV/s, (b) 320 mV/s and (c) 100 V/s. In each case, the applied voltage V_{ap} is varied linearly from 1.05 V down to 0 V and immediately back up to 1.05 V. Solid lines denote the down scan (1.05 V to 0 V) and dashed lines the up scan (0 V to 1.05 V). Neither the slow nor fast scan exhibits hysteresis, although the slow scan has poorest performance. Hysteresis is present for the intermediate scan rate.

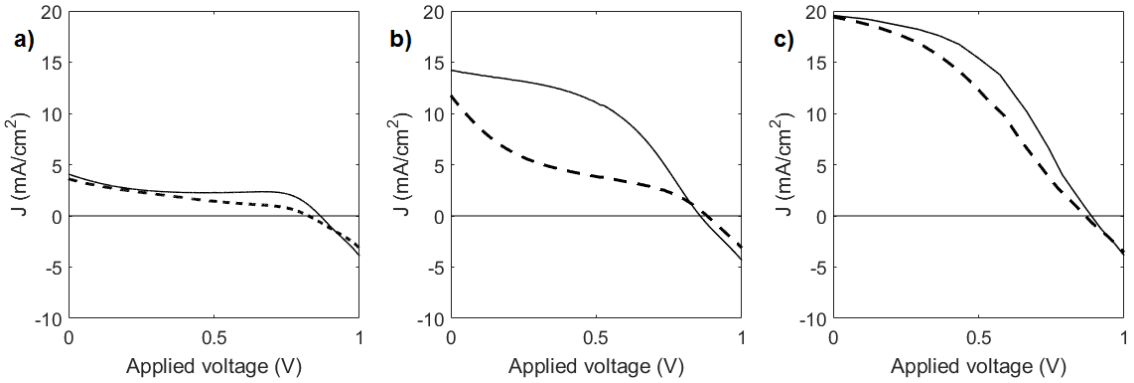

Figure 4.3: Experimental J-V scans for a TiO_2/$MAPbI_3$/spiro PSC at (a) 1 mV/s, (b) 75 mV/s and (c) 1 V/s, measured by collaborators at CSIRO.

simulate a J-V curve, the device is initially held at the built-in voltage of 1.05 V for 5 minutes under illumination. This ensures the vacancies are uniformly distributed to begin with. In practice, the initial preconditioning voltage is above the built-in voltage to ensure that open-circuit is measured – the effect of doing this is considered later. Then the applied voltage V_{ap} is swept linearly downwards to 0 V at the appropriate scan rate. The current measured during this part of the procedure is the down scan, or reverse scan. At $V_{ap} = 0$ V, the measured current is the short-circuit current J_{SC}. Once reaching 0 V, the applied voltage is immediately swept back up to 1.05 V linearly at the same rate. The current during this half of the sweep is the up scan, or forward scan. Figure 4.3 shows experimental J-V curves for the same device architecture, measured at CSIRO.

For the very fast scan, the J-V curve is virtually identical as for when the ions are immobile, and no hysteresis is exhibited. This is because the low diffusivity/mobility of the halide vacancies means the ion distribution is essentially fixed on this very fast timescale. When the ions are fixed, there is no dependence on scan rate or direction as carrier motion is sufficiently fast relative to any feasible scan rate that the electron and hole distributions are relaxed into a steady-state at all points in

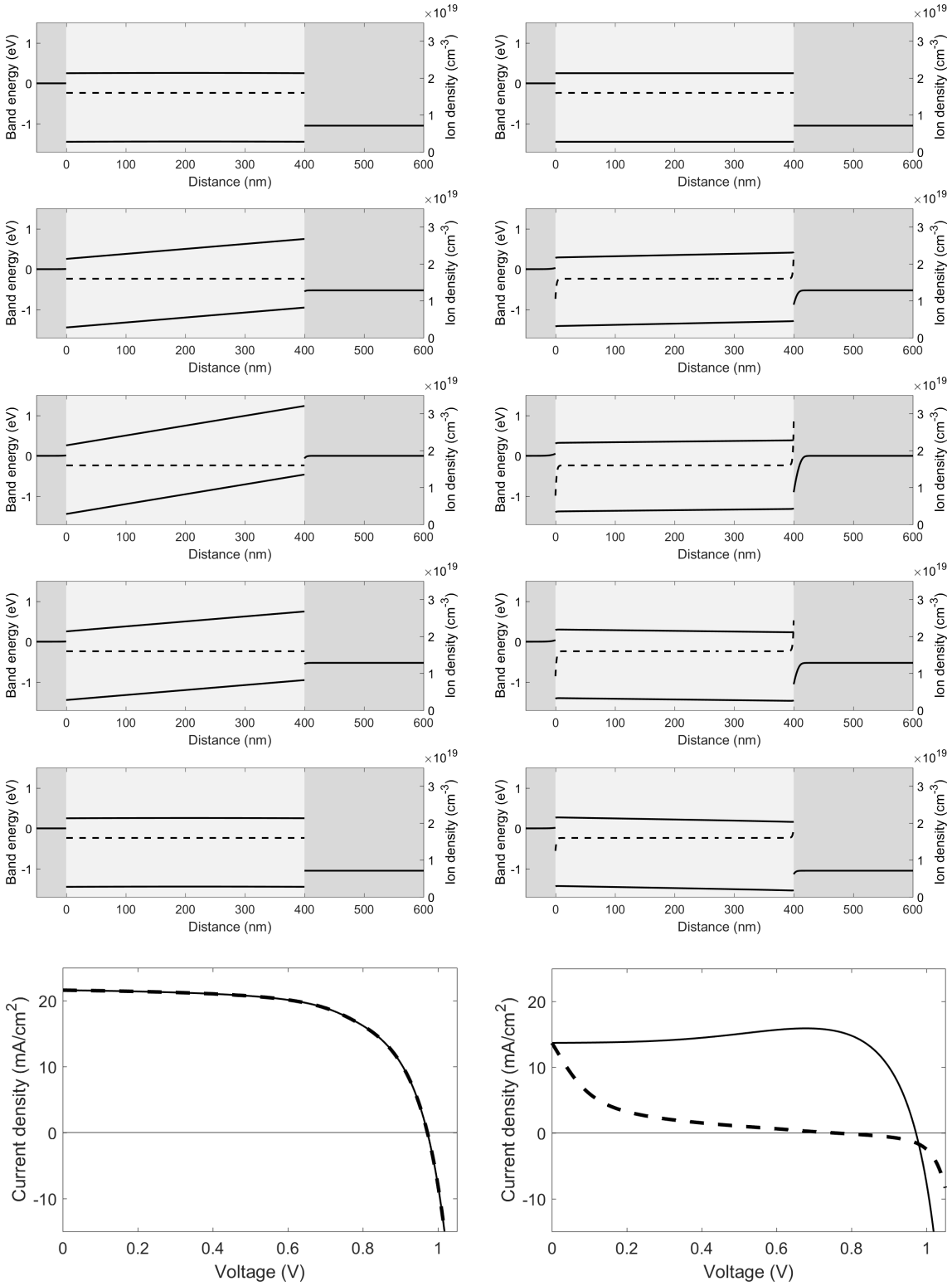

Figure 4.4: Band energies (solid lines, left axes) and halide vacancy density (dashed lines, right axes) for a PSC at five points evenly spaced throughout a J-V scan at 200 mV/s, with fixed ions (left column) and with mobile ions (right column). Top row, $V_{\mathrm{ap}} = V_{\mathrm{bi}} = 1.05$ V at the start of the scan; second row, $V_{\mathrm{ap}} = 0.525$ V on the down scan; third row, $V_{\mathrm{ap}} = 0$ V, where the scan changes direction; fourth row, $V_{\mathrm{ap}} = 0.525$ V on the up scan; fifth row, $V_{\mathrm{ap}} = V_{\mathrm{bi}}$ at the end of the scan; sixth row, full J-V curves.

the scan. When the scan rate is very slow, the ion motion is also sufficiently fast relative to the scan such that the ion distribution is relaxed throughout the whole scan. Essentially, the ions can keep up with the scan and fully screen the bulk electric field in the interior of the perovskite layer. The distribution of ions depends on the voltage but not on scan direction, so there is no hysteresis. However, the screening of the bulk field reduces device performance, very severely in some cases, as seen by the very poor J_{SC} and fill factor.

For the moderate scan rate, hysteresis is present. Here, the timescale of the J-V sweep is comparable to the timescale for ion motion. At these scan rates, the ions are fast enough to move significantly from their starting distribution over the course of the scan, but not fast enough to fully relax. Figure 4.4 shows the band structure and ion distribution for such a sweep, for the same device with and without mobile ions. The key point is that the charging of the Debye layers lags behind the scan. During the down scan, the layers are not quite charged enough to fully screen the field (Figure 4.4b). The bulk field in the perovskite is reduced, but still present and pointing in the correct direction. The current is reduced significantly. On the up scan, the layers are too heavily charged to perfectly screen the field. The bulk field is not simply cancelled, but reversed (Figure 4.4d). The current is severely hampered, as now the carriers must rely on just diffusion to separate and overcome drift in the wrong direction. Note the current on the way up with negative field is actually *worse* than for the very slow scans where the field is 'only' zero. The size of the Debye layers depends not only on the applied voltage at some given time, but also on the scan direction. The currents on the down and up scans diverge, giving rise to hysteresis.

Videos of these J-V curves are available as part of the supplementary material for this thesis. The slow, moderate and fast scans are shown in supplementary videos 1, 2 and 3 respectively. Each video consists of four panels that update as the scan progresses. The upper-left panel shows the electric potential (black) and ion vacancy density (magenta) profiles throughout the device as time evolves. ETL, perovskite and HTL are depicted in blue, yellow and red respectively. The simulation time is displayed above this panel, with the J-V scan starting at t=300 s due to the 5 minute equilibration at the beginning.

The upper-right panel shows the band energies through the device, using the layer colour scheme from the previous panel. Within the perovskite layer, the valence band maximum (electron energy, lower line) and condution band minimum (hole energy, upper line) are shown. Within the ETL only the conduction band is plotted, as holes are not permitted to enter this layer. Similarly within the HTL, only the valence band is plotted. The lower-left panel shows the J-V curve plotted over time, with the down scan denoted by a solid line and the up scan by a dashed line. The measured current at time t is denoted by a circle. The lower-right panel shows the electric field at the centre of the perovskite layer. As with the J-V plot, down scan values are denoted by a solid line, up scan values by a dashed line and the value at time t by a circle. Positive field is defined as driving carriers towards their corresponding transport layers.

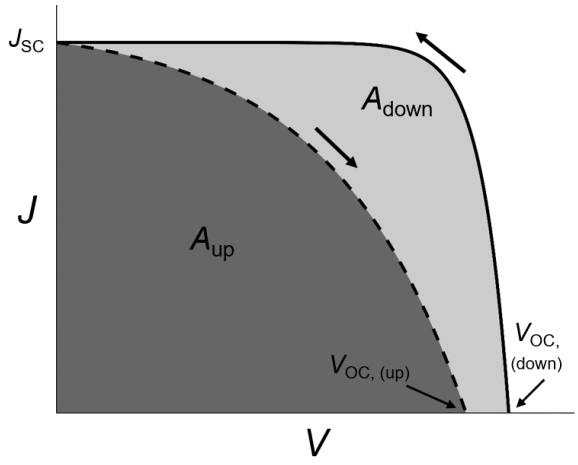

Figure 4.5: A J-V curve from forward bias, down to J_{SC} (solid line) and back up (dashed line). The area under the up scan A_{up} is the dark shaded area, while the area under the down scan A_{down} is the sum of the two shaded areas. Hysteresis factor $\mathcal{H}$ is calculated using (4.1), and is equal to the area of the light shaded region as a fraction of the sum of the areas of both shaded regions.

4.3 Quantifying dependence on scan rate

While we have found three qualitative regimes of hysteresis in Figures 4.2 and 4.3, it is interesting to quantify the dependence of hysteresis on scan rate. To this end, we can define a hysteresis factor, or $\mathcal{H}$-factor, as

$$\mathcal{H} = \frac{A_{\text{down}} - A_{\text{up}}}{A_{\text{down}}} \tag{4.1}$$

where A_{down} and A_{up} are the areas under the down and up scans respectively. More specifically, A is the area enclosed by the lines $J(V)$, $J = 0$ and $V = 0$ defined by

$$A = \int_0^{V_{\text{OC}}} J(V)\ \mathrm{d}V \tag{4.2}$$

so that $\mathcal{H}$ is just the relative change between the areas enclosed by the up and down scans and the J and V axes. $\mathcal{H}$ is 0 if there is no hysteresis and is positive but less than 1 for a hysteretic curve. if $\mathcal{H}$ is negative, the up scan is better than the down scan.

Figure 4.6 shows the $\mathcal{H}$-factor, short-circuit current J_{SC}, power conversion efficiency PCE and fill factor FF for the simulated device at 300 K for a set of scan rates in the range 100 µV/s to 100 V/s. J_{SC} is simply the current density J when the applied voltage is zero, and the J-V sweep changes direction. This is the point in the scan where the down scan ends and the up scan begins. PCE, as in (1.1), is calculated from the full J-V curve as

$$\text{PCE} = \frac{J_{\text{max}} V_{\text{max}}}{P_{\text{irr}}} \tag{4.3}$$

where V_{max} and J_{max} are the voltage and current at maximum power point respectively and the incident irradiated power P_{irr} for one sun is approximately 1 kW/m^2

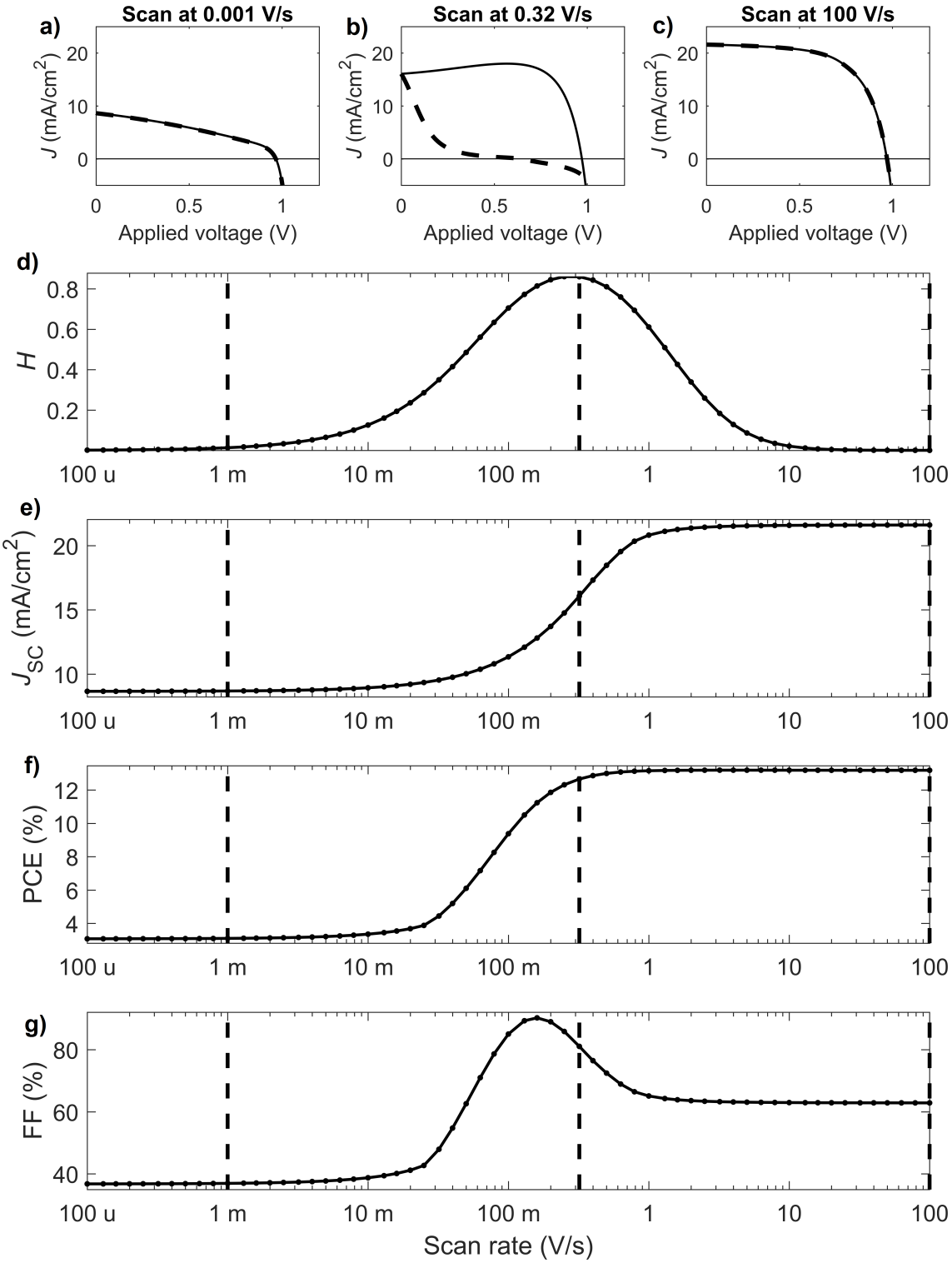

Figure 4.6: (a)-(c) Simulated J-V curves for scan rates 1 mV/s, 320 mV/s and 100 V/s, as discussed in Figure 4.2. (d) $\mathcal{H}$-factor, (e) J_{SC}, (f) PCE and (g) FF for the simulated planar TiO_2/$MAPbI_3$/spiro device at 300 K for a range of scan rates spaced logarithmically between 100 µV/s and 100 V/s. The PCE and FF are calculated from the max power point on the down scan. For (d)-(g), the points corresponding to the scans (a)-(c) are depicted by vertical dashed lines.

or 100 mAV/cm^2. The fill factor FF is calculated from

$$\mathrm{FF} = \frac{V_{\max} J_{\max}}{V_{\mathrm{OC}} J_{\mathrm{SC}}} \tag{4.4}$$

using the same max power point and open-circuit voltage V_{OC} from the down scan.

There is no hysteresis for the extremal scan rates, with intermediate rates yielding significant hysteresis. There is a smooth transition between regimes, with the $\mathcal{H}$ against scan rate plot roughly approximating a Gaussian or bell curve. The short-circuit current and power conversion efficiency exhibit sigmoidally-shaped plots, with the three hysteresis regimes clearly visible. The best J_{SC} and PCE are obtained for faster scan rates as the ions have not had time to redistribute to shield the electric field. For slow scan rates the worst J_{SC} and PCE are observed, as the ions are fully screening the field. For intermediate scan rates, the fields once J_{SC} and max power point (for PCE) are reached are partially screened, giving currents and efficiencies part way between the two extremes. The V_{OC} was found to not vary significantly with scan rate, so is not shown.

The shape of the fill factor appears to be almost a hybrid of a bell curve and sigmoid, with a flat low FF regime for low scan rate, a flat high FF regime for fast scan rate and a bump with the maximum FF forming the transition between the two. As discussed previously, the device properties at high scan rate are representative of the device when the ions are stationary. For this device, the fast scan fill factor at 300 K is a respectable 63%. For slow scan rates the ions are fully screening the built-in field, hindering charge separation and this increasing recombination. The rather disappointing fill factor for low scan rates of 37% reflects this increased recombination, symptomatic of large resistive losses. Of particular interest is the bump in the transition region – specifically the peak FF of about 90%, higher even than high performance crystalline GaAs which might achieve 87% [4]. The reason for this is the bump in the down scan of some hysteretic J-V curves, visible in Figure 4.6b. In this case, the current at maximum power point may actually *exceed* the short-circuit current. The concept of fill factor as a measure J-V curve squareness, and by extension performance, assumes the cell is behaving as a diode plus a constant. The apparent heroic performance here is actually a consequence of poor J_{SC}, rather than excellent performance at maximum power point.

These results are of considerable significance to the accurate characterisation of perovskite solar cells. Many published articles trumpet that their devices are hysteresis-free, yet only provide a single J-V scan at a single rate as evidence. For example, a Google Scholar search for hysteresis-free perovskite solar lists about 1,000 items from the start of 2017 to August 2018. However, as in Figure 4.6d, if such a device is scanned either very quickly or very slowly compared to the timescale of ion motion then no hysteresis would be expected. If this is the case, important behaviour is being missed. For devices scanned too slowly or too quickly to observe the hysteresis, a potentially important source of loss may still be present but going unnoticed. Identifying if this is the case is important so that strategies can be devised to tackle this problem, if possible. Perovskite devices should be measured at a wide range of scan rates, ideally over several orders of magnitude, to check for hysteresis before being declared hysteresis-free. In the same manner as hysteresis itself was used to inflate reported device performance in the early days of PSC research [2] by only reporting the better performing down scan, exploiting a single scan to allege the absence of hysteresis has become ingrained in the field today.

From a practical point of view, a J-V curve is measured in order to characterise how well a device will perform at generating power. After all, a solar module in the field will not undergo voltage sweeps – rather, it will be held at maximum power point. When held at a single voltage the Debye layers will have ample time to reach equilibrium distribution, so a very slow scan is best representative of operating performance. Specifically for devices that are scanned too quickly, metrics extracted from the J-V characteristic will not be representative of operating performance. To extract PCE from a J-V curve, the point on the curve representing the greatest product of voltage and current is used. This method will overestimate the device performance for anything other than very slow scans, as shown in Figure 4.6f. If the fill factor is calculated from a hysteretic down scan, an anomalously high value may be obtained. Stabilised power conversion efficiency measurements, where the device is held at maximum power point until the current (and therefore ion distribution) settles, are a good way of dealing with these measurement problems.

4.4 Dependence on temperature – speeding the ions up

In the previous section, we concluded that it is important to understand the timescale of ion motion in PSCs. When we apply a stimulus to the system in the form of a J-V scan, we can expect hysteresis only if the frequency of the scan is comparable to that of ion motion. There is an immediate, if slightly tenuous, parallel with resonance, in that when we apply a stimulus to a system we expect a strong response only if the stimulus is of similar frequency to the natural frequency of the system. The frequency of the stimulus in this case is obviously related to the scan rate of the J-V curve, but the frequency corresponding to the system is more subtle. So what determines the ionic timescale? From our understanding developed thus far we can suggest a few possible factors, then use the model to quickly test the effect (if any) of each.

Perhaps the most obvious factor is the mobility of the ions, as the faster the ions move the faster they can respond to a change in applied voltage. As ion hopping is an Arrhenius process, the vacancies have a diffusivity of the form

$$D_P = D_P^{\infty} \exp\left(-\frac{E_{\mathrm{A}}}{k_{\mathrm{B}}T}\right) \tag{4.5}$$

with some activation energy E_{A} and high temperature limit D_P^{∞}. Due to the exponential dependence, the ion mobility is highly sensitive to temperature. Different perovskite chemistries (e.g. $MAPbI_3$, $FAPbI_3$, $MAPbBr_3$) will have different activation energies, depending on the A and B site cations and halide or mixtures thereof. In practice, the quality of the film also influences the effective diffusivity through the relative prevalence and form of grain boundaries in the perovskite. High quality film tend to have larger grains, and may be expected to behave closer to an idealised lattice. Films with with small grains have more grain boundary regions where the constituent ions do not form a lattice. As it is not possible to describe this properly in the one dimensional model, here we shall abstract this into different E_{A} and D_P^{∞} values in (4.5).

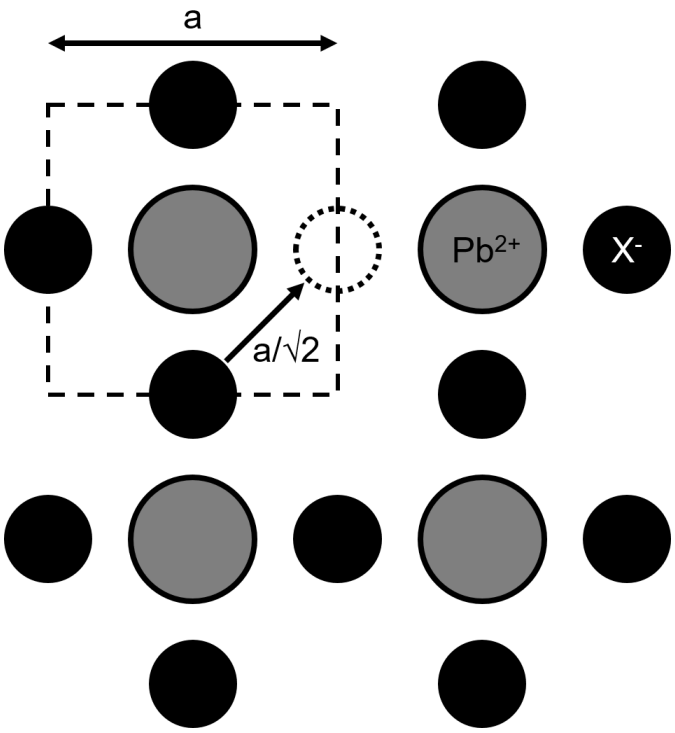

Figure 4.7: Diagram of the Pb-X plane in a lead halide perovskite in the cubic phase. Lead ions are drawn as grey circles, halides as black circles. The unit cell is indicated by the dashed line, with lattice parameter a. The distance between neighbouring halide sites, as for the small arrow between a halide and a vacancy (dotted line), is $a/\sqrt{2}$.

The high temperature diffusivity D_P^∞, the value of D_P when $T = \infty$ in (4.5), is a constant prefactor that we fit to experiment. Taking the motion of a vacancy as a random walk on a cubic lattice, the diffusivity may be calculated from

$$D_P = \frac{h^2}{6\delta t} \tag{4.6}$$

where h is the lattice spacing and δt the average time between hops. In reality, the motion of the (charged) ions cannot be a true random walk because the ions are interacting. However, as the uniform ion density is around 0.4% of sites and in the following simulations never exceeds about 1%, this is a reasonable approximation. The lattice spacing for the $MAPbI_3$ unit cell in the cubic phase is around $a = 0.63$ nm [51, 79], so the hop distance between neighbouring halide sites, illustrated in Figure 4.7, is $h = a/\sqrt{2}$ or around 0.45 nm. As halide hopping is a barrier hopping process, the hop frequency $1/\delta t$ can be expressed as the product of an attempt frequency f_a and the probability that the hop is successful,

$$1/\delta t = f_\mathrm{a} \exp\left(-\frac{E_\mathrm{A}}{k_\mathrm{B}T}\right), \tag{4.7}$$

where the attempt frequency is usually taken as a typical phonon frequency, about 1 THz [51]. Combining (4.6) and (4.7), we find

$$D_P = \frac{a^2 f_\mathrm{a}}{12} \exp\left(-\frac{E_\mathrm{A}}{k_\mathrm{B}T}\right). \tag{4.8}$$

Through inspection with (4.5), we can then estimate the high-temperature diffusivity as

$$D_P^{\infty} = \frac{a^2 f_{\mathrm{a}}}{12}. \tag{4.9}$$

For $f_{\mathrm{a}} = 1$ THz and $a = 0.63$ nm, we obtain an estimate of 3×10^{-8} m^2/s. Most perovskites are in the tetragonal phase at room temperature, where the lattice parameters $a = b \neq c$, but provided $a = b$ and c aren't too different we can just take a as an approximate quasi-cubic lattice parameter. A calculated D_{∞} is only a very rough approximation then, due to the error in both a and f_{a}. Additionally, boundaries between perovskite grains and the differing orientations of the grains themselves will affect halide motion in a way not described by (4.9). Still, (4.9) provides an order of magnitude estimate for D_P^{∞}.

To model how device behaviour varies with temperature, we now set the diffusivity of the ions to be dependent on temperature using (4.5). Here, we take $E_{\mathrm{A}} = 0.58$ eV as calculated from DFT [51], with $D_P^{\infty} = 10^{-7}$ m^2/s as an order of magnitude estimate to give roughly the right value for D_P at 320 K from the same reference. In all subsequent calculations, we use these two values in (4.5) to find D_P. For this section, N_0 is not varied with temperature. To extend the map of $\mathcal{H}$, J_{SC} and PCE against scan rate out into temperature space, 915 simulated J-V curves were run for 15 temperatures spaced uniformly in the range 270 to 340 K (every 5 K). 61 scan rates were simulated for each temperature, rates spaced logarithmically between 100 µV/s and 100 V/s (10 rates per decade). This sweep ran overnight on a high-end desktop machine (Intel i7-4790 quad-core processor at 3.60 GHz, 32.0 GB RAM) taking 10 hours and 16 minutes in total. Each curve took about $2\frac{1}{2}$ to 3 minutes each, with the jobs parallelised over 4 workers using a MATLAB built-in `parfor` loop. Figure 4.8 shows the effect on the $\mathcal{H}$, J_{SC}, PCE, V_{OC} and FF against scan rate curves of the simulated device for a range of temperatures.

As seen in Figure 4.8, the plots of $\mathcal{H}$, J_{SC}, PCE and FF are shifted to higher scan rate as temperature is increased. Higher temperature increases the diffusivity of the ions, and therefore decreases the timescale of ion motion. A faster scan rate is needed for the timescales of the scan and of the ions to still be aligned. The increase in temperature worsens the J_{SC} for anything other than the fastest scan rates, and also decreases FF once the timescale shift is accounted for. V_{OC}, which is roughly constant with scan rate, decreases with temperature. There is a very slight increase in V_{OC} for hysteretic scans, which shifts to higher scan rates with temperature. Due to the decrease in V_{OC} and FF, increasing temperature harms PCE at all scan rates. For slow scan rates, the decrease in J_{SC} leads to a proportionally greater reduction in PCE. The worsening of all performance characteristics with temperature for this device is due to additional bulk recombination.

Figure 4.9 shows contour plots of these same five measures against scan rate and temperature for the full dataset. On each these plots, the hysteresis regime where the timescale of ion motion aligns with the timescale of the scan is obvious. For Figure 4.9(a), there is a thick diagonal band where hysteresis is present. In panel (e), the region of augmented fill factor coincides with the hysteresis region. For panels (b) and (c), the hysteresis region coincides with the transition from low to high values of J_{SC} and PCE. The regime is most subtle for V_{OC} in panel (d), although a diagonal ripple is visible.

The steepness of the diagonal bands in the panels of Figure 4.9 depends on

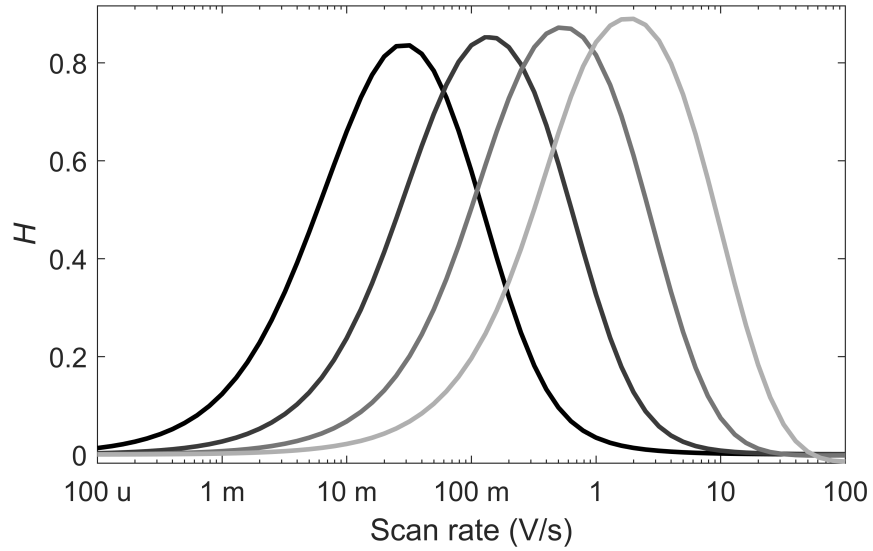
0.8
0.6
H
0.4
0.2
0
100 u
1 m
10 m
100 m
1
10
100
Scan rate (V/s)

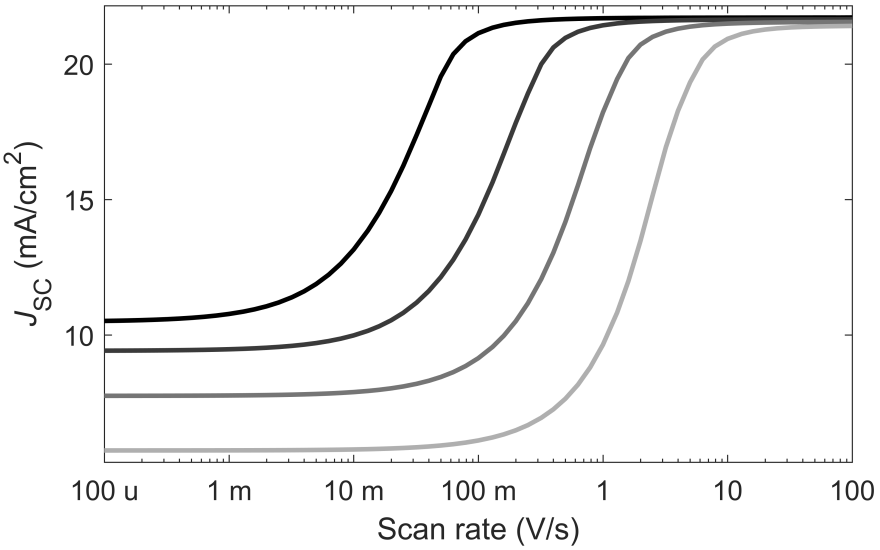
20
15
J_{SC} (mA/cm^2)
10
100 u
1 m
10 m
100 m
1
10
100
Scan rate (V/s)

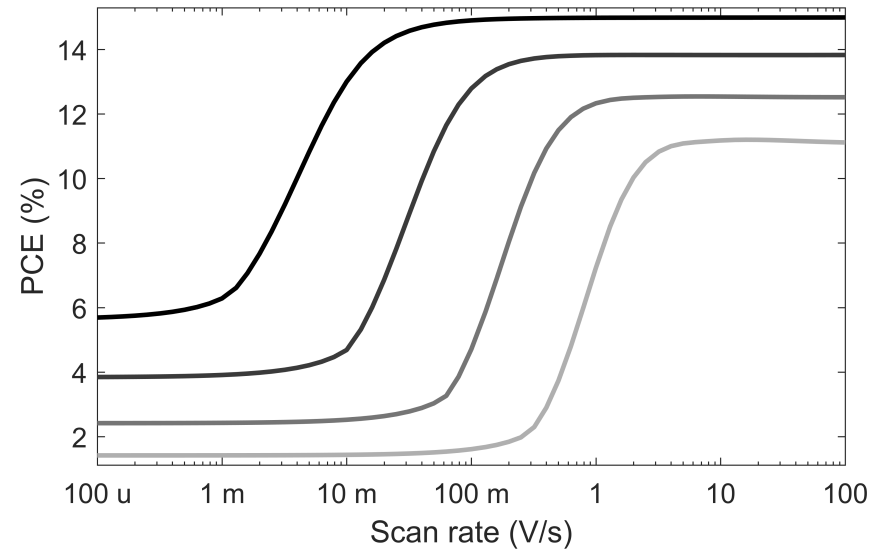
14
12
10
8
PCE (%)
6
4
2
100 u
1 m
10 m
100 m
1
10
100
Scan rate (V/s)

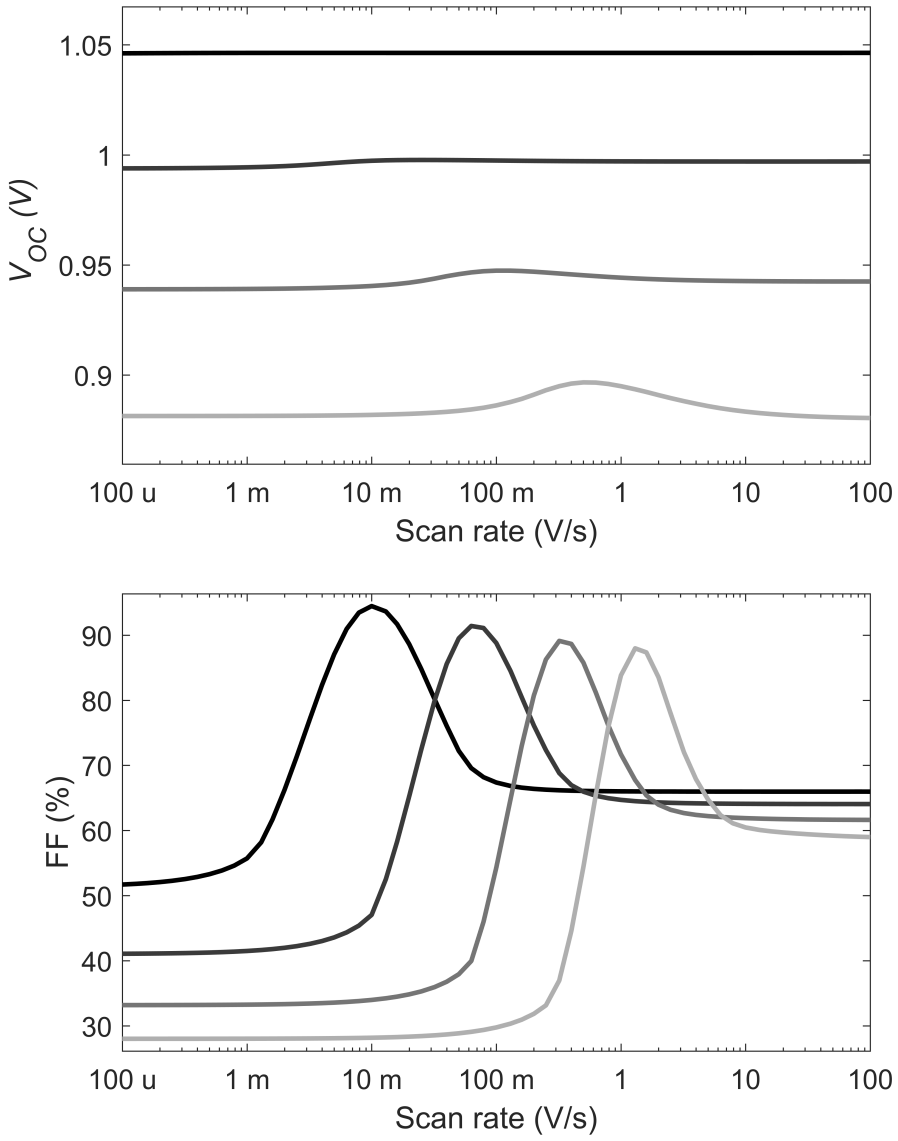

Figure 4.8: $\mathcal{H}$-factor, J_{SC}, PCE, V_{OC} and FF as a function of scan rate for temperatures 270, 290, 310 and 330 K (increasing temperature black to light). 15 temperatures in the range 270 to 340 K inclusive at 5 K intervals were simulated, although only four values are shown in (a)-(c) for clarity. 61 scan rates spaced logarithmically between 100 µV/s to 100 V/s inclusive (10 per decade) were simulated for each temperature.

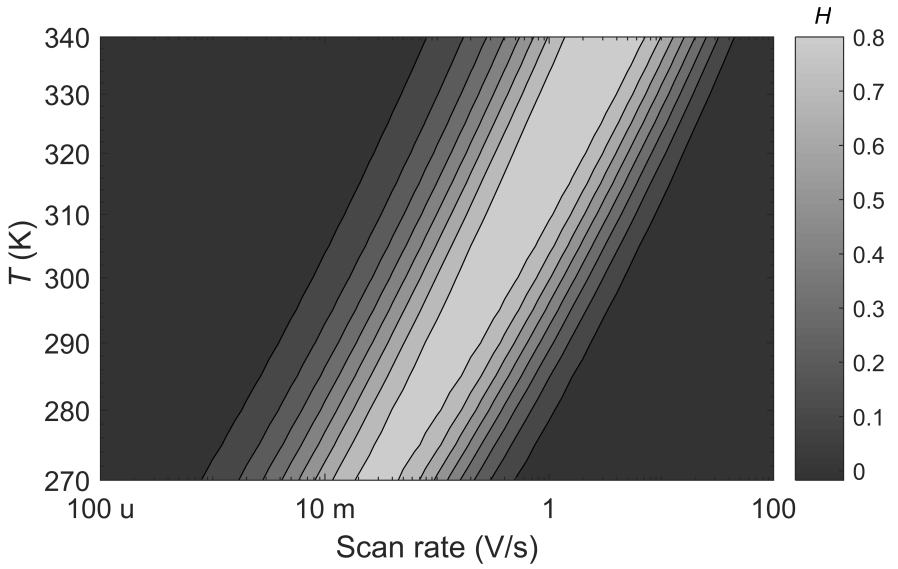
H
0.8
0.7
0.6
0.5
0.4
0.3
0.2
0.1
0
340
330
320
310
300
290
280
270
T (K)
100 u
10 m
1
100
Scan rate (V/s)

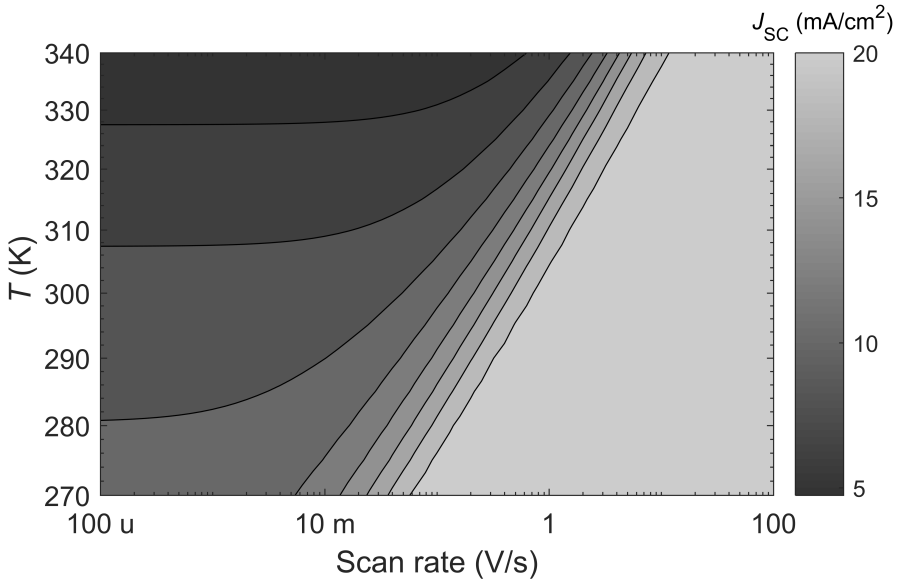
J_{SC} (mA/cm^2)
20
15
10
5
340
330
320
310
300
290
280
270
T (K)
100 u
10 m
1
100
Scan rate (V/s)

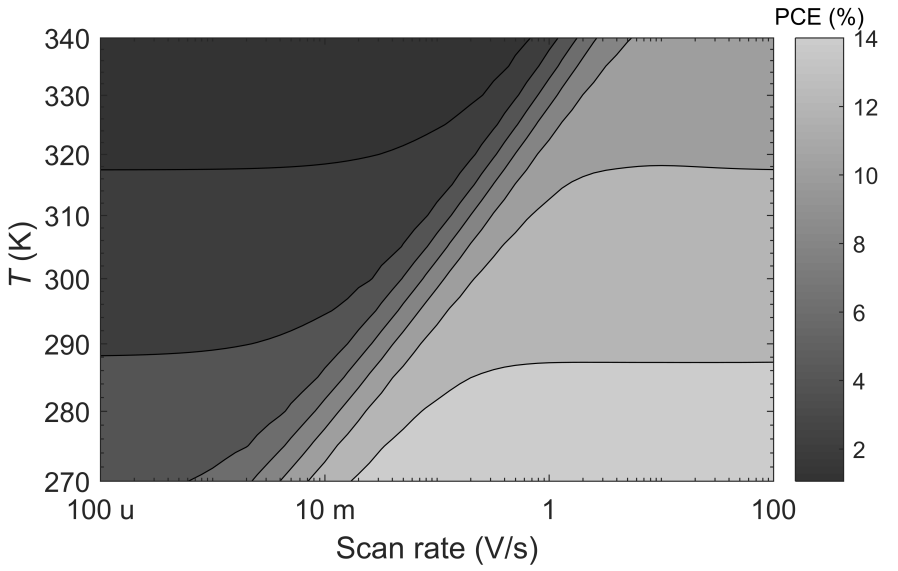
PCE (%)
14
12
10
8
6
4
2
340
330
320
310
300
290
280
270
T (K)
100 u
10 m
1
100
Scan rate (V/s)

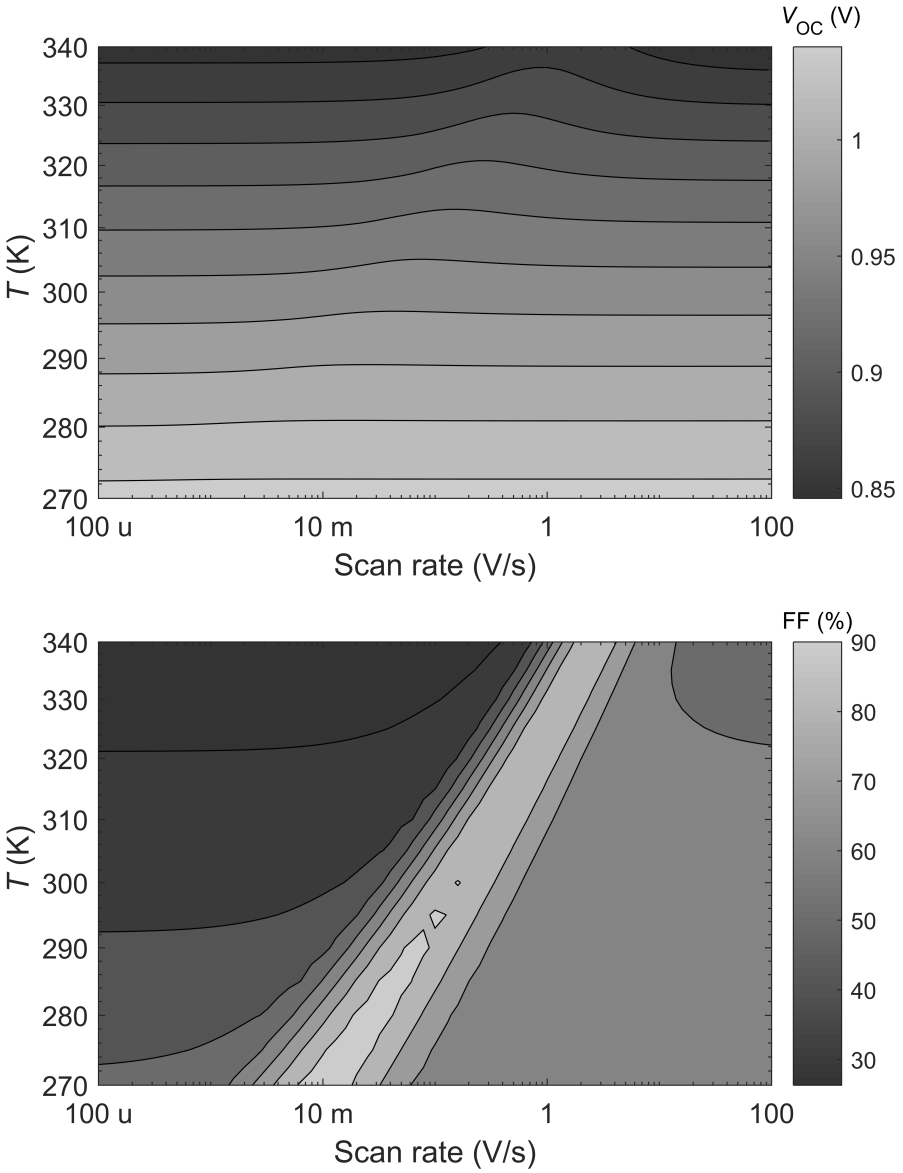

Figure 4.9: Variation in $\mathcal{H}$-factor, J_{SC}, PCE, V_{OC} and FF with scan rate and temperature T on log-log axes. PCE, V_{OC} and FF are each calculated for the down scan. The gradient of the diagonal bands in (a)-(c) and (e) correspond to the activation energies obtained in Figure 4.10. The plots in Figure 4.8 are cut-throughs of horizontal lines on these graphs.

how sensitively the timescale of ion motion depends on temperature. Due to the Arrhenius form of ionic diffusivity D_P, the key parameter controlling the steepness is the activation energy E_A. Assuming that the system response, represented by some measure R, is proportional to the D_P, and that D_P is the only parameter with an Arrhenius form, we may write

$$R \propto \exp\left(-\frac{E_\mathrm{A}}{k_\mathrm{B}T}\right). \tag{4.10}$$

Taking the natural logarithm of both sides and rearranging, we find

$$\ln R = -\frac{E_\mathrm{A}}{k_\mathrm{B}T} + \text{const.} \tag{4.11}$$

For some sensible definition of R, a plot of $\ln R$ against $1/k_\mathrm{B}T$, or Arrhenius plot, will have a gradient of -E_A. This gives us a way of deducing the activation energy from a set of J-V curves.

For hysteresis, we here choose $R(T)$ to be the scan rate that yields maximum $\mathcal{H}$ for a particular temperature T. This corresponds to the peaks in Figure 4.8a and the centre of the bands in Figure 4.9a. Similarly for fill factor, we choose R to be the scan rate giving maximum FF. For the sigmoidal J_SC and PCE curves with a plateau at high scan rate, an obvious maximum is not present. Instead for J_SC and PCE, we take $R(T)$ as the scan rate yielding 90% of the value of the measure at the fast scan rate plateau. For a particular J_SC sigmoid for example, R is the scan rate satisfying $J_\mathrm{SC}(R,T) = 0.9\ J_\mathrm{SC}(100\ \mathrm{V/s}, T)$.

Figure 4.10 shows the Arrhenius plots and fits for the modelled data. Activation energies inferred from the gradients are tabulated in Table 4.1. The most accurate method is a fit to J_SC, with an error of just 1.4%. By contrast, the other methods give at least a 7.8% error. The discrepancies here are likely due to some combination of the assumption (4.10) not being strictly true and poor fitting. However, even an error of $\sim$10% is rather good. The use of modelling here gives us a reliable and repeatable way of testing this method to check it is measuring the activation energy as we expect. By analysing the macroscopic device behaviour we are able to make a statement about the microscopic phenomenon of ion motion, which is pleasing.

An alternative method for fitting the sigmoids is to first subtract the low scan rate limit before normalising, as depicted in Figure 4.11. In this way, R is taken as 90% of the total *change* in J_SC or PCE over the measured scan rate rather than of the absolute value of the highest scan rate. Including subtraction yields activation energies of 0.56 eV for J_SC and 0.62 eV for PCE, compared to 0.59 eV and 0.65 eV without subtraction respectively. This advantage of this method is that rescaling all the sigmoids to range from 0 to 1 might be expected to give a better fit to the total shift on the scan rate axis. However, this method only changes the calculated E_A by 30 meV and requires knowledge of both the high and low scan rate J_SC values. Experimentally, measuring the low scan rate plateau is found to need extremely slow scan rates <1 mV/s. As part of this measurement, the PSC being measured will need to be under constant operation under illumination for a number of hours, much of this near short-circuit, causing significant device degradation. As a result, fitting to 90% of the absolute value is the better approach. A major advantage of the model is that low scan rate regimes can be explored without having to worry about the fragility of the material.

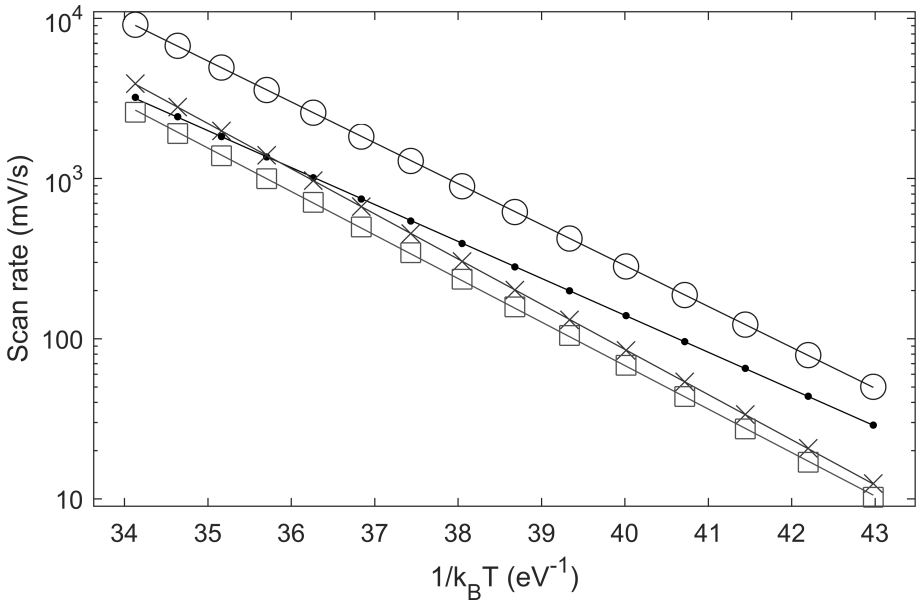

Figure 4.10: Arrhenius plot of the scan rates yielding maximum $\mathcal{H}$ (dots), 90% of maximum J_{SC} (circles), 90% of maximum PCE (crosses) and maximum FF (squares). Activation energies inferred from gradients are tabulated in Table 4.1.

Measure	R	Inferred E_{A} (eV)	Error (%)
$\mathcal{H}$	Maximum value	0.5310	-8.4
J_{SC}	90% of high rate limit	0.5881	1.4
PCE	90% of high rate limit	0.6495	12
FF	Maximum value	0.6255	7.8

Table 4.1: Values for the activation energy of halide motion inferred from the shift in hysteresis factor $\mathcal{H}$, short-circuit current J_{SC}, power conversion efficiency PCE and fill factor FF. For $\mathcal{H}$ and FF, the scan rate yielding the maximum value was taken as the measure of system response R; for J_{SC} and PCE, the scan rate giving 90% of the value at the highest simulated scan rate of 100 V/s is taken. The error between each inferred E_{A} and the true value input into the model, 0.58 eV, is also listed.

Figure 4.12 shows $\mathcal{H}$-factor and J_{SC} as measured experimentally at a range of temperatures and scan rates for four typical perovskite solar cells, along with Arrhenius fits to extract activation energies. J_{SC} is shown normalised to the high scan rate value. Perovskites $MAPbI_3$, $FAPbI_3$ and $MAPbBr_3$ with a tin oxide ETL and $MAPbI_3$ with a titania ETL were tested. Electrodes of FTO and gold and an HTL of spiro-OMeTAD were common to each devices. These devices were fabricated by collaborators at CSIRO Energy, Newcastle, Australia. Inferred activation energies from the Arrhenius plots are given in Table 4.2, along with values for each material as calculated from density functional theory. The extracted values show reasonable agreement with each other and with DFT.

The dependence of short-circuit current on scan rate (Figure 4.12, second column) shows excellent agreement with prediction, with a flat high scan rate regime observable for all devices. Measured hysteresis curves have the same qualitative

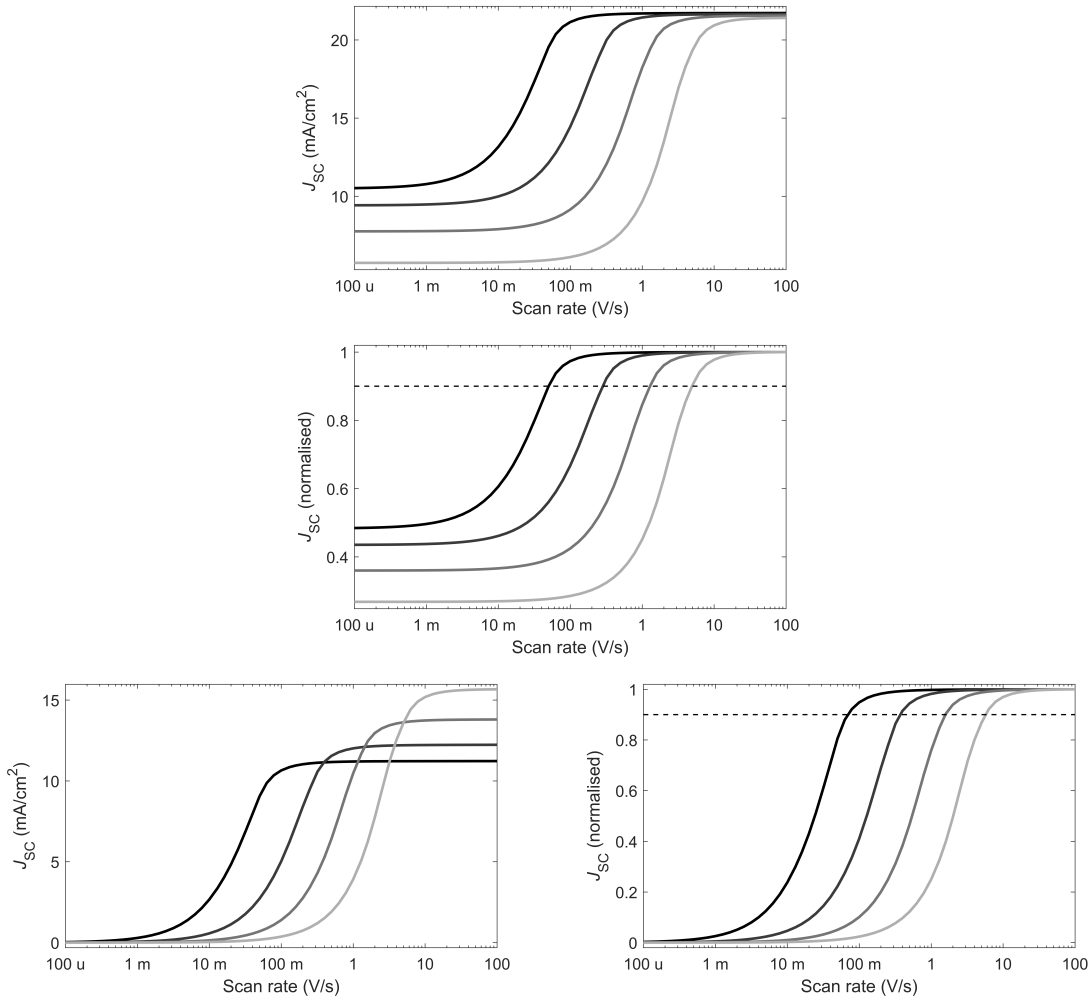

Figure 4.11: Two methods of selecting R for the sigmoidal J_{SC} against scan rate curves. The top panel shows the simulated data. In the second panel, each curve is normalised to the high scan rate value and R chosen as the scan rate giving 90% (dashed lines). This method is used in the previous plots and for the experimental data. In the bottom row of panels, the low scan rate value is first subtracted from each curve before they are normalised to the high scan rate value. This alternative method is not useful for experimental data, where the low scan rate limit is impractical to measure. The difference in inferred E_{A} between the two methods is also small.

shape as in the simulations, although with longer tails and a varying amplitude. Probable explanations for these slight discrepancies are a device memory from the previous scans and degradation; for a 1 mV/s scan rate, for example, measuring a full scan from 1.2 V requires the device to be continuously operating for 40 minutes.

As predicted, peak hysteresis is observed for the scan rates where J_{SC} varies strongly with scan rate. Importantly, this means the presence of hysteresis can be used as an indicator for whether ion motion is suppressing device performance. If hysteresis is not present when a device is measured, other scan rates and temperatures must be measured to find the hysteresis regime in order to obtain an accurate prediction of steady-state performance. For our $MAPbI_3$ and $FAPbI_3$ devices, hysteresis was still present even for extremely slow scan rates of about 1 mV/s. This

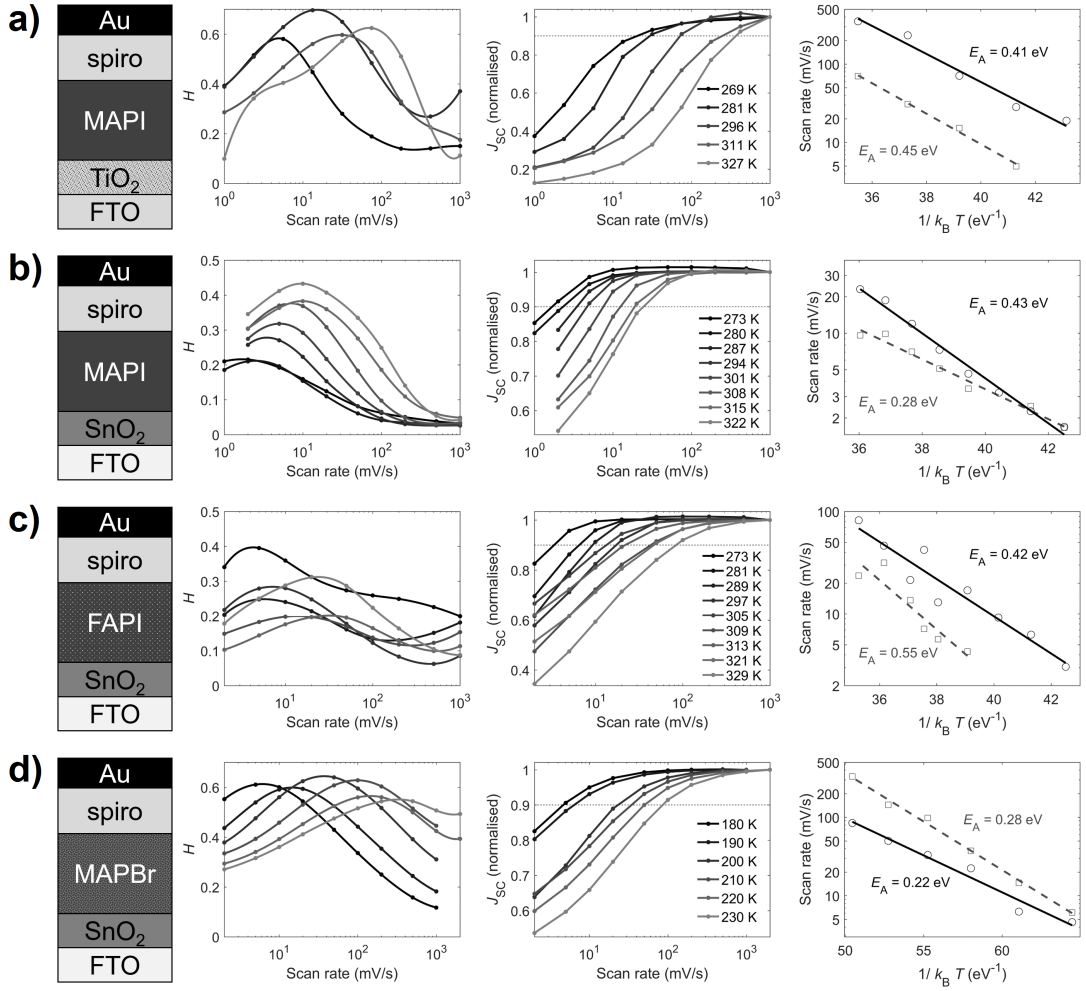

Figure 4.12: Variation of $\mathcal{H}$-factor (second column) and J_{SC} (third column) with scan rate and temperature for (a) $MAPbI_3/TiO_2$, (b) $MAPbI_3/SnO_2$, (c) $FAPbI_3/SnO_2$ and (d) $MAPbBr_3/SnO_2$. Device structures are given in the first column. The last column gives Arrhenius plots for the scan rate giving 90% of the maximum J_{SC} (black circles and solid lines) and scan rate giving maximum $\mathcal{H}$-factor (grey squares and dashed lines). Inferred activation energies are labelled next to each line and given in Table 4.2. Measurements performed by (c, d) myself, (a) IA Blakborn and (b) TW Jones at CSIRO.

Perovskite	ETL	E_{A} (eV)		
		J_{SC} shift	$\mathcal{H}$ shift	DFT
$MAPbI_3$	TiO_2	0.41	0.45	0.44
$MAPbI_3$	SnO_2	0.43	0.28	
$FAPbI_3$	SnO_2	0.42	0.55	0.45
$MAPbBr_3$	SnO_2	0.22	0.28	0.36

Table 4.2: Values for the activation energy E_{A} for halide motion inferred from the shift in hysteresis factor $\mathcal{H}$ and short-circuit current J_{SC} for the experimental devices. The E_{A} values as calculated from density functional theory (DFT) by D Ghosh at Bath are also given.

means that even these scans overestimate performance. To remedy this, so-called stabilised measurements may be used experimentally. For example, holding the device at maximum power point for the true steady-state PCE or holding at open-circuit for V_{OC}, so the property of interest can relax to a stable value.

Notably, the peak hysteresis for the $MAPbBr_3$ device occurs in the 10-100 mV/s range only at low temperatures (∼200 K). At room temperature significant hysteresis only occurs at faster scan rates than are commonly (and easily) measured. The hysteresis, and onset of J_{SC} loss, is shifted back to the 100 mV/s regime upon cooling. This effect has been observed in $MAPbI_3$ cells employing organic transport layers [80, 81].

The J_{SC} method appears to give a more reliable measure of E_A, as in the simulated data. From inspection of Figure 4.12, especially for the $FAPbI_3$ device in row (c), it is obvious that the J_{SC} plots have sharper trends than the $\mathcal{H}$ plots. This is likely because the H method depends on the entire J-V curve, the shape of which is very sensitive to a wide variety of parameters. Further, interpolating to find the maximum $\mathcal{H}$ is likely to introduce additional error. In contrast, the J_{SC} method depends on one point on the curve, does not include any effects from the change in scan direction and is calculated from the monotonically increasing J_{SC} against scan rate. Using J_{SC} measurements to calculate the E_A works significantly better than using $\mathcal{H}$-factor measurements.

4.5 Shifting the timescale or reducing loss?

As can be seen in Figure 4.8 and 4.9, decreasing temperature shifts hysteresis and the drop off in PCE to slower scan rates. However, the decrease in temperature also increases PCE for all scan rates. Most importantly, the PCE, V_{OC}, J_{SC} and FF are all improved for the slowest scan rate (representing steady-state) for a reduction in temperature. Seeing as ion motion is affecting device performance negatively, it is desirable to find a way of mitigating it. Using the model, we can easily study the effect of important device parameters to see if we can identify a practical way of avoiding losses. We can also explore which parameters change the timescale of ion motion. While changing the timescale alone does not improve steady-state performance, the links between ion motion and degradation as discussed in the introduction mean that lengthening the ion timescale may be beneficial for device lifetime.

Defect density

Removing the ion vacancies and other mobile defects would, of course, eliminate hysteresis and any associated loss from ion motion, as this would remove the charges that form the Debye layers. Thermodynamic considerations limit the minimum defect density, however, making total elimination of defects impossible. That said, there is certainly scope for reducing defect density. Reducing vacancy density will lengthen the timescale of hysteresis and any associated loss as, with fewer defects available, ions deeper within the interior of the perovskite are needed to charge the Debye layers sufficiently. Figure 4.13 shows $\mathcal{H}$, J_{SC}, PCE and FF as a function of scan rate for the simulated device as the defect density is reduced from 1.6×10^{19} cm^{-3} by three orders of magnitude down to 1.6×10^{16} cm^{-3}.

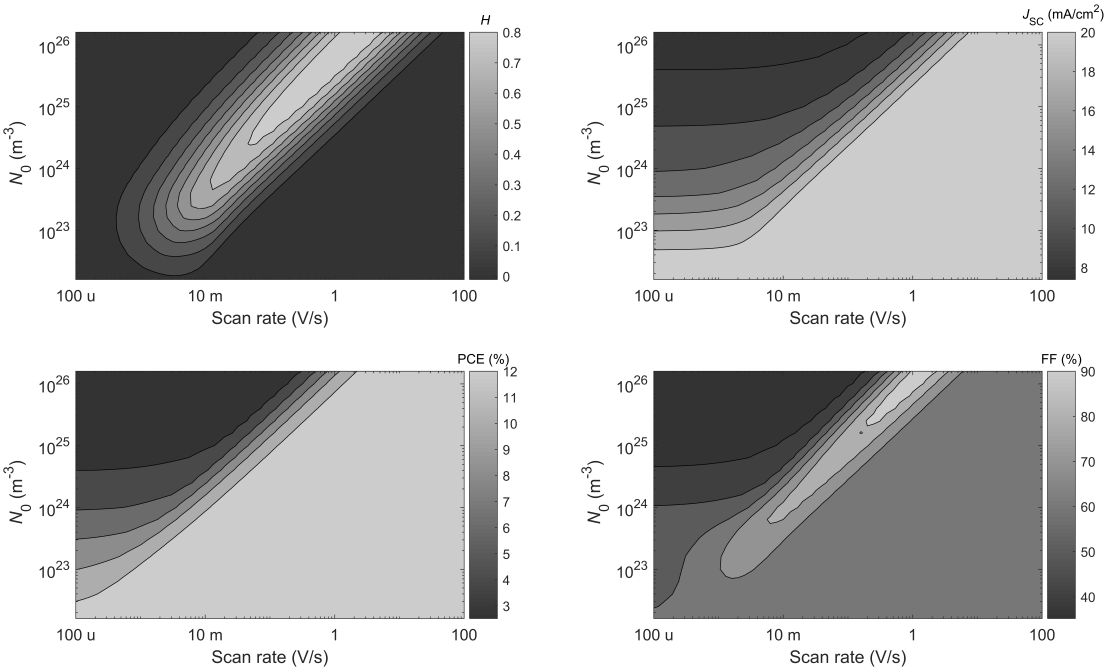

Figure 4.13: $\mathcal{H}$, J_{SC}, PCE and FF as vacancy density N_0 is varied between 1.6×10^{22} and 1.6×10^{26} m^{-3}. The value used previously is 1.6×10^{25} m^{-3}. Reducing N_0 shifts the timescale of ion motion to slower scan rates. If N_0 is reduced enough, the magnitude of both hysteresis and loss is reduced as there are not enough vacancies to fully form the Debye layers. V_{OC} is insensitive to both scan rate and vacancy density, so is not shown.

As the vacancy density is reduced, the hysteresis and loss behaviours are both shifted to slower timescales and both reduced in severity. With fewer defects available, vacancies deeper within the perovskite are required to charge the Debye layers. This requires ions to move further to charge the layers, lengthening the timescale of layer charging. For a given scan rate, reducing the vacancy density reduces loss arising from ion motion.

As the vacancy density is reduced, the equilibrium width of the Debye layers at an applied voltage grow wider. If the density is reduced far enough, the Debye layers take up the entirety of the perovskite layer as all the ionic charge is required to form the layers. If the density is reduced yet further, there is insufficient charge to form layers large enough to fully screen the internal field. The further the density is reduced, the smaller the fraction of the internal field that the ions can screen, causing the drop-off in $\mathcal{H}$ at the lower-left of Figure 4.13.

Reducing defect density in the perovskite has been achieved in practice via the inclusion of a reducing agent during synthesis [82], thermal annealing [83], Lewis base passivation [84], fabrication with an excess of lead halide [85] and the use of additional A-site cations such as caesium [86].

Recombination

If ion motion cannot be entirely eliminated, the loss in performance may at least be mitigated by reducing recombination. While the formation of the Debye layers reduces the electric field within the bulk of the absorber, even inverting it in some

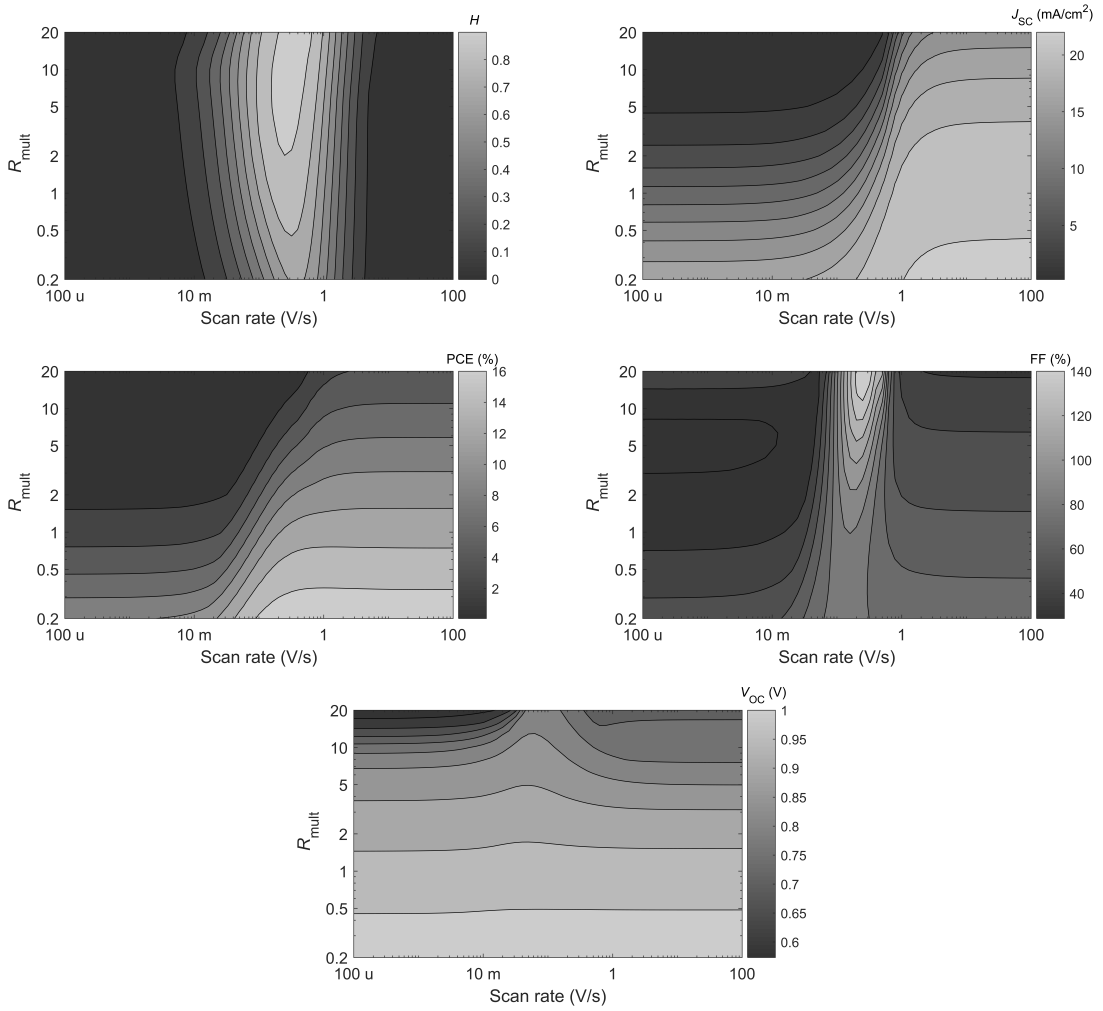

Figure 4.14: $\mathcal{H}$, J_{SC}, PCE, FF and V_{OC} as recombination parameters are varied. The recombination multiplier R_{mult} multiplies the bimolecular recombination coefficient β and the surface recombination velocities v_{nE}, v_{pE}, v_{nH} and v_{pH} and divides the electron and hole SRH pseudolifetimes τ_n and τ_p. The values used previously correspond to $R_{\mathrm{mult}} = 1$. The timescale of hysteresis and loss is largely unchanged with increasing recombination, but, unsurprisingly, the loss becomes more severe.

cases, many perovskite devices still show good performance on the forward scan. This is because such devices have sufficiently long carrier lifetimes and large enough diffusion lengths to produce a large current through diffusion alone. The carrier diffusion length in the mixed-halide perovskite $CH_3NH_3PbI_{3-x}Cl_x$, formed from large crystals, has been found to be of the order of 1 µm [87], considerably greater than the typical perovskite film thickness of hundreds of nm. Ensuring the largest possible grain size is crucial for achieving high diffusion lengths and low recombination [88].

Figure 4.14 shows the result on hysteresis and performance as recombination within the simulated device is reduced. The timescale of ion motion is unaffected by recombination, and so the scan rate dependence of the behaviours is largely unchanged. Loss is reduced for all scan rates, as is to be expected. The greatest improvement is for scan speeds and directions with the weakest bulk field, as it is these situations where recombination is more of an issue. This is why the improve-

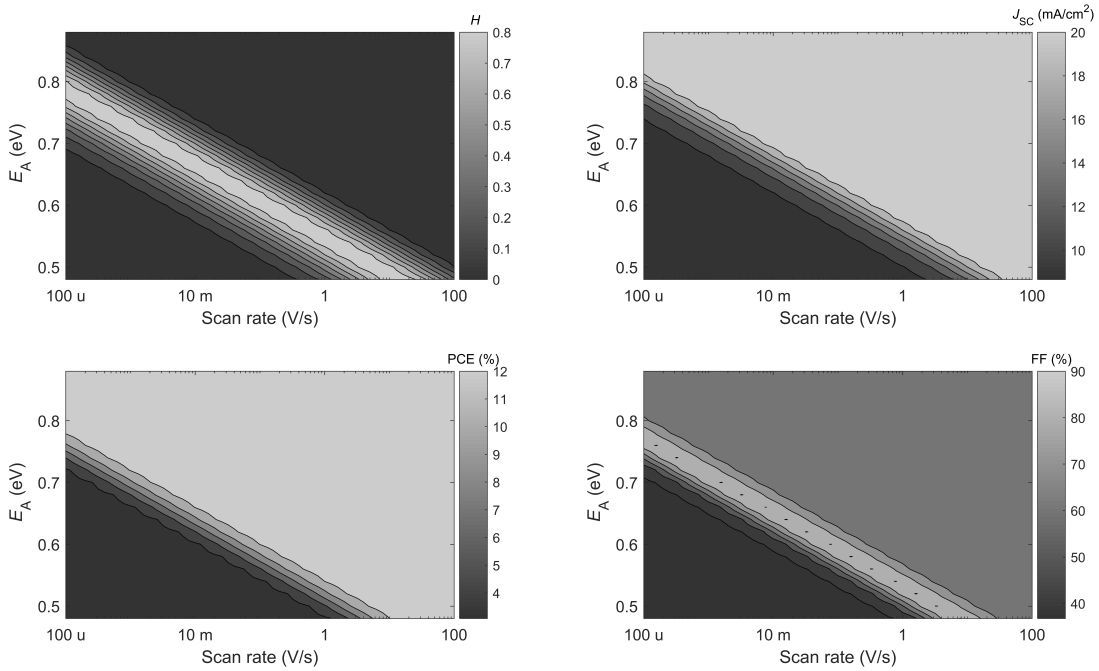

Figure 4.15: $\mathcal{H}$, J_{SC}, PCE and FF as the activation energy for ion motion E_A is varied between 0.48 and 0.88 eV. The value used previously is 0.58 eV. Increasing E_A shifts the timescale of ion motion to slower scan rates, but has no effect on the magnitude of hysteresis or loss. V_{OC} is insensitive to both scan rate and activation energy, so is not shown.

ment in J_{SC} and PCE is greatest for slower scans, as the Debye layers have more time to charge. It is also why $\mathcal{H}$-factor reduces, as the reduction in recombination improves the forward scan more than the reverse scan, leading to less of a difference in the currents between scan directions.

Amusingly, the fill factor for hysteretic scans with high recombination is above 140%. This is due to the formation of the Debye layers causing immense losses at short-circuit current, such that the current at the apparent maximum power point on the down scan is considerably greater than J_{SC}. For the highest recombination rates, open-circuit voltage improves for hysteretic scans. This appears to be due the formation of small Debye layers that help sweep carriers past the perovskite/transport layer interfaces at the expense of the bulk field. For small Debye layers this yields a net improvement, but for fully formed Debye layers, as indicated by the slowest scan, the improvement in charge extraction at the interfaces is more than cancelled by the collapse in charge separation within the bulk (as previously).

Activation energy

If defects were truly static, the Debye layers would never be able to form. As such, it is reasonable to assume that slowing the ions down, by increasing the activation energy for vacancy motion for example, would help improve performance. Figure 4.15 shows the effect of varying the E_A between 0.48 eV and 0.88 eV. Increasing E_A by just 0.1 eV is enough to slow all behaviours by two orders of magnitude for this parameter set. Critically, however, there is no reduction in the magnitude of hysteresis or of loss. The slow scan limit of J_{SC}, which best represents steady-

state, shows no improvement. Slowing the ions is then not a good way of improving PSC performance. It is possible that slowing the ions may improve stability due to reduced lattice strain or mitigating the diffusion of superoxide species, so increasing the E_A should not be entirely discounted.

Transport layer permittivity and doping

More subtly, the choice of transport layer plays a role in determining the timescale of ion motion. As ion motion is an intrinsic property of the perovskite, this is perhaps rather surprising. Some papers have used the observation that hysteresis depends on the transport layers to completely dismiss ion motion as the cause [89]. What these groups choose to ignore is that the ionic Debye layers induce electronic Debye layers within the transport layers. The importance of the electronic layers is especially clear for the devices with moving ions in Figures 4.1 and 4.4, where the electronic Debye layer in the hole transporter constitutes most of the potential drop across the device once the Debye layers have formed. Experimental confirmation of large voltage changes within the transport layers has been provided by Kelvin probe measurements [89].

The critical parameters for the transport layers are the dielectric permittivity and doping density, where lower values for each lead to more of a potential drop in those layers. The lower the doping in the layer, the wider the electronic Debye layers will be. The wider the layers are the greater the distance the potential can change over, yielding a larger potential change even for the same layer charge. The lower the transport layer permittivity, the greater the electric field in that layer due to continuity of electric displacement field normal to a dielectric interface ($\varepsilon_1 E_1 = \varepsilon_2 E_2$). The larger the electric field within the layer, the greater the potential change within that layer. The carrier motion timescale is extremely fast compared to the ionic and J-V scan timescales, so the electronic Debye layers form essentially instantly – the limiting process is ion motion. The larger the porportion of potential change that occurs within the electronic layers, the less change that needs to occur within the ionic layers. This reduces the necessary motion required of the ions, speeding up the bulk field screening process and thereby speeding up the timescale of the hysteresis and loss behaviours.

Figures 4.16, 4.17, 4.18 and 4.19 show the effect on $\mathcal{H}$, J_{SC}, PCE and FF of the ETL permittivity ε_E and doping density d_E and HTL permittivity ε_H and doping density d_H respectively. The values for permittivities have virtually no effect on the performance of devices as measured with a high scan rate because Debye layers don't have a chance to form for these scans. Decreasing the permittivity of a layer causes more of the potential drop across the device to occur within that layer, and thus less within the perovskite, but that does not make a significant difference here. The doping of the ETL also has no effect on the high scan rate performance, while the doping of the HTL does. This is because the low permittivity of the HTL, 3 ε_0, causes the layer to dominate over the contribution of the ETL with permittivity 40 ε_0, as discussed earlier and seen in Figures 4.1 and 4.4.

Like before, J_{SC} and PCE fall as scan rate is reduced irrespective of transport layer properties as the formation of the Debye layers reduce performance. Oddly, steady-state PCE improves as ETL permittivity and doping are decreased, but improves as HTL permittivity and doping are increased. This difference appears to be due to surface recombination being more severe with the ETL than HTL. As

ε_E and d_E decrease and ε_H and d_H increase, more of the potential drop occurs at the interface of the perovskite with the ETL. The greater potential drop at the ETL/perovskite interface helps sweep electrons efficiently into the ETL and hinders holes from approaching the interface.

As theorised, decreasing the permittivities and doping of both layers acts to shift the timescale of hysteresis to faster scan rates. So-called hysteresis-free devices tend to employ organic semiconductors for both transport layers, which have low permittivities and dopings compared to inorganic materials. It has been found that cooling such a device, which we know shifts hysteresis to longer timescales, can lead to hysteresis reappearing [80]. It is then natural to ask if hysteresis-free devices actual have hysteresis at timescales faster than those routinely measured in the characterisation of PSCs.

We can test this hypothesis using the model by varying ε_E, d_E, ε_H and d_H simultaneously over a wide range to gain an idea of how much of a difference this is likely to make. Figure 4.20 shows the effect of varying the permittivities from ε_0 to 100 ε_0 and doping densities from 10^{20} m^{-3} to 10^{26} m^{-3} at the same time. Reducing these four parameters does indeed shift hysteresis, as well as the sigmoidal transition from low J_{SC} and PCE to high, to higher scan rates. A typical J-V scan at about 100 mV/s would exhibit a large amount of hysteresis for a device with high values for the permittivities and doping densities, but almost none for a device with low values for these parameters. The model predicts that switching from an inorganic transport layer to an organic one will shift hysteresis to higher scan rates, and reducing the temperature will then shift the hysteresis back to the 100 mV/s regime. This offers an explanation for why organic transport layers yield apparently hysteresis-free cells. However, this shift to higher scan rates actually reduces performance. Ironically, this method to eliminate observable hysteresis does so at the expense of PCE.

Summary

Figure 4.21 gives a summary of the effect of vacancy density, severity of recombination, vacnacy motion activation energy and transport layer properties on hysteresis factor $\mathcal{H}$ and apparent power conversion efficiency PCE. Reducing the defect density N_0 reduces the magnitude of hysteresis and associated loss, and shifts the hysteresis behaviour to longer timescales. Reducing recombination does not change the timescale of hysteresis behaviour, but does reduce the magnitude of hysteresis and improve PCE. Increasing the activation energy, thus slowing the ions, shifts the behaviour to longer timescales but has no effect on the magnitude of hysteresis or loss. Increasing the doping densities and permittivities of the transport layers shifts the behaviours to longer timescales. Interestingly, the magnitue of hysteresis increases then decreases, although PCE, even at steady-state, is always improved.

Efforts to eliminate ion migration-induced efficiency losses should then focus on reducing defect density and reducing recombination. One method that may achieve both these goals is minimisation of compressive lattice strain. Recent results [90] suggest that equilibrium halide vacancy concentration correlates with strain and that strained regions show increased non-radiative recombination. Alleviating strain should enhance the beneficial effects of decreased vacancy density and passivation of non-radiative recombination to both slow the onset of loss from ion motion and also reduce its extent as in Figure 4.21. Concerted surface passivation strategies can further reduce surface vacancies and decrease non-radiative recombination. Ex-

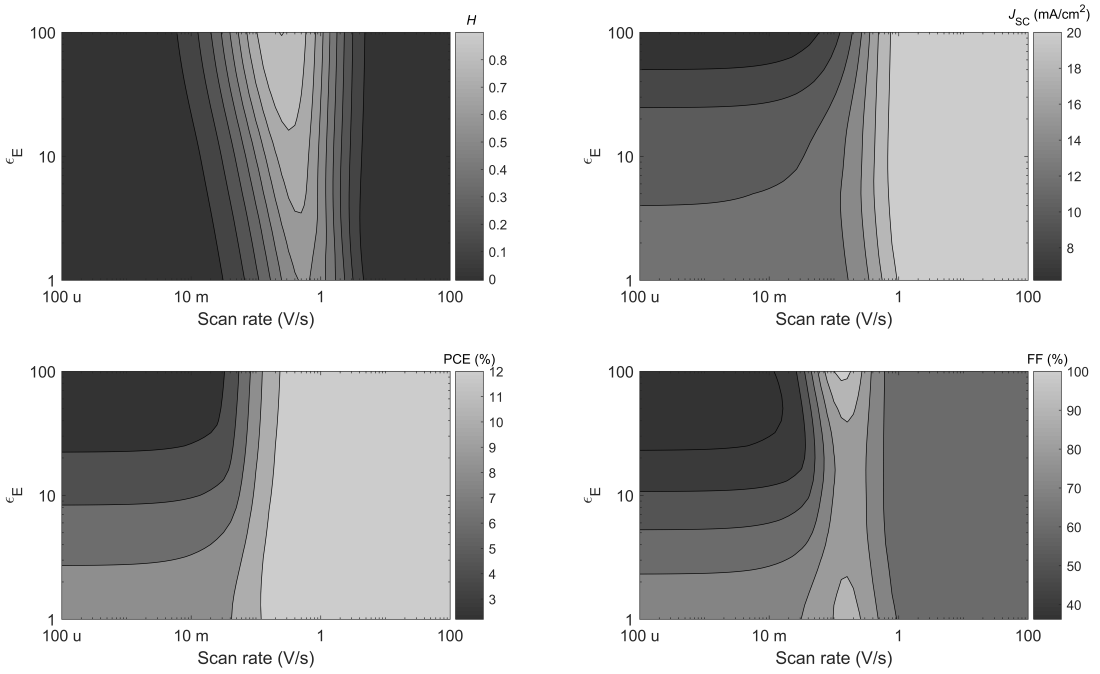

Figure 4.16: $\mathcal{H}$, J_{SC}, PCE and FF as the ETL permittivity ε_E is varied between ε_0 and 100 ε_0. The value used previously was 40 ε_0. V_{OC} is insensitive to both scan rate and ε_E, so is not shown.

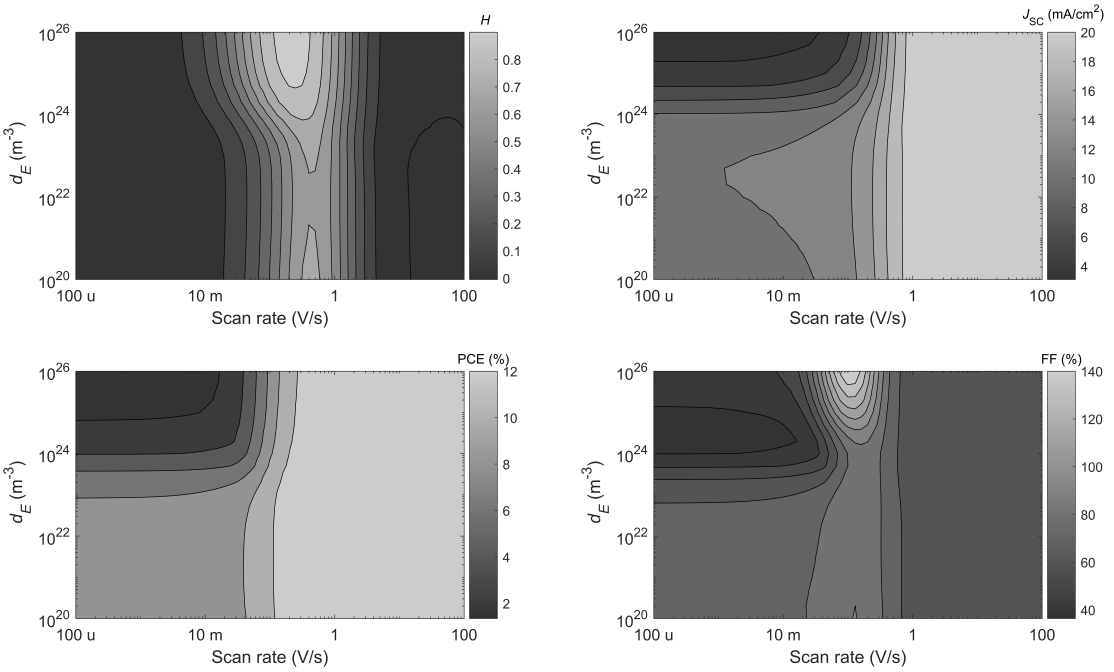

Figure 4.17: $\mathcal{H}$, J_{SC}, PCE and FF as the ETL doping density d_E is varied between 10^{20} m^{-3} and 10^{26} m^{-3}. The value used previously was 1.7×10^{24} m^{-3}. V_{OC} is insensitive to both scan rate and d_E, so is not shown.

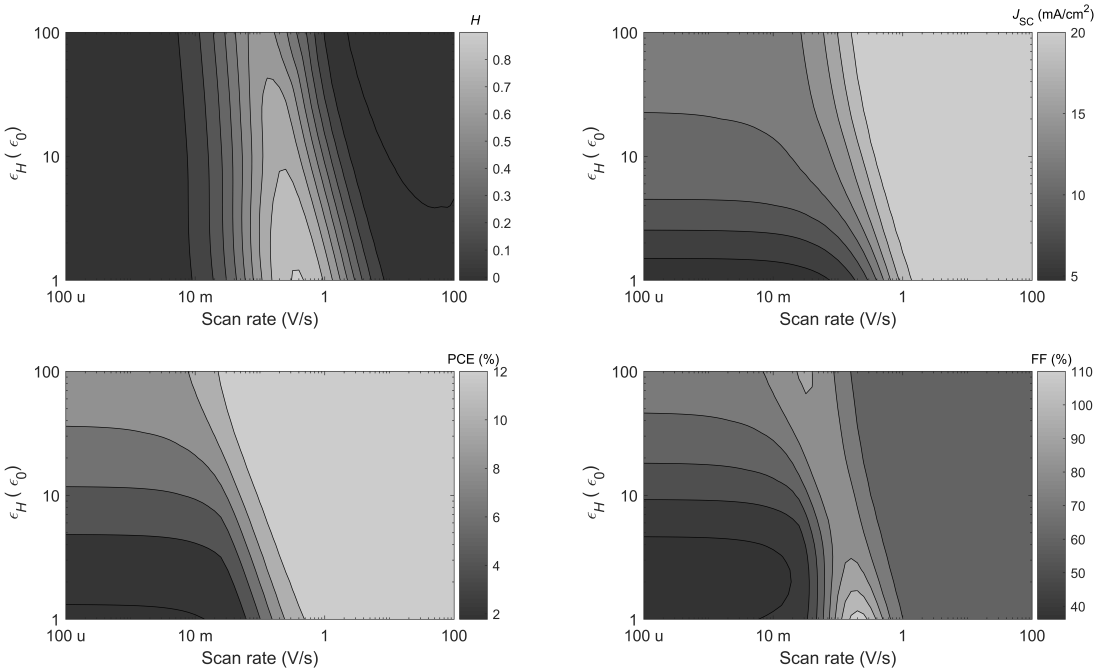

Figure 4.18: $\mathcal{H}$, J_{SC}, PCE and FF as the HTL permittivity ε_H is varied between ε_0 and 100 ε_0. The value used previously was 3 ε_0. V_{OC} is insensitive to both scan rate and ε_H, so is not shown.

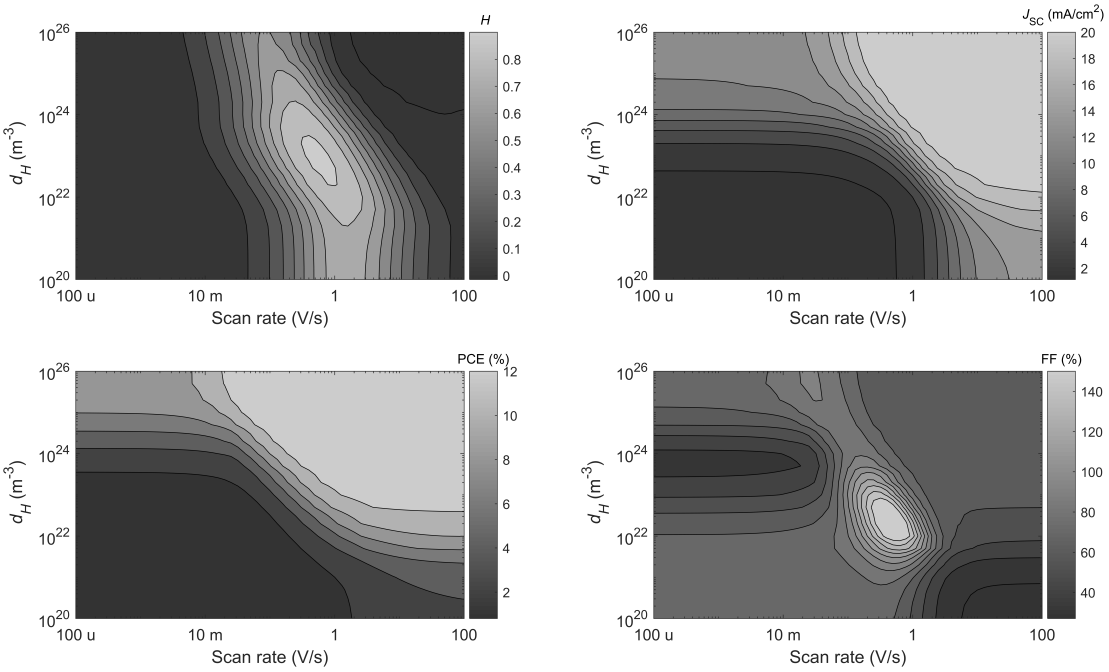

Figure 4.19: $\mathcal{H}$, J_{SC}, PCE and FF as the HTL doping density d_H is varied between 10^{20} m^{-3} and 10^{26} m^{-3}. The value used previously was 8×10^{23} m^{-3}. V_{OC} is insensitive to both scan rate and d_H, so is not shown.

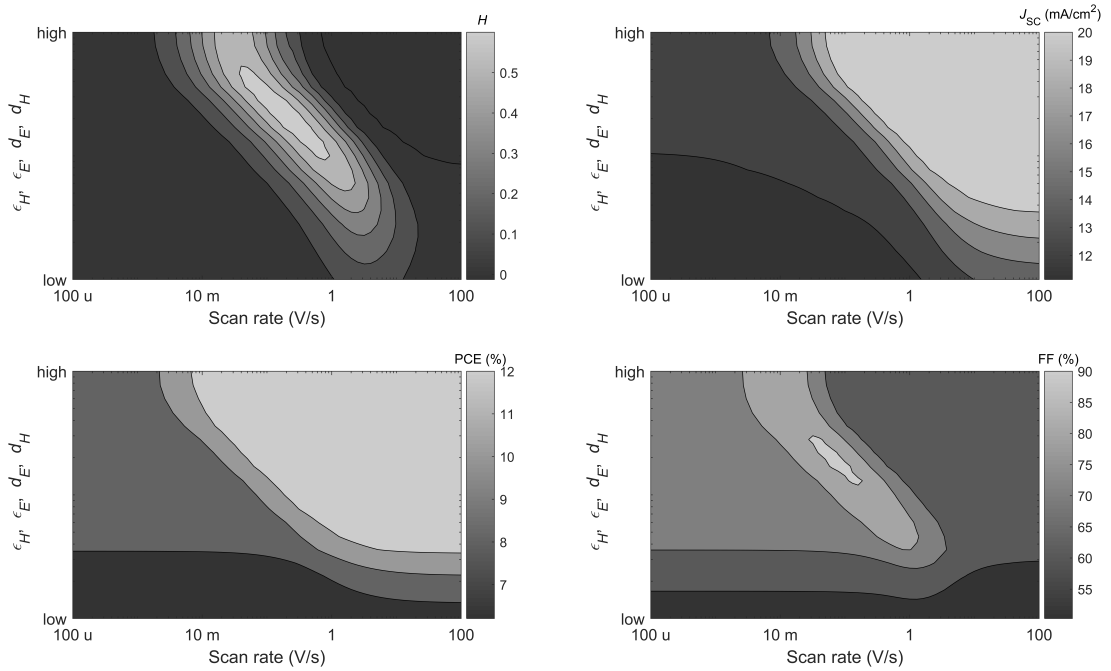

Figure 4.20: $\mathcal{H}$, J_{SC}, PCE and FF against scan rate as the transport layer permittivities $\varepsilon_E = \varepsilon_H$ are varied together between ε_0 and 100 ε_0 and simultaneously the transport layer doping densities $d_E = d_H$ are varied together between 10^{20} m^{-3} and 10^{26} m^{-3}. The values used previously are given in Table 3.2. V_{OC} is insensitive to all these parameters as before, so is not shown.

ploration of a range of A site cations, as mixed cation PSCs exhibit lower defect density and enhanced performance and stability [45, 86, 91]. These strategies could lead to significant improvements in stabilised device PCE and marked reductions in ion motion and photocurrent hysteresis.

Increasing activation energy is not suitable as a method to eliminating hysteresis or efficiency losses from ion motion, as all slowing the ions does is shift the hysteresis to longer timescales. Reducing ion motion may be beneficial in other ways, such as reducing degradation related to lattice strain from ion hopping, although this is still speculative. The model predicts that transport layers with higher permittivities and doping densities yield better performance, and so suggests the use of inorganic transport layers over organic ones. Note there is some evidence [92] that perovskite layers form better quality films when deposited on organic films, leading to reduced recombination and vacancy density – depending on the difference in quality, this may affect the conclusion.

4.6 Ion density as a function of temperature

When we discussed the dependence of device behaviour on temperature, we noted that the ionic diffusivity D_P takes the form

$$D_P = D_P^{\infty} \exp\left(-\frac{E_{\mathrm{A}}}{k_{\mathrm{B}}T}\right). \tag{4.12}$$

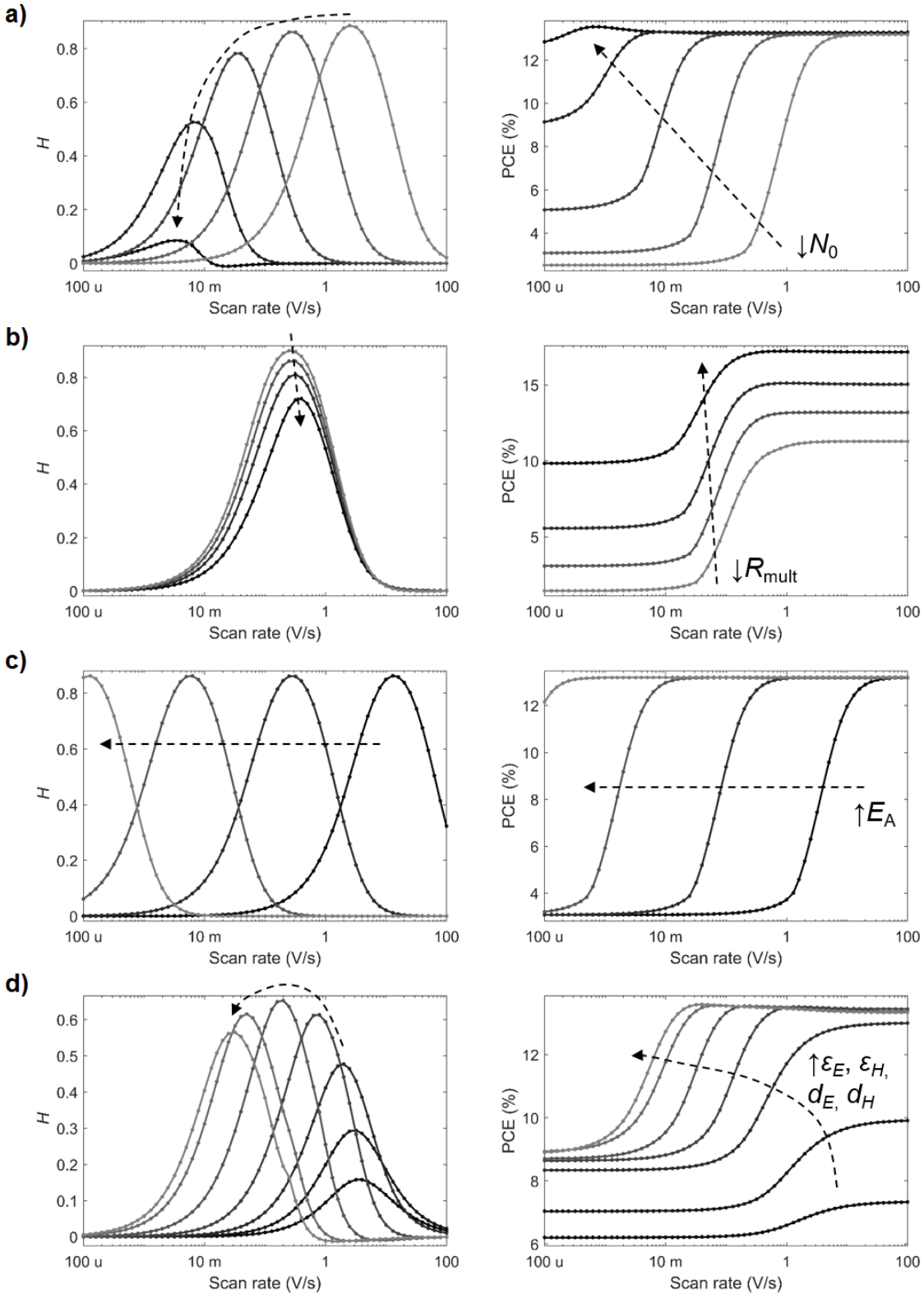

Figure 4.21: The effect on $\mathcal{H}$-factor and PCE from (a) decreasing the vacancy density N_0, (b) reducing recombination R_{mult}, (c) increasing the activation energy for halide vacancy motion E_{A} and (d) increasing transport layer permittivities and doping densities ε_E, d_E, ε_H and d_H.

By assuming the system response R is proportional to D_P, and that D_P is the only parameter with Arrhenius form, a plot of $\ln R$ against $1/k_\mathrm{B}T$ yields the activation energy E_A. By choosing an easily measurable R, this provides us a method of inferring the activation energy from experimental data. However, what if D_P isn't the only parameter with Arrhenius form?

Until now, we have taken the iodide vacancy density N_0 to be a fixed value of 1.6×10^{25} m^{-3} at all temperatures [51]. Assuming a cubic lattice with parameter $a = 0.63$ nm [51], the unit cell density is $1/a^3 = 4 \times 10^{27}$ m^{-3}. For 0.4% of Schottky defects at room temperature [52], we find our N_0 from before. The fraction of sites with a vacancy may itself be calculated from[†]

$$\exp\left(-\frac{\Delta H_\mathrm{S}}{k_\mathrm{B}T}\right), \tag{4.13}$$

where ΔH_S is the reaction enthalpy (essentially an activation energy) for defect formation. ΔH_S for a Schottky defect has been calculated to be 0.14 eV [52]. We can then derive an expression for the defect density as a function of temperature as

$$N_0 = N_0^\infty \exp\left(-\frac{\Delta H_\mathrm{S}}{k_\mathrm{B}T}\right) \tag{4.14}$$

where N_0^∞ is the high-temperature limit. In order for N_0 at $T = 300$ K to be 1.6×10^{25} m^{-3} as before, N_0^∞ must be 3.6×10^{27} m^{-3}. The 10% discrepancy between this number and the unit cell density appears to be due to a rounding error in literature of $\exp(-0.14/0.0259) = 0.449\% \approx 0.4\%$, a testament to finding the final answer algebraically before plugging the numbers in.

If N_0 varies exponentially with T, then we need to rethink the method of extracting the activation energy – we know from Figure 4.13 that varying N_0 shifts the timescale of the ion motion behaviour as measured by $\mathcal{H}$-factor, J_SC, PCE, V_OC and FF. We previously assumed that the system response R was simply directly proportional to the ionic diffusivity D_P. As the system response depends on how quickly the ionic Debye layers charge, it is more appropriate to consider the current of ions into the layers. From Ohm's law, the ionic current is

$$j_P = \sigma_P E \tag{4.15}$$

where σ_P is the ionic conductivity and E the electric field. The relevant E for this problem is the unscreened bulk field within the perovskite layer. The ionic conductivity for (monopositive) halide ions can be calculated from

$$\sigma_P = N_0 \mu_P q \tag{4.16}$$

where N_0 is the number density, μ_P the mobility and q the elementary charge. Converting mobility to diffusivity using the electrical mobility equation

$$D_P = \frac{k_\mathrm{B}T}{q}\mu_P, \tag{4.17}$$

we find

$$\sigma_P = \frac{q^2}{k_\mathrm{B}T} N_0 D_P. \tag{4.18}$$

[†] ΔH_S should be divided by 2 in each equation in this section in which it appears. Please see the note at the end of this section.

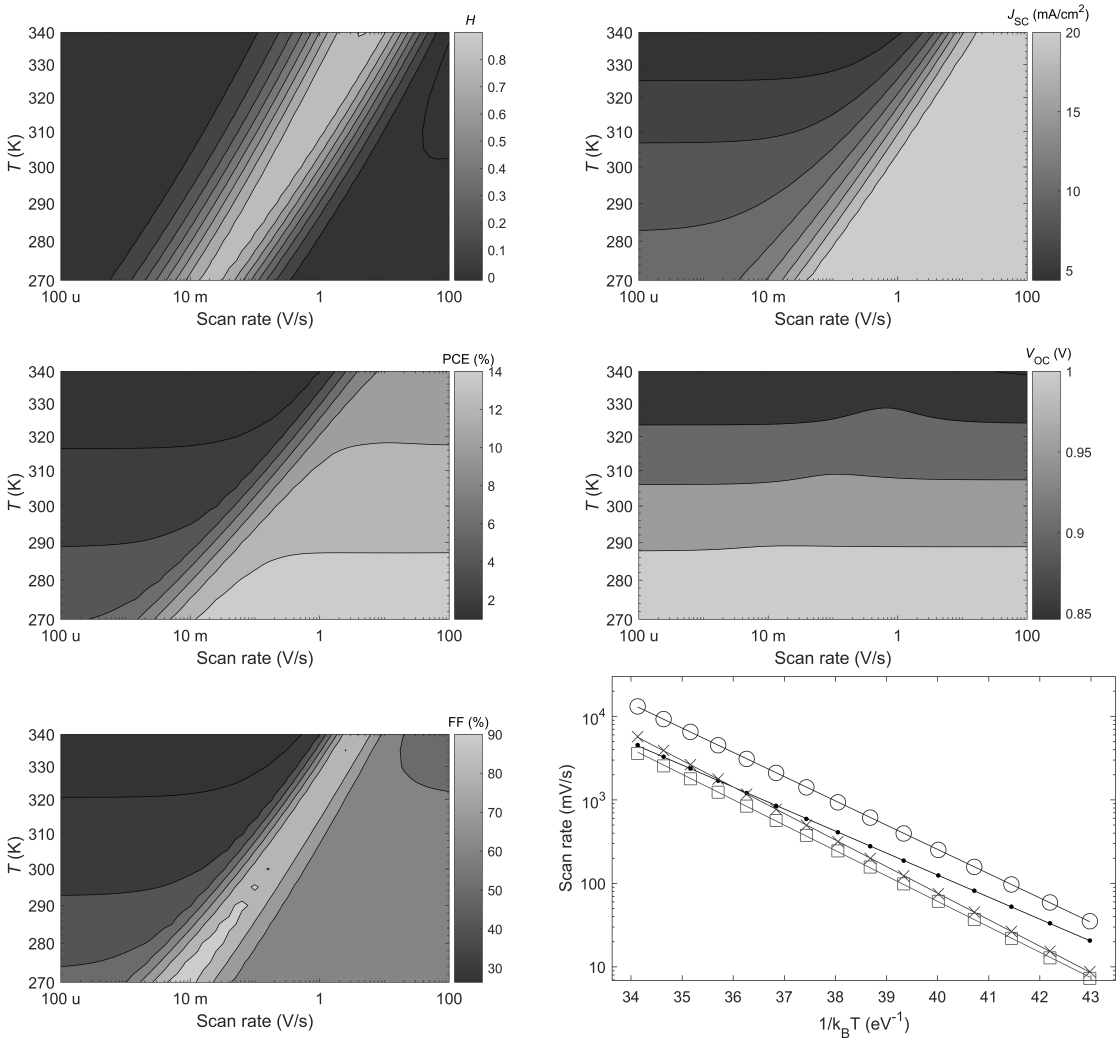

Figure 4.22: Variation in $\mathcal{H}$-factor, J_{SC}, PCE, V_{OC} and FF with scan rate and temperature T, where both the ionic diffusivity D_P and ionic density N_0 have an Arrhenius dependence on T. Arrhenius plot of the scan rates yielding maximum $\mathcal{H}$ (dots), 90% of maximum J_{SC} (circles), 90% of maximum PCE (crosses) and maximum FF (squares). Values for activation energy plus reaction enthalpy inferred from gradients are tabulated in Table 4.3.

Measure	Inferred $E_{\mathrm{A}} + \Delta H_{\mathrm{S}}$ (eV)	Error (%)	Change, $\approx \Delta H_{\mathrm{S}}$ (eV)
$\mathcal{H}$	0.6072	-16	0.0762
J_{SC}	0.6691	-7.1	0.0810
PCE	0.7319	1.7	0.0824
FF	0.7010	2.6	0.0755

Table 4.3: Values for $E_{\mathrm{A}} + \Delta H_{\mathrm{S}}$ inferred from the shift in hysteresis factor $\mathcal{H}$, short-circuit current J_{SC}, power conversion efficiency PCE and fill factor FF. The error is given between each inferred $E_{\mathrm{A}} + \Delta H_{\mathrm{S}}$ and the expected exponential dependence, 0.72 eV. Also listed are the differences between the activation energies in Table 4.1, inferred from when N_0 is independent of T, which gives an indication of the effect of ΔH_{S} alone. The true $\Delta H_{\mathrm{S}} = 0.14$ eV is underestimated.

Then including the Arrhenius forms of D_P from 4.12 and of N_0 from 4.14 we obtain

$$\sigma_P = \frac{q^2 N_0^\infty D_P^\infty}{k_\mathrm{B} T} \exp\left(-\frac{E_\mathrm{A} + \Delta H_\mathrm{S}}{k_\mathrm{B} T}\right). \tag{4.19}$$

Now saying $R \propto \sigma_P$ rather than directly to D_P, we discover an additional dependence of R on $1/T$ which may be contributing to the error in the inferred values of E_A. Assuming that the exponential dependence dominates, we find

$$R \propto \exp\left(-\frac{E_\mathrm{A} + \Delta H_\mathrm{S}}{k_\mathrm{B} T}\right) \tag{4.20}$$

which differs from (4.10) with the addition of the reaction enthalpy ΔH_S. On an Arrhenius plot, we would then expect a gradient of $-(E_\mathrm{A} + \Delta H_\mathrm{S})$.

Figure 4.22 shows contour plots of $\mathcal{H}$, J_SC, PCE, V_OC and FF as a function of scan rate and temperature T where the vacancy density N_0 varies exponentially as in (4.14) with a reaction enthalpy ΔH_S of 0.14 eV and high T prefactor N_0^∞ of 3.6×10^{27} m^{-3}. As before, in Figure 4.9, the ion diffusivity varies exponentially with an activation energy E_A of 0.58 eV and high T prefactor D_P^∞ of 3×10^{-8} m^2/s. The inclusion of a temperature dependence of N_0 does indeed increase the inferred activation energy, although not by a much as expected. We would expect the inferred energy to increase by $\Delta H_\mathrm{S} = 0.14$ eV compared to the previous energies, although each measure only increases by about 0.08 eV. Arrhenius plots work best when $E_\mathrm{A} \gg k_\mathrm{B} T$, as a small change in temperature leads to a large change in dependent variable. The ΔH_S here is only about 5 times larger than $k_\mathrm{B} T$ at 300 K, and so N_0 is not especially sensitive to temperature. The underestimation of about 0.06 eV is likely then to be error. When ΔH_S is set artificially high to 0.6 eV, and the prefactor N_0^∞ to an unphysically high 1.84×10^{35} m^{-3} to preserve an N_0 of 1.6×10^{25} m^{-3} at 300 K, the inferred energies for all four methods increase by about 0.6 eV as expected with an error of a few times $k_\mathrm{B} T$.

That ΔH_S changes the measured activation energy at all should be a consideration to using the shift in $\mathcal{H}$-factor, J_SC etc. to finding E_A experimentally. However, this is only a problem if the vacancy density is able to vary freely according to (4.14) after fabrication. As part of an encapsulated PV device, it may be that N_0 is unable to significantly change with temperature – after all, where would the removed ions go? Removed ions might be positioned along grain boundaries or perhaps as interstitial Frenkel defects, although the tight packing of lead halide perovskites makes Frenkel disorder unfavourable [51]. As ΔH_S is relatively small compared to E_A, the error from the contribution of the former to measuring the latter, especially if the effect is suppressed by encapsulation, is also small.

Note

In my viva it was pointed out that there should actually be a factor of 2 in the denominator of the exponential terms in all equations in this section containing a ΔH_S term. In equations containing both E_A and ΔH_S terms, only the ΔH_S should be halved. The reason for this is that vacancy formation produces a *pair* of defects. With regard to the model, the calculation of the vacancy density as a function of temperature $N_0(T)$ (4.14) is implemented exactly as written above without the factor of 2. The effect of neglecting this factor is the same as modelling a ΔH_S of

twice what it actually is, i.e. of 0.28 eV. The main practical finding of this section, that the ion density N_0 being a function of temperature will not significantly altar deduction of E_A, is unchanged. In fact, the effect is overestimated due to this error and $N_0(T)$ has even less of an impact than found in this work. The finding that ΔH_S will shift the hysteresis and other scan rate dependent device behaviours in the same manner as E_A is unchanged.

4.7 Preconditioning and inverse hysteresis

In the preceeding work, all J-V curves have swept from the built-in voltage V_bi down to 0 V and back up to V_bi. This is because at V_bi there is no bulk field, and so the Debye layers have no charge. In practice, however, V_bi is not known beforehand. Indeed, high performance devices may have an open-circuit voltage $V_\mathrm{OC} > V_\mathrm{bi}$, and so starting the measurement above V_bi is necessary to measure the full power generating quadrant of the J-V curve. Generally, the voltage is swept from some 'nice round number' such as 1.2 or 1.6 V, chosen depending on the device to be sufficiently above V_OC to measure the full curve. Normally, the device is held at the start voltage for some length of time before the J-V sweep, to allow the measurement to settle. This process is known as preconditioning, where we shall refer to the start voltage as the preconditioning voltage V_pre.

Preconditioning gained notoriety in the early days of perovskite research, when it was found that preconditioning at a little above V_OC could improve measured performance on the down scan [2]. Groups could report inflated performance by preconditioning at a high voltage and then reporting only the down sweep of the J-V scan. From the model, we know that this is because holding the device at around V_bi discharges the Debye layers. Note that a cell in the dark with no applied voltage, for example in a drawer with nothing attached to the electrodes, has fully charged Debye layers. In the dark there is a potential difference between the electrodes that charges the Debye layers, but no difference in Fermi levels that could be used to do work. A device that is scanned from 0 V up and back down starts with the Debye layers fully charged, giving worse performance. A device that is taken from $V_\mathrm{ap} = 0$ to $V_\mathrm{ap} = V_\mathrm{bi}$ quickly and then immediately scanned down and up will still exhibit poor performance, as the layers do not have time to discharge. Preconditioning for some length of time, usually minutes, is required.

Of interest is what happens when V_pre is a few hundred meV greater than V_bi, as is usually the case in J-V measurements. Figure 4.23 shows $\mathcal{H}$, J_SC, PCE, FF and V_OC as a function of scan rate as the preconditioning voltage is increased from starting at $V_\mathrm{bi} = 1.05$ V. Perhaps the most prominent feature is the region of negative $\mathcal{H}$-factor for relatively fast scan rates (but not extremely fast scans) for far forward bias. These J-V curves, said to exhibit *inverse hysteresis*, have an up scan that is better than the down scan. Inverse hysteresis is a phenomenon of the equilibrium charging of the Debye layers past V_bi. Figure 4.24 shows the band energies and vacancy density profile for a scan with inverse hysteresis, with $V_\mathrm{pre} = 1.45$ V and a scan rate of 1 V/s. The band energies, vacancy density profile and bulk electric field throughout the full J-V curve is shown in supplementary video 4. An explanation of the meaning of the panels in this video is given in Section 4.2.

Initially, in panel (a), the Debye layers are charged to ensure zero bulk electric field (flat bands in the bulk). This differs from $V_\mathrm{pre} = V_\mathrm{bi}$, where there is no

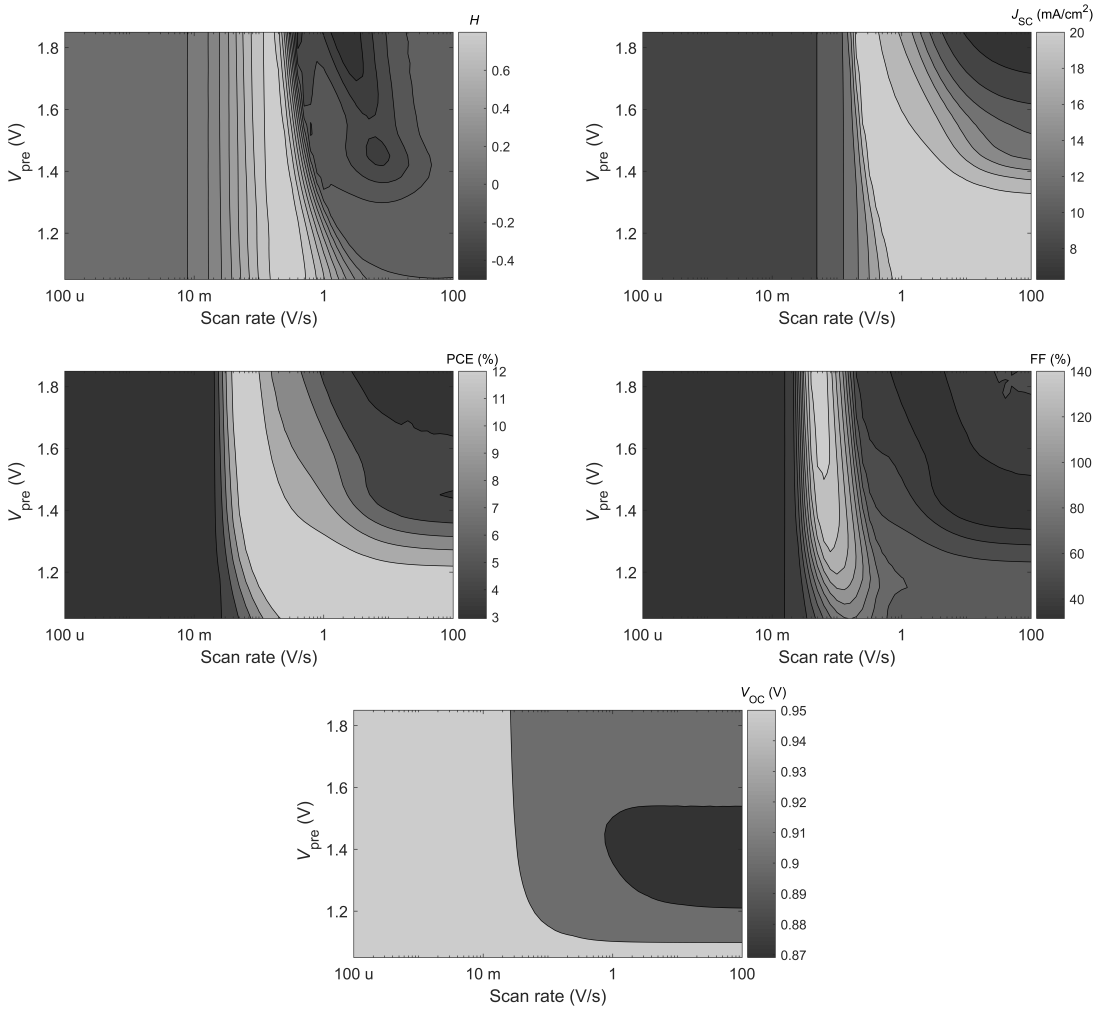

Figure 4.23: $\mathcal{H}$, J_{SC}, PCE and FF as the preconditioning voltage V_{pre} is increased from its previous value of $V_{\mathrm{bi}} = 1.05$ V up to 1.85 V. Most notably, a region of negative $\mathcal{H}$, known as inverse hysteresis, appears for $V_{\mathrm{pre}} > V_{\mathrm{bi}}$ for fast scans.

bulk field to begin with so the Debye layers are not charged. When $V_{\mathrm{ap}} > V_{\mathrm{bi}}$ the bulk field drives carriers away from their respective transport layers, and so the Debye layers are charged with opposite polarity to when $V_{\mathrm{ap}} < V_{\mathrm{bi}}$. As before, very slow scans show no hysteresis because the Debye layers charge/discharge sufficiently rapidly to keep up with the scans; very fast scans show none because the layers charge/discharge sufficiently slowly to be negligible on the timescale of the scan. For certain hysteretic scans with relatively fast scan rates, such as the scan in Figure 4.24 and supplementary video 4, the scan is fast enough such that the negatively charged Debye layers take the majority or entirety of the scan to discharge. For hysteretic scans with slower scan rates, such as those with rates less than a few hundred mV/s in Figure 4.24, inverse hysteresis is not observed because the negative Debye layers fully discharge in the early stages of the down scan.

During the scan, the negative Debye layers *increase* the electric field within the bulk at the expense of introducing potential barriers near the interfaces with the transport layers. This is the case in Figure 4.24 (b) and (c), as can be seen by the slight minima in band energies next to the ETL and slight maxima next to the HTL. While the increased bulk field boosts charge separation in the bulk, this is

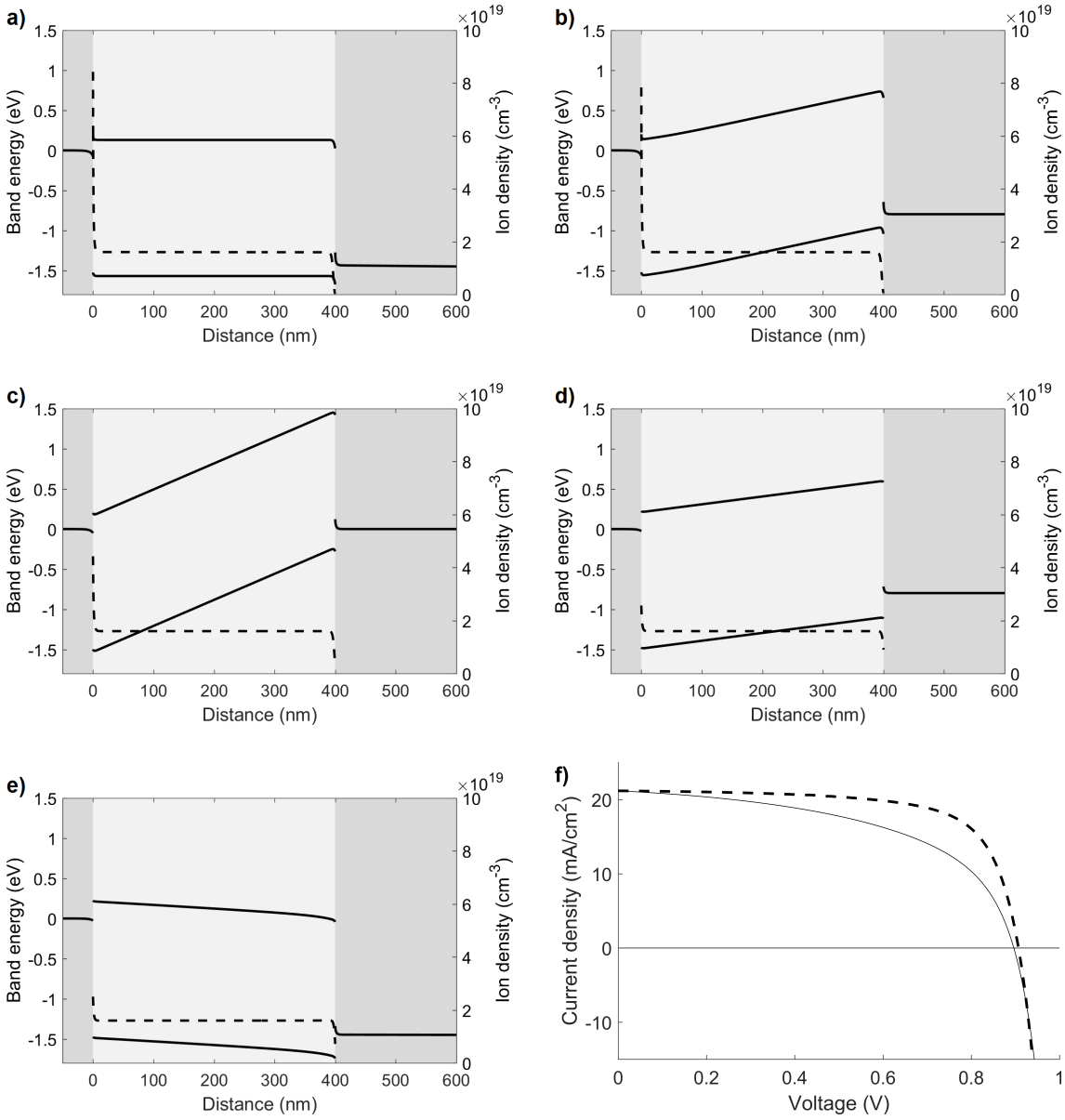

Figure 4.24: (a)-(e) Band energies (solid lines, left axes) and halide vacancy density (dashed lines, right axes) for a PSC at five points throughout a J-V scan starting from 1.45 V down to 0 V and back up to 1.45 V at 1 V/s. Shown are applied voltages of (a) 1.45 V at the start of the down scan, (b) 0.8 V on the down scan, (c) 0 V, (d) 0.8 V on the up scan and (e) 1.45 V at the end of the up scan. (f) The full J-V curve, with down scan denoted by the thin solid line and up scan by the thick dashed line. This curve is notable for exhibiting inverse hysteresis, whereby the up scan is better than the down scan.

more than cancelled out by the energy extrema near the interfaces that block the carriers from transferring to the transport layers. Over time, the negative Debye layers discharge, improving photocurrent. By 0.8 V on the up scan, plotted in panel (d), the Debye layers are considerably less charged than for 0.8 V on the down scan in panel (b). As a result, the current on the up scan is greater than that of the down scan, yielding inverse hysteresis. The full J-V scan is shown in panel (f).

The other clear feature of Figure 4.24 is a decrease in (b) J_{SC}, (c) PCE and (d) FF for fast scans as V_{pre} is increased, leading to L-shaped regions of high performance on these plots. This decrease in performance is another consequence of negative Debye layers. For these faster scan rates, the Debye layers are unable to discharge significantly during the down scan. Larger preconditioning voltages cause larger energy barriers near the interfaces which take longer to discharge, yielding poorer performance. If the scan rate is slow enough then V_{pre} has no effect, as evidenced by the vertical contours for the slowest scan rates. Slow scan rates should be used anyway, as previously discussed, in order to measure the steady-state performance of devices.

4.8 Conclusion

The drift-diffusion model has been applied to explore the behaviour of a typical planar lead halide perovskite solar cell. First and foremost, vacancy-mediated halide ion motion is found to offer a unified theory for a wide range of anomalous behaviours, including current-voltage hysteresis. Ions within the perovskite active layer pack into tight Debye layers next to the internal interfaces with the transport layers. The ionic layers induce counter layers of carriers within the transport layers themselves. The Debye layers act to screen the electric field within the active layer, hindering charge separation and extraction. This leads to increased bulk recombination, and lower performance.

J-V hysteresis and associated effects are fully explained by the dynamics of the Debye layers charging and discharging over the course of the scan. Holding a device at high voltage and scanning down yields better performance than starting at short-circuit, as the Debye layers start discharged. The extent to which hysteresis present depends on the alignment of the timescale of the J-V sweep with the timescale of the Debye layers charging and discharging. Very fast scans yield no hysteresis and good performance, representative of the device if the ions were immobile. Very slow scan rates also exhibit no hysteresis but poor performance, representative of steady-state operation. Scans where the timescales are comparable, normally hundreds of mV/s, show hysteresis. To tell if hysteresis is present, a device should be measured at a range of scan rates.

The timescales of ion motion, and thus Debye layer charging/discharging, may be modified via changing temperature, vacancy density, activation energy and transport layer properties. Increasing temperature speeds up the ions, shifting hysteresis to higher scan rates. Due to the Arrhenius dependence of ion diffusivity on temperature, the activation energy may be extracted experimentally from J-V curves by examining how hysteresis, short-circuit current, power conversion efficiency and fill factor shift in scan rate as the temperature is varied. Activation energies are found experimentally for four perovskite solar cells, in good agreement with density functional theory calculations.

Reducing vacancy density shifts hysteresis to longer timescales and reduces loss. Reducing recombination reduces loss, but does not affect the hysteresis timescale. Increasing activation energy lengthens the hysteresis timescale, but does not reduce loss. Increasing the permittivities and doping densities of the transport layers lengthens the timescale of hysteresis and reduces loss, although can increase the amount of hysteresis for certain values.

The prediction of hysteresis on transport layer properties explains a key criticism of ion motion theory: if ion motion is an intrinsic property of perovskite, transport layers would naïvely be expected not to make a difference. The drift-diffusion model shows, due to explicit modelling of the transport layers and fully-coupled particle dynamics, that electronic charge in the transport layers also contribute to field screening. Hysteresis-free devices may be explained by the dependence on transport layer properties, as changing an inorganic transport layer to an organic one may shift the hysteresis to fater scan rates than routinely measured.

The effect of setting ion vacancy density as a function of temperature is explored, finding that the gradient of the Arrhenius plot then gives sum of the activation energy for ion motion as before plus the reaction enthalpy for vacancy formation. If the vacancy density is able to vary freely with temperature then measurements of the activation energy may be overestimated. As the reaction enthalpy is predicted to be small, of the order 100 meV, the error from neglecting this term is also likely to be small. Finally it is demonstrated that preconditioning at a high voltage, hundreds of mV past the built-in voltage, can cause inverse hysteresis. In such a case, the up scan is better than the down scan due to the formation of Debye layers at the start of the scan that act to block charge extraction at the perovskite/transport layer interfaces.

Chapter 5

Kinetic Monte Carlo Modelling of Energy Transport in Organic Solar Cells

Organic solar cells (OSCs) have shown considerable potential as an alternative PV technology, especially for niche applications [93]. Advantages of OSCs largely coincide with the advantages of organic electronics generally. Organic films are very flexible, in turn opening up the possibility to manufacture using roll-to-roll (R2R) processing techniques and for use in wearable devices. The feedstock has the potential to be low cost, if production were to commence on an industrial scale, and critical device properties (specifically energy levels) can be tuned through both material choice and doping. The low initial capital cost to deploy a system is useful for generating small amounts of power in isolated areas. The main disadvantages of OSCs are low power conversion efficiencies, that struggle to compete with those of traditional inorganic devices [94] and issues relating to long-term stability affected OSCs from their inception [95] and continue to to this day [96]. It has been predicted that organic systems are capable of generating power competitively if commercial OPV modules can achieve an efficiency of 7% (already found in laboratory produced devices) and a lifetime of 5 years [97].

This chapter examines energy dynamics within OSCs. Energy transfer between different materials is known to occur within organic devices, but its relative importance in practical devices is unclear. The scale of energy transport in a standard OSC architecture, with both two and three materials, is studied. How energy transport may be exploited to improve device performance is discussed.

5.1 Introduction

Excitons

Absorption of a photon in an OSC works much the same as in an inorganic device. An absorbed photon promotes an electron from the highest occupied molecular orbital (HOMO) to the lowest unoccupied molecular orbital (LUMO). These are analogous to the valence and conduction bands respectively. The electron and hole are separated and driven to opposite sides of the device. An additional challenge arises in OPV compared to inorganic photovoltaic devices – that of separating a produced

electron-hole pair when it is first generated. In inorganic materials absorption of photons directly produces free charge carriers, but in OSCs the pairs remain tightly bound by the Coulomb interaction [98]. Each pair acts as an electrically-neutral quasiparticle, known as the exciton [99].

Classically, if an electron and hole are initially a distance r_{ex} from each other in a material with relative permittivity ϵ_r, the energy required to separate the particles is given by

$$E_{\text{B}} = \int_{r_{\text{ex}}}^{\infty} F \mathrm{d}r = \frac{e^2}{4\pi\epsilon_0\epsilon_r} \int_{r_{\text{ex}}}^{\infty} \frac{\mathrm{d}r}{r^2} = \frac{e^2}{4\pi\epsilon_0} \frac{1}{\epsilon_r r_{\text{ex}}}. \tag{5.1}$$

E_{B} is known as the exciton binding energy. The Bethe-Salpeter equation [100] provides a quantum mechanical treatment of the exciton binding energy [101, 102], necessary for accuracy at small r_{ex} where the effect of bound charges is no longer well-described by a continuum of relative permittivity ϵ_r. As discussed previously, the value of the exciton binding energy in a material determines whether it is *excitonic*. That is, whether excitons are present in significant number within the device or whether they dissociate quickly into free charges. From (5.1), the binding energy of the exciton depends on both the permittivity of the material and the size of the exciton, known as the exciton radius.

In terms of electron-hole separation, excitons can be broadly split into two types: Frenkel and Wannier-Mott excitons [99]. A Frenkel exciton has a small radius, less than the intermolecular spacing, with the exciton is localised on a single molecule. Excitons in organic devices are usually of this type [103, 104, 105]. A Wannier-Mott exciton has a radius much larger than the intermolecular spacing, spanning several molecules [99].

Organic materials have a low relative permittivity, usually in the range 3 to 4. Excitons in a small molecule organic material tend to be localised on a single molecule, with a small effective radius of perhaps a nanometre or smaller [106]. In organic polymers, they are localised to a region a few monomers in length, called a chromophore. Binding energies are usually in the range 300 to 600 meV, though can be well over 1 eV [107]. An electric field strength well in excess of 1 MV/cm would be required to split an exciton [106, 108]; the typical built-in field in an OSC is 0.1 MV/cm [109]. Organic materials are, therefore, decidedly excitonic.

Once an exciton is generated, if it is not split quickly the electron and hole will recombine. The rate at which this occurs is $1/\tau$, where τ is known as the exciton lifetime. Exciton lifetimes are material dependent, though typically around a nanosecond for most organics [110].

Excitons may exist in either a singlet or triplet state, with a total spin angular momentum of 0 or 1 respectively. Excitons that are generated by absorption of a photon must be singlets. Photons have spin 0, so to conserve spin the promoted electron must keep its original spin. The space left in the HOMO will be for an electron of that spin, and so the exciton can recombine. Triplets can be formed in OPV devices, and play an extremely important role in OLEDs, though we shall not consider them here.

Exciton dissociation

As the internal field is insufficient to overcome the binding, dissociation (splitting) of the exciton into free charges must occur by another means. This is achieved

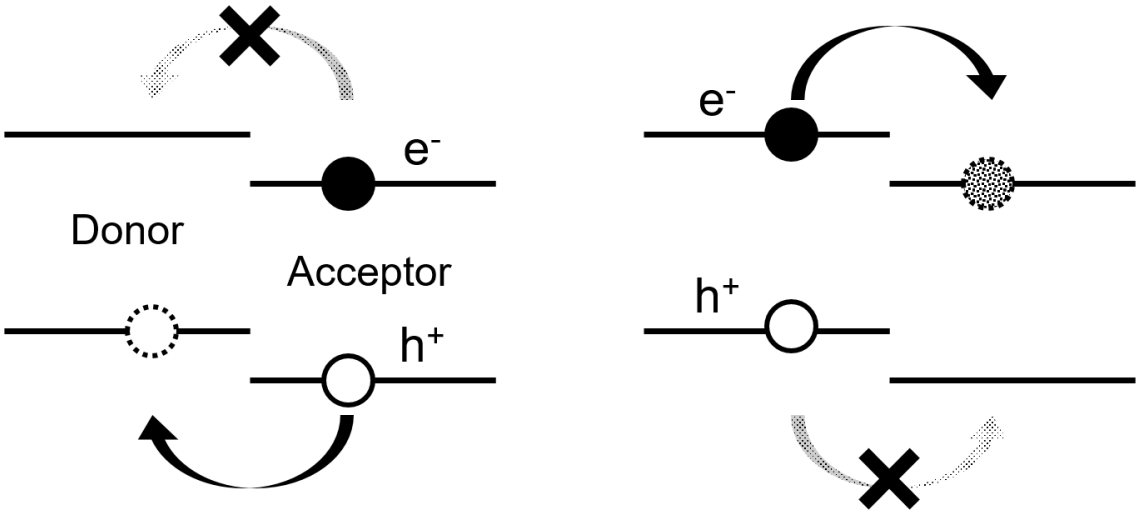

Figure 5.1: Dissociation from both sides of a donor-acceptor heterojunction. In the left panel, it is energetically favourable for the hole, but not the electron, to hop to the donor material. In the right panel, it is favourable for the electron, but not the hole, to hop to the acceptor. In this way, an exciton can be dissociated from either side of the interface.

by a heterojunction between an electron donor material and an electron acceptor material, known as a donor-acceptor (DA) interface [111]. For efficient dissociation from the donor side, the LUMO of the donor must be greater than the LUMO of the acceptor by more than the exciton binding energy so that it is energetically favourable for the electron to hop from the donor material to the acceptor [108],

$$D_{\mathrm{LUMO}} - A_{\mathrm{LUMO}} > E_{\mathrm{B}}. \tag{5.2}$$

Likewise for dissociation from the acceptor side,

$$D_{\mathrm{HOMO}} - A_{\mathrm{HOMO}} > E_{\mathrm{B}}. \tag{5.3}$$

These processes are shown in Figure 5.1. Needing to satisfy (5.2) and (5.3) is a major source of loss in OSCs, As excitons do need to be dissociated, however, this loss is seemingly unavoidable.

Once one of the charges has hopped to the other material, the exciton is dissociated and the charges can drift away from the interface to be collected. This occurs within the order of picoseconds [112]. If an exciton separates at an interface from the donor side where (5.2) is not satisfied, or from the acceptor side where (5.3) is not satisfied, the electron or hole can still hop to the other material, but will not fully dissociate. In this case a new quasiparticle called an exciplex or charge transfer (CT) state is formed, straddling the interface [113]. This can then dissociate into free charges, though the exact mechanism for this is still unclear [114]. It is thought that the carriers may separate quickly enough ($\sim$100 fs) to use excited 'hot' energy levels to clear each others influence to the point where the electric field from the difference in electrode potentials is sufficient to overcome the Coulomb interaction [115]. The electric field, then, reduces the barrier to dissociation, explaining the dependence of photocurrent on voltage [116]. In any case, the efficiency of CT separation is near unity in many organic systems at normal operating voltages [117].

The free carriers can then travel to the electrodes to be extracted, either by diffusion or drift from an electric field. As free electrons are only located in the acceptor material, it is often referred to as the electron conductor. Similarly for holes, the donor is called the hole conductor. Excitons can in principle generated in either material, provided the energy of the photon is at least the bandgap for that material. OSCs typically employ a polymer as the p-type electron donor and either another polymer or a fullerene derivative as the n-type electron acceptor component [118]. Conjugated polymers, which have a backbone of alternating single and double bonds, are often used due to their higher hole conductivity from overlapping p-orbitals creating a system of delocalised π-electrons [119]. Polymers generally have higher absorptivities than small molecules, especially fullerenes, so tend to be responsible for most of the generation within an OSC.

Förster Resonance Energy Transfer

In principle, an exciton may not be generated close enough to an interface to immediately dissociate and must migrate closer to a boundary. Singlet excitons, as would produced by absorption of a photon, may move from one molecule to another via Förster Resonance Energy Transfer (FRET) [120]. A singlet on one molecule, the donor, acts as an oscillating dipole and can couple to a non-excited molecule, the acceptor [121]. The dipole-dipole interaction allows the energy to be transferred from the donor, producing a new exciton on the acceptor – the exciton appears to instantaneously hop. If the donor and acceptor are the same material, this is referred to as homotransfer; else, if the materials are different, it is called heterotransfer.

The rate of FRET between two molecules is given by [120, 121, 122]

$$k_{\mathrm{FRET}} = \frac{1}{\tau}\left(\frac{R_0}{r}\right)^6 \tag{5.4}$$

where τ is the exciton lifetime, r is the distance between themolecules and R_0 is the Förster radius for the transition between those two molecules. The Förster radius is defined as the distance where the rate of FRET is equal to the radiative recombination (fluorescence) rate $1/\tau$, as can be seen by substituting $r = R_0$ into (5.4). The Förster radius can be calculated using

$$R_0^6 = \frac{9000 Q_0 (\ln 10)\kappa^2}{128\pi^5 n^4 N_A} J \tag{5.5}$$

where Q_0 is the fluorescence quantum yield of the donor, n the refractive index and N_A Avogadro's number.

κ is the orientation factor, defined as

$$\kappa = \mathbf{u}_D \cdot \mathbf{u}_A - 3(\mathbf{r}\cdot\mathbf{u}_D)(\mathbf{r}\cdot\mathbf{u}_A) \tag{5.6}$$

where $\mathbf{r}$ is the unit vector pointing from the donor to the acceptor and $\mathbf{u}_D$ and $\mathbf{u}_A$ are the unit vectors in the direction of the donor and acceptor dipole moment respectively. Computationally, κ^2 is often taken as $\langle\kappa^2\rangle = 2/3$. This average corresponds to the dynamic isotropic limit, where all dipoles are randomly aligned [123]. In the absence of knowledge on how excitons are actually aligned, this introduces the least extraneous information.

J is the overlap of the donor fluoresence spectrum with the acceptor absorption spectrum, given by

$$J = \int_0^\infty F_D(\lambda)\ \varepsilon_A(\lambda)\ \lambda^4\ \mathrm{d}\lambda \tag{5.7}$$

where $F_D(\lambda)$ is the normalised fluorescence spectrum of the donor, $\varepsilon_A(\lambda)$ the molar extinction coefficient of the acceptor and λ wavelength. It is important to note that, despite the dependence on the spectral overlap, FRET is a non-radiative process that uses the radiative pathway – no real photon is emitted or absorbed. The transfer can be described by emission and absorption of a virtual photon that transfers the energy instantly.

Device morphology

Once an exciton has dissociated, the liberated charges must be extracted at the correct electrodes. Charge carriers drift under the influence of the built-in field, electrons toward the anode and holes toward the cathode. As the exciton is electrically neutral, its path through the cell is unaffected by the built-in field. This poses a problem in a simple bilayer device, as illustrated in Figure 5.2, because an exciton generated in the bulk of a layer will undertake a random walk and may not encounter the interface. The root-mean-square displacement an exciton moves in a material between generation and recombination is known as the diffusion length. Excitons in organic semiconductors usually have diffusion lengths of the order 10 nm [110, 124], so only excitons generated within a distance of about 10 nm of the interface will dissociate. This cripples the efficiency of the device.

One solution to this problem is to simply introduce more interfacial area. This led to the development of the bulk heterojunction, or BHJ. The electron and hole conductors are intertwined on the nanoscale [109], as shown in Figure 5.2. This drastically increases the interfacial area and thus exciton dissociation efficiency (EDE), the fraction of generated excitons that dissociate. The extent of interpenetration is often characterised by the feature size [125], defined as

$$F = \frac{3V}{A} \tag{5.8}$$

where A is the interfacial area of the sample of volume V.

For the freed carriers to be extracted at the electrodes, they must traverse the morphology while remaining in their respective conducting layers. In a BHJ, the interpenetration of the conductors means there is a higher chance of a charge meeting its opposite and recombining across the interface. Increased interpenetration also increases the possibility of traps in the morphology where a particle gets stuck in a peninsular surrounded by the other conductor but cannot escape due to the electric field. There needs to be percolation paths for regions of each material to the appropriate electrode, else the regions will act as traps and dimish performance. Due to the simplicity of a bilayer, there is only the correct conducting layer between the particle and the electrode and so there is less loss from charge transport. The fraction of produced charges that are extracted defines the charge collection efficiency (CCE) of the device. There is, then, a trade off between good EDE for large feature size and good CCE for small feature size as the internal quantum efficiency (IQE) depends linearly on both these efficiencies. Watkins et al. [126] used a kinetic Monte

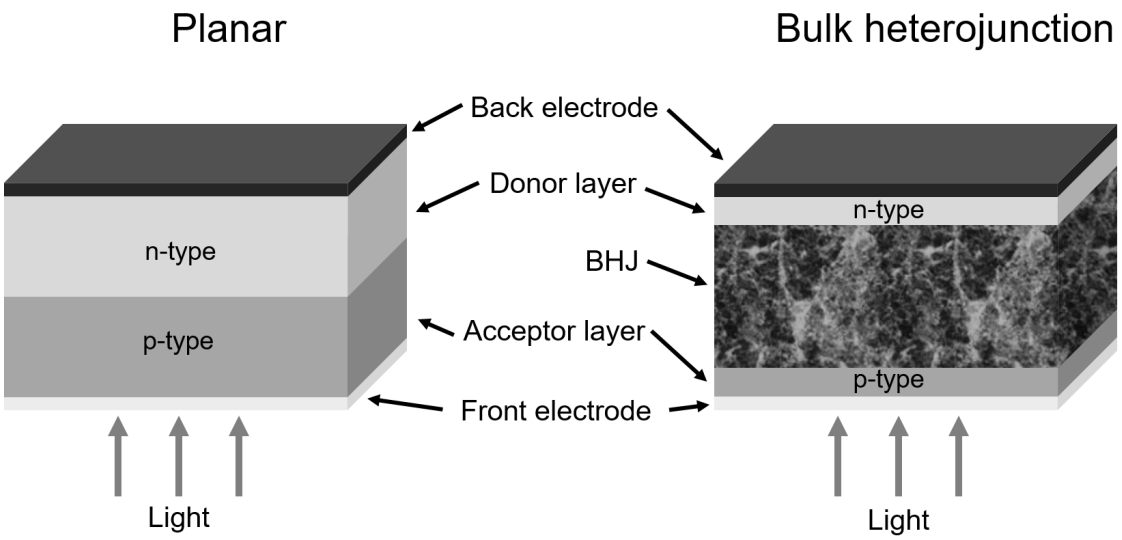

Figure 5.2: Illustration of planar and bulk heterojunction (BHJ) morphologies for OSCs. In the planar arrangement, flat sheets of acceptor and donor materials form a p-n junction. This has very little interfacial area for exciton dissociation, so is not very effective. In a BHJ, the acceptor and donor materials intricately permeate each other, forming a disordered structure with very large interfacial area. Optional buffer layers prevent charges reaching the wrong electrodes. Whether the p-type material is the layer on the front side (as depicted here) or the n-type is also optional.

Carlo approach to quantify the interplay between these two effects and found it led to a *Goldilocks* region of intermediate feature size where overall IQE was maximised. Figure 5.3 summarises the full set of processes for converting a photon to current, with each definition of efficiency.

Ternary OSCs

One reason for low efficiencies in organic materials is poor absorptivity of low-energy photons. Many organic materials used in OSCs have relatively wide bandgaps, with low or no absorption in the infra-red. In an effort to improve current, OPV devices with three active materials, known as ternary devices, have generated significant interest in recent years. These typically employ a near infra-red (NIR) sensitiser as a third material, designed to absorb in the otherwise wasted IR spectrum. This allows the cell to absorb more light overall, produce more current and hopefully therefore achieve higher power conversion efficiencies.

While ternary devices do deliver significantly better photocurrents, this has not translated into proportionately larger PCEs. The reason for this is that ternary OSCs suffer from poorer photovoltage than their binary (two material) counterparts. Figure 5.5 shows the energy levels in typical binary and ternary OSCs. For each carrier species to have an energetically favourable path its appropriate electrode, the band energies of the materials must be arranged such that LUMO levels decrease towards the anode and HOMO levels increase towards the cathode. This is known as a cascade structure. In addition, the energy offset at each interface needs to be chosen to be great enough to allow exciton dissociation. An offset of

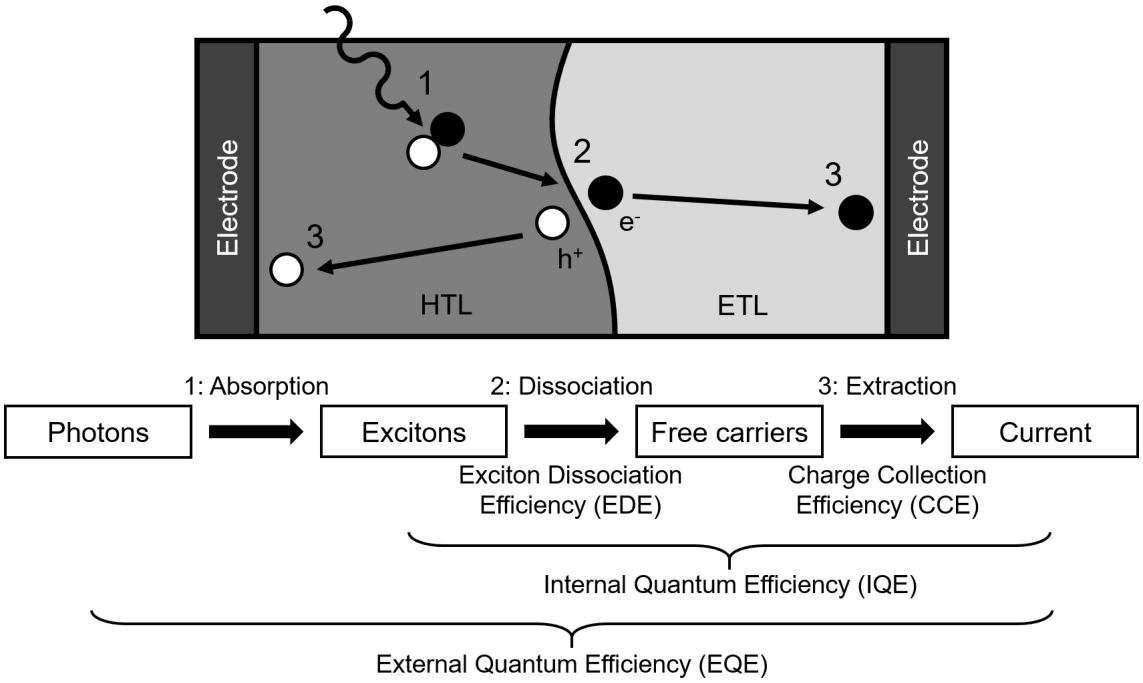

Figure 5.3: Illustration of the processes within an OSC for converting a photon to current, with relevant efficiencies. 1: a photon is absorbed, producing an exciton. 2: the exciton dissociates (efficiency EDE), producing a free hole and free electron. 3: the free carriers travel to their respective electrodes and are extracted (efficiency CCE), producing useful current. The efficiency of converting an already absorbed photon (an exciton) to current is the internal quantum efficiency (IQE). The overall efficiency of converting a photon before absorption to current is the external quantum efficiency (EQE).

$\sim$300 meV, a typical exciton binding energy, is often used. In principle excitons need to dissociate from both sides of the interface, so both (5.2) and (5.3) need to be satisifed simultaneously for a total offset of about 600 meV per interface [127]. As the built-in voltage of an OSC depends on the difference in electrode Fermi levels, depicted in Figure 5.5, the addition of the ternary material results in an additional 0.6 V overall reduction in possible photovoltage. This is on top of the minimum 0.6 V required from the single interface in the binary system. The strict energy band offset requirement is the single biggest limiting factor in OSC efficiency [128].

The energy levels for a typical ternary organic system, P3HT:DIBSq:PCBM is shown in Figure 5.6a. The system of P3HT:PCBM is very well studied in the field of OPV. The polymer P3HT acts as the electron acceptor (p-type) and the fullerene PCBM as the electron donor (n-type). An infra-red sensitiser DIBSq, with intermediate energy levels, may be added as the ternary material. Fortunately, due to surface energy effects, DIBSq congregates at the interface between P3HT and PCBM [129] leading to a cascade structure. Normally only a few percent of DIBSq by weight is used, an amount found to improve device performance significantly.

A key line of research in OPV is overcoming the band offset requirements for exciton dissociation. One possibility is to exploit Förster energy heterotransfer. Exciton diffusion within a material (homotransfer) is well known, but transfer from one material to another has been identified as an important process in ternary OSCs

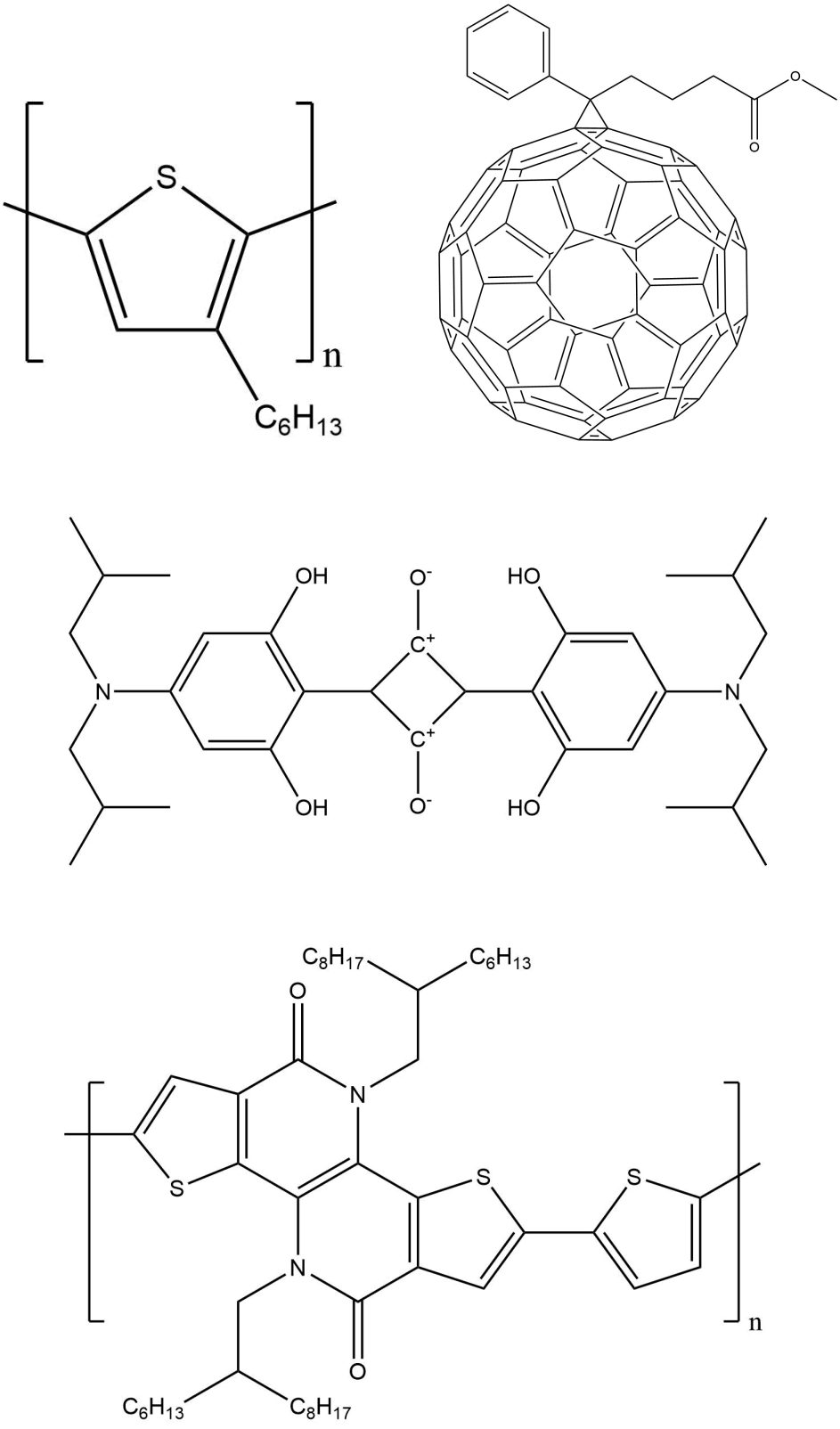

Figure 5.4: Chemical structures of organic semiconductors considered here. Top-left: polymer P3HT, often used as the electron acceptor. Top-right: fullerene derivative PCBM, often used as the electron donor. Centre: small molecule DIBSq, used as an infra-red dye. Bottom: polymer PTNT, a possible alternative for P3HT.

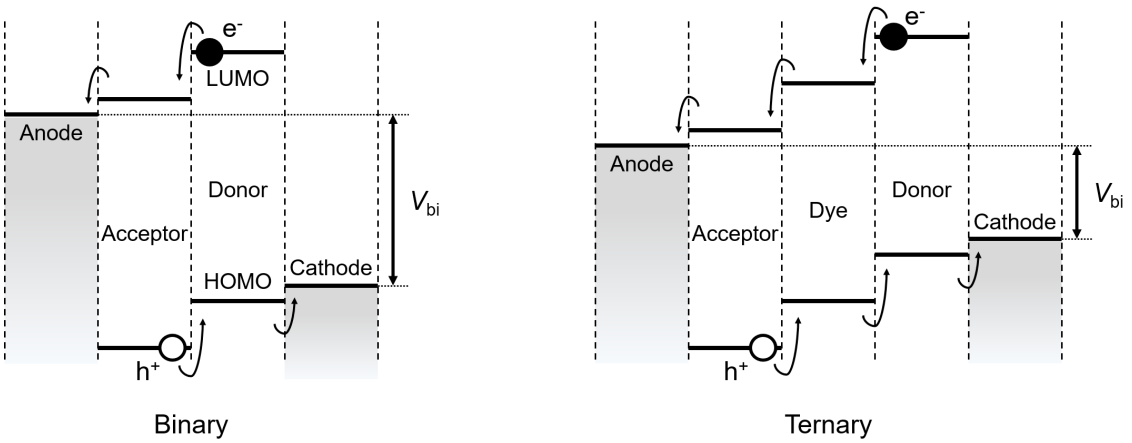

Figure 5.5: Binary and ternary device with band energies in the cascade structure. For organic materials, LUMOs are represented by the upper lines and HOMOs by the lower lines. For the electrodes, the lines represent Fermi levels. For an electron e^- in any material, there is a path of successively lower energies towards the anode; likewise for a hole h^+ towards the cathode. The built-in voltage, defined as the difference in Fermi levels between electrodes, for each device is labelled V_{bi}.

[130]. In fact, heterotransfer is often a far faster process than homotransfer, as the energy acceptor necessarily has a lower exciton energy (essentially the bandgap) than the donor. One obvious use of heterotransfer is to funnel excitons from the bulk of an energy donor to an interface with an energy acceptor, and thus improve dissociation efficiency. Another exciting possibility is to selectively funnel excitons from one side of an interface to another, and thus relax the neccessity for dissociation on the donor side. Related, specifically for ternary systems, is to funnel excitons into the ternary material and dissociate them all from there. In fact, if the ternary material domains are small enough, only a single offset may be needed.

An alternative acceptor layer for OSCs is PTNT, which has deeper HOMO and LUMO levels than P3HT. The PTNT:DIBSq:PCBM system is shown in Figure 5.6b. Due to the smaller energy offsets with DIBSq and PCBM, a ternary system containing P3HT can be expected to have a higher open-circuit voltage. However, the HOMO offset of PTNT with DIBSq is just 10 meV – not large enough to dissociate excitons from the DIBSq side of the interface. Excitons may still dissociate from the PTNT side, however, as the LUMO offset is greater than 300 meV.

In this chapter, we first examine the importance of energy heterotransfer in both binary and ternary systems. Then, using the ternary systems in Figure 5.6, explore if the band offset requirements may be relaxed by exploiting heterotransfer.

5.2 Kinetic Monte Carlo model

In order to model both the wide variety of events that may occur in an OSC and the widely different rates at which they occur, here we employ the kinetic Monte Carlo (KMC) method. KMC treats the evolution of a system as a sequence of discrete events. We provide the different events that can happen and how to calculate the rates at which they happen. A KMC simulation chooses a sequence of events to

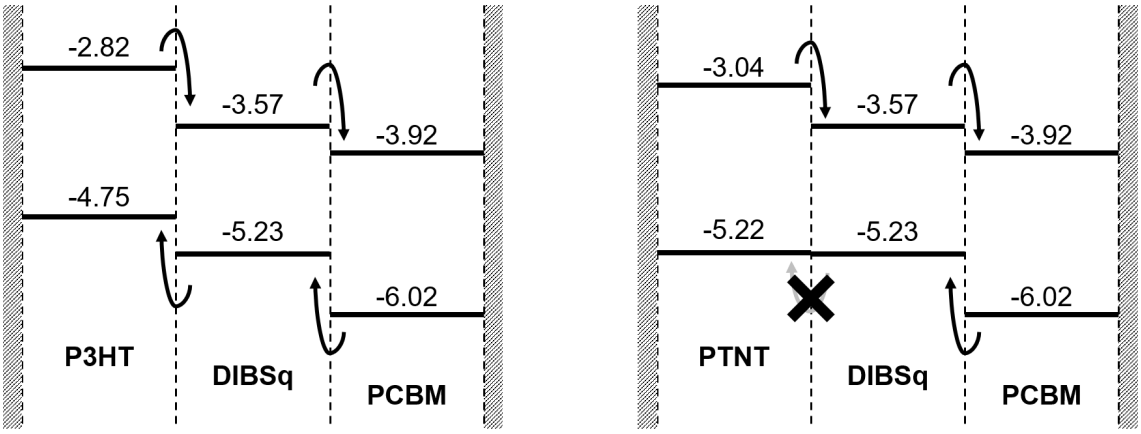

Figure 5.6: Band diagrams for a standard P3HT:DIBSq:PCBM system and the new PTNT:DIBSq:PCBM system. Energies are labelled in eV, possible exciton dissociation paths by arrows. With P3HT, the energy levels form a cascade structure with sufficient offsets that excitons can dissociate at either side of both interfaces. With PTNT, the ∼10 meV HOMO offset between PTNT and DIBSq is too small for excitons to dissociate from the DIBSq side of the interface.

occur, providing individual trajectories for the entities in the system.

There are two usual methods for implementing the KMC: the residence time algorithm (RTA) and first reaction method (FRM). The RTA is the direct way to implement the algorithm that closely follows the mathematics, while the FRM is an alternative method that can be more efficient for certain systems. The FRM also easily allows for a particularly efficient approximate implementation, though gives the exact same result as RTA if performed with full accuracy.

Residence Time Algorithm

At the start of the RTA loop, the rates for all n events that may occur in the system are calculated. An event is selected with a probability proportional to its rate, so the chance of event i with rate r_i being occurring is

$$P_i = \frac{r_i}{\sum_{j=1}^{n} r_j} \tag{5.9}$$

where the denominator is the sum of rates of all events. This can be calculated efficiently for event i by calculating the cumulative sum of rates for all events before and including i in the event list

$$C_i = \sum_{j=1}^{i} r_j. \tag{5.10}$$

We then generate a uniform random number u in the range $(0, C_n]$, where C_n is the sum of all rates, and pick the event i for which $C_{i-1} < u \leq C_i$. Using a binary search method allows this to be found in $O(\log_2 n)$ time. This event is then executed and the simulation clock incremented by

$$\delta t = -\frac{1}{C_n} \ln(v) \tag{5.11}$$

where v is a uniform random number in the range (0, 1]. This draws a number from a Poisson distribution, weighted by the total sum of rates, with an average value of $1/C_n$.

We can visualise the RTA by considering a number line. We place all of the C_i on the number line, which spans from 0 to C_n. The space between C_i and the previous value (or 0 for C_1) is r_i. We then pick a random point on the line, which will be in any spacing with a probability proportional to the width of the spacing.

Once this has been completed, the loop begins again. As it is usually expensive to completely recalculate everything again on the next step (unless there are very few possible events), some optimisation should be made to remember some of the event information from the previous loop to avoid unnecessary recalculation. For example, the execution of an event will usually only significantly impact the rates of other events nearby in space. For particles in a box, the algorithm might be optimised by compartmentalising the system into supercells and only recalculating events for particles in the same or neighbouring supercells as the most recent event.

First Reaction Method

The FRM uses the concept of an event queue, rather than a number line. As in the RTA, the first step is to calculate all the possible events and the rates at which they occur. Next, for each event i we calculate a waiting time for that event,

$$\tau_i = -\frac{1}{r_i}\ln(v) \tag{5.12}$$

where again v is a uniformly drawn random number in range (0, 1]. This uses the same logic as (5.11) in the RTA, but this time for each individual event rather than for the system as a whole. Each event is then placed into the queue in chronological order by τ, such that the event with the shortest τ is at the front, and the longest τ at the back. The KMC loop can then begin: the first event in the queue is executed, and the simulation time updated by that event's waiting time τ.

We now have a choice as to what happens next. If we throw away the queue and recalculate it from scratch, we obtain the same answer as the RTA with no approximations. Of course, in this case it is considerably more efficient to not store the queue at all. As we only need the fastest event, when calculating events we can simply store the event with the smallest τ_i found so far and overwrite this when we find a faster event.

Alternatively we can obtain a significant speed up for systems with a large queue by storing the queue between events. In this case, fully calculating the queue is done once, at the start of the simulation. After any event occurs, any new events that have become possible are given a waiting time using (5.12) and inserted into the queue at the appropriate points to conserve chronological order.

This leads to the complication that execution of one event may invalidate a later one; for example, if a particle recombines then it can no longer move. As such, all events must be checked for validity before execution. If an event is no longer valid it is discarded. In addition, the rates of certain events may change without the event becoming invalid. For example, the movement of a charged particle changes the motion of any nearby charged particles. To rectify this we would need to store which events depend on each other, which may be difficult and expensive. Otherwise, any error from outdated events can simply be accepted. This is likely to especially

hamper the accuracy of modelling rare events, as these slow events are most likely to remain in the queue for longest.

As a compromise between fully recalculating the queue each step and dealing with outdated events, a hybrid scheme may be employed where a full queue recalculation happens after some chosen number of steps and the queue is reused in the meantime. This stops the queue from becoming too 'stale' while still offering a significant speed up.

One major benefit of the FRM over the RTA is that only the fastest from a set of mutually exclusive group of events will occur. An electron may be able to move from its current position to one of tens or hundreds of nearby sites, for example, but only the fastest need be recorded in the queue. Once the electron has moved from its initial position, all events from that initial position to any other positions would be invalidated. Therefore, only the fastest event from a set of mutually exclusive events need be stored. Another boost to computational efficiency comes from storing the queue from one Monte Carlo step to the next, at the cost of some accuracy.

KMC model for exciton dynamics

For this study, the first reaction method (FRM) is used. As we are primarily interested in the dynamics of energy transfer, the only particle we consider is the exciton. The morphology of the system consists of a cubic lattice of sites with a spacing of 1 nm. Each site is a certain material and has an associated exciton energy. The exciton energy for each site is randomly drawn from a Gaussian distribution with standard deviation σ. Only one exciton may exist on a site at a time, and generation on or hopping to an occupied site is forbidden. The temperature for all simulations is 300 K.

Possible events for the system are exciton movement, generation, recombination and dissociation. Excitons may hop from one site to another via FRET, as in (5.4). We modify this with a Boltzmann multiplier to reduce the rate of hops that result in an increase in energy:

$$k_{\text{FRET}} = \frac{1}{\tau}\left(\frac{R_0}{r}\right)^6 \times \begin{cases} \exp\left(-\frac{\Delta E}{k_B T}\right) & \Delta E > 0 \\ 1 & \text{otherwise} \end{cases} \tag{5.13}$$

where k_B is the Boltzmann constant, T temperature and ΔE the change in energy from the hop. Excitons may hop to a site of the same material or a material with a smaller bandgap. Hopping to a site of a different material with a larger bandgap is not possible due to the large increase in energy this requires.

Generation is uniform across the system with a rate 10 $s^{-1}nm^{-3}$ or 10 s^{-1} per site, which was found to approximate the standard AM1.5 spectrum for a layer thickness $\sim$100 nm. Excitons recombine with a material dependent rate $1/\tau$.

At a boundary site, which we define to be any site adjacent to another site of a different material, an exciton may dissociate. This is handled separately from other events. When an exciton hops to (or is generated on) an interface site, it has a probability p to dissociate instantly. If it does not dissociate, it remains in the system as normal and can continue to hop through the system or recombine. If the exciton hops to an interface site again it has another chance to dissociate. The probability p can be varied for each side of the same boundary; e.g. the dissociation

Material	Q_0 (%)	L (nm)	τ (ns)	σ (eV)
P3HT	25	8.5 [132]	0.9 [133]	0.06
PCBM	8.3×10^{-2} [134]	5 [135]	1.43 [134]	0.09
PTNT	32	8.5	0.9	0.09
DIBSq		2 [136]	4.9 [133]	0.05

Table 5.1: Fluorescence quantum yield Q_0, diffusion length L, exciton lifetime τ and excitonic energy disorder σ for the four materials studied.

R_0 (nm)		Acceptor			
		P3HT	PTNT	PCBM	DIBSq
Donor	P3HT	2.3		2.7	5
	PTNT		2.3	2.8	5.2
	PCBM			2.3	1.2
	DIBSq				1.1

Table 5.2: Förster radii for relevant energy transfer combinations.

probability from the P3HT side of a P3HT:PCBM interface may differ from the probability from the PCBM side.

Materials

The values for fluorescence quantum yield Q_0, exciton diffusion length L, exciton lifetime τ and exciton energy disorder σ for each material as used are given in Table 5.1. Cited values were taken from literature. Q_0 values for P3HT and PTNT were measured in-house by collaborators at the University of Newcastle using a standard procedure [131]. Q_0 for DIBSq was not needed as it did not act as the donor in any FRET pathways. L and τ for PTNT were assumed to be the same as in P3HT as both have similar optimal feature sizes when paired with $PC_{70}BM$. σ was found by fitting a Gaussian to the measured absorbance spectrum of each material.

The Förster Radii for heterotransfer were calculated using (5.5) and (5.7), the values in Table 5.1 and measured fluorescence and absorbance spectra. A refractive index n of 1.4 was used for all materials. The dipole orientation factor κ was taken so that κ^2 was 2/3 for all transfers, which corresponds to the average value if dipoles are oriented randomly [123].

R_0 values for homotransfer were calculated using the KMC. For each material for a range of R_0 values, a $100\times100\times100$ nm^3 box was simulated with exciton energy levels distributed normally with the appropriate standard deviation σ in Table 5.1. An exciton was placed in the centre of the box and allowed to hop through the system until recombination; its absolute displacement from the starting position was then recorded. Periodic boundaries existed in all three dimensions, and the number of times the exciton crossed the periodic boundaries kept track of so as to simulate an infinitely large box. Upon recombination, the energy landscape was randomised and a new exciton placed. This was repeated 10,000 times for each R_0, and the root-mean-square of the set of displacements taken to give the exciton diffusion length L as a function of R_0. R_0 was varied in 0.1 nm intervals, and the value taken giving the closest L to that from literature in Table 5.1. The full set of Förster Radii are given in Table 5.2.

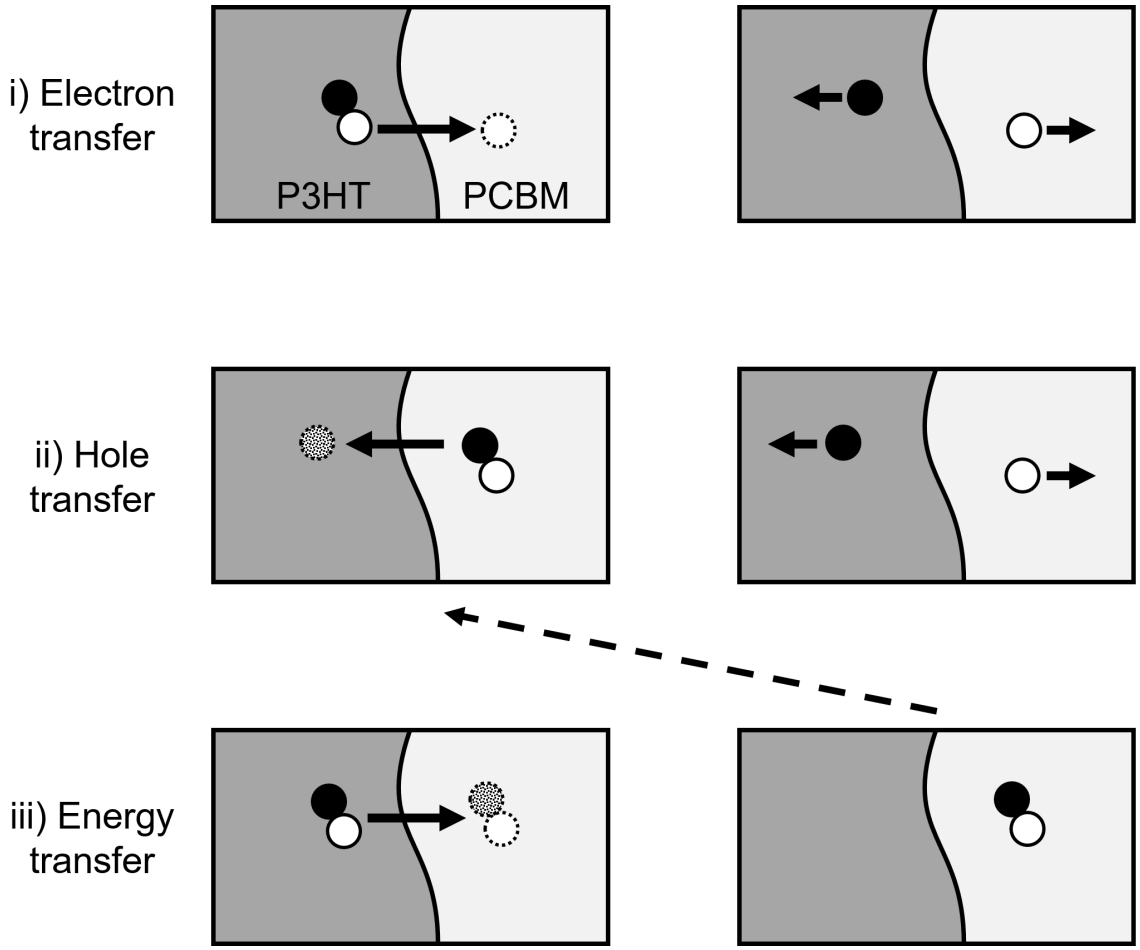

Figure 5.7: Exciton dissociation mechanisms in a binary P3HT:PCBM system. (i) An exciton in P3HT dissociates by electron transfer to PCBM. (ii) An exciton in PCBM dissociates by electron transfer to P3HT. (iii) An exciton in P3HT heterotransfers to PCBM. Afterwards, the hole may transfer back to the P3HT (dashed line). We refer to the combination of (iii) followed by (ii) as the two-step dissociation process.

5.3 Impact of heterotransfer in a binary BHJ

Exciton dissociation efficiency (EDE) is a crucial metric for an OSC, as a poor EDE results in fewer produced free charges and thus less current. Dissociation occurs via one of the processes in Figure 5.7. In (i), an exciton is generated in the P3HT domain and hops via homotransfer within the material to the boundary with PCBM. As both the HOMO and LUMO of P3HT are higher than those of PCBM, electron transfer is energetically favourable but hole transfer is not. This also leads to the situation in (ii), where an exciton in the PCBM phase may dissociate by the hole transferring to the P3HT.

A third process is also possible: an exciton generated in the P3HT may heterotransfer to the PCBM as in (iii) and then dissociate from that side of the interface as in (ii). This is possible as the bandgap of PCBM, i.e. the difference in HOMO and LUMO levels, is smaller than that of P3HT and PCBM absorbs light at wavelengths where P3HT fluoresces. The rate of heterotransfer determines how prevalent this process, which we call the two-step mechanism, is in the device. Heterotransfer is

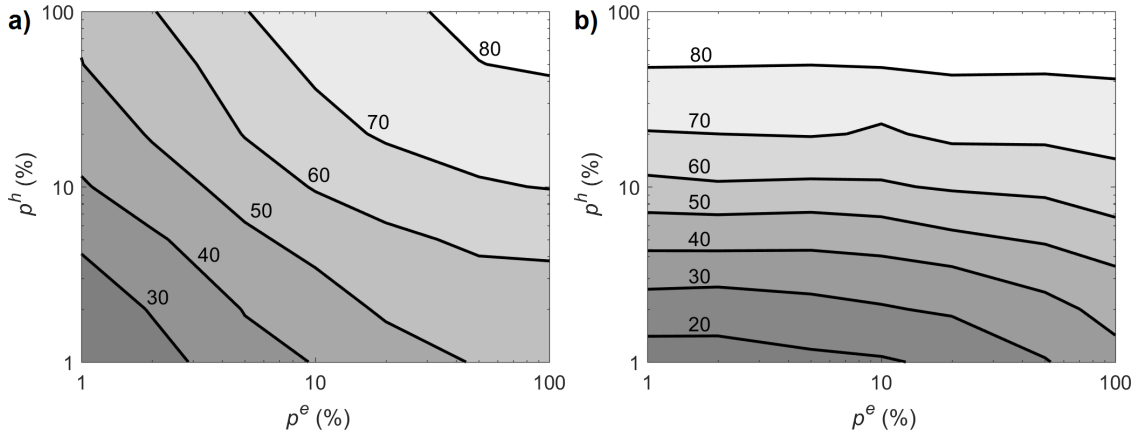

Figure 5.8: Exciton dissociation efficiencies (EDEs) in percent as a function of the electron and hole transfer probabilities p^e and p^h for the same morphology when energy transfer from P3HT to PCBM is (a) ignored and (b) included.

often neglected, however, when simulating exciton dissociation in binary systems. Here, we investigate the effect heterotransfer has on the EDE of a binary device to evaluate whether this is a reasonable approximation.

The rate at which an exciton dissociates at an interface depends depends on the offset between the HOMO levels of the materials for hole transfer driven dissociation, such as from the PCBM side of a P3HT:PCBM interface, or between the LUMO levels for electron transfer driven, as from the P3HT side of P3HT:PCBM [137]. In the model, this corresponds to the dissociation probability p. As we are interested in varying p for each side of the interface, we denote p^e as the probability of the exciton dissociating from the P3HT side via electron transfer and p^h as the probability from the PCBM side.

To quantify the importance of heterotransfer, we studied a 1:1 P3HT:PCBM BHJ morphology with feature size 15 nm and varied p^e and p^h between 1% and 100%. The morphology was created by collaborators at the University of Newcastle using the cellular automata method described elsewhere [138]. The method is similar to the Ising model: sites are randomly assigned a material type, and then randomly swapped with a an Ising style probability that gradually builds domains. The system was 80×80×80 sites large, with periodic boundaries enabled. For each point, 100 simulations were run for 10 µs each, with the energy landscape randomised at the start of each simulation. EDE was calculated as the fraction of excitons that dissociated of those generated. Figure 5.8 gives the obtained EDE as a function of p^e and p^h for (a) without and (b) with heterotransfer.

When heterotransfer is not included, p^e and p^h each have about the same impact on the EDE. This is because, with heterotransfer disabled and mechanism (iii) in Figure 5.7 not possible, each exciton must dissociate from the side of the boundary it was generated on and half the excitons will be generated in each material. If a binary device was fabricated using materials where heterotransfer could not happen efficiently, it would be important to optimise both the HOMO and LUMO energy offsets to ensure both (i) and (ii) are efficient.

With heterotransfer on, however, p^h dominates the EDE and p^e has relatively little effect. An exciton on the P3HT side can still efficiently dissociate via the two-step mechanism, despite a low p^e. Mechanisms (ii) and (iii) are both viable paths

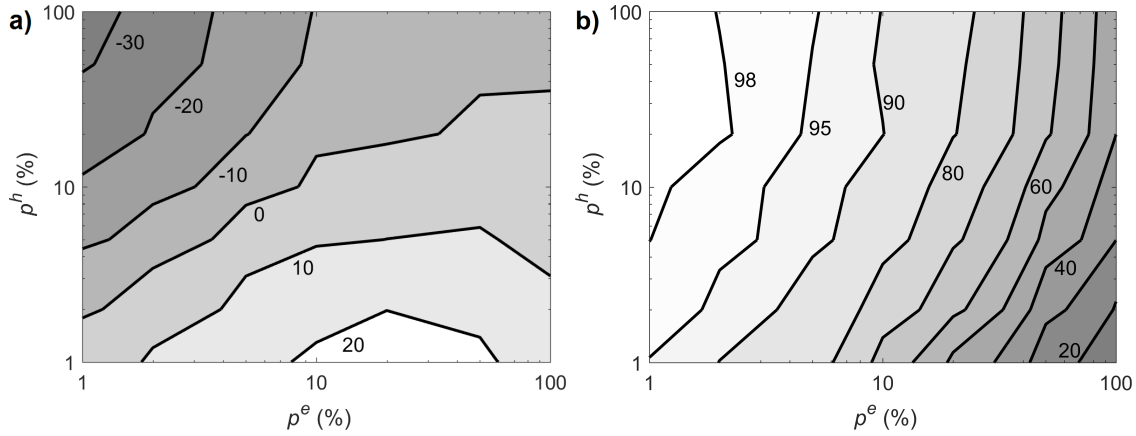

Figure 5.9: (a) Difference in EDEs between ignoring and including heterotransfer, in percentage points. The dashed line shows where $p^e = p^h$, and the difference in EDEs is ≈ 0. (b) The fraction of dissociated P3HT excitons that underwent the two-step process, in %.

for a P3HT exciton to dissociate, so only one of these paths need be optimised. Mechanism (i) is the only path for a PCBM exciton to dissociate, and so this needs to be efficient for a high EDE. Some excitons in the P3HT will transfer across to the PCBM even if p^e is high, further increasing its importance.

In general, we find that to obtain a good EDE in a binary system the following must be efficient: (ii) the dissociation from the FRET acceptor side of the interface and *either* (i) dissociation from the FRET donor side *or* (iii) heterotransfer from the donor to acceptor. As noted previously, one of the major voltage loss mechanisms in organics cells is the need to have relatively large offsets ($\sim$ 300 meV) in the HOMO and LUMO levels at the interface to ensure good EDE (mechanisms (i) and (ii)). Heterotransfer can be exploited here by not including the offset required for excitons in the FRET donor material, improving the photovoltage, but ensuring they can still dissociate via the two-step process (mechanisms (iii) then (ii)), maintaining photocurrent.

The difference between the EDEs in Figure 5.8 (without heterotransfer minus with) is shown in Figure 5.9a. If $p^e \sim p^h$, ignoring heterotransfer will still predict the correct EDE to within a few percentage points. This is denoted by the dashed line in the figure. When the p^e and p^h differ considerably, it is crucial to consider mechanism (iii) to obtain an accurate answer.

In P3HT:PCBM blends, we can estimate p^e based on the rate of the exciton to decay radiatively in P3HT $k_{rad} = 1.67$ GHz [139], decay non-radiatively $k_{nonrad} = 5$ GHz [140] and dissociate $k_{dissoc} = 100$ GHz [139] using

$$p = \frac{k_{dissoc}}{k_{rad} + k_{nonrad} + k_{dissoc}} \tag{5.14}$$

which comes to about 94%. Hole transfer is about 100 times faster that electron transfer [139], which leads to $p^h \approx 100\%$. Since the p's are similar, ignoring heterotransfer will not significantly over or underestimate EDE for the P3HT:PCBM system.

The fraction of dissociated P3HT-generated excitons that undergo the two-step dissociation process is shown in Figure 5.9b. As the P3HT-side dissociation proba-

bility p^e decreases, the fraction of excitons undergoing two-step dissociation increases leading to the low dependence of EDE on p^e seen in Figure 5.8b. For P3HT:PCBM, with $p^h = 100\%$ and $p^e \approx 100\%$, 43% of dissociated P3HT excitons do so using the two-step mechanism. Even though excluding heterotransfer does not affect the calculated EDE in this case, it is neglecting this important behaviour. If p^e were smaller, such as if we were to exploit the two-step mechanism to increase photovoltage by eliminating an energy offset as mentioned earlier, virtually all P3HT excitons would use this path. It is important to consider heterotransfer in OSCs not just so that dissociation dynamics are accurately described, but also because this opens possible avenues to improve the devices.

5.4 Exciton dissociation in a ternary organic system

Binary systems, such as P3HT:PCBM, have only one interface and thus two energy offsets, one between the HOMOs and another between the LUMOs, to drive exciton dissociation. In a ternary BHJ, such as P3HT:DIBSq:PCBM, there are three possible interfaces (P3HT:PCBM, P3HT:DIBSq and DIBSq:PCBM) and so six energy offsets. Since it is unlikely that all six offsets will result in the same p, heterotransfer becomes a necessary consideration to calculate EDE accurately.

The P3HT:DIBSq:PCBM BHJ system employs DIBSq as an infrared sensitiser. From energy-dispersive x-ray elemental mapping and studies of surface energy, DIBSq regions are located at the P3HT:PCBM interface [130]. Further evidence comes from considering the energy structure of the system, as given in Figure 5.6a. P3HT:DIBSq:PCBM forms an energy cascade structure, where electrons in the LUMO can successively hop from P3HT to DIBSq to PCBM, and reverse for holes in the HOMO. The observed optimum concentration for DIBSq is less than 5%, which is far too low to form continuous paths to the electrodes. For DIBSq to improve performance and be photo-active in the EQE spectrum as observed, each region of DIBSq must be simultaneously able to pass holes to the P3HT and electrons to the PCBM. If DIBSq existed purely within a region of P3HT, there would be nowhere for electrons in the DIBSq to go to – the entire DIBSq region would act as a trap. The same logic applies for a region of DIBSq in PCBM, as such a region would trap holes. Therefore, DIBSq domains must be in contact with both other materials.

In our model, the simulated ternary structures were produced by taking binary P3HT:PCBM systems, generated using the cellular automata method, and randomly replacing P3HT:PCBM interface sites with DIBSq until the desired DIBSq concentration was reached. As all six offsets in the electronic cascade structure, shown in Figure 5.6a, are of at least the order of the exciton binding energy, the dissociation probability p for each interface is set to 1.

The EDE as a function of the DIBSq content for three feature sizes is shown in Figure 5.10a. The addition of a few percent of DIBSq relative to P3HT significantly improves the EDE for all feature sizes. As discussed previously, smaller feature sizes have a naturally larger EDE due to the shorter distance on average to an interface and so the effect of the DIBSq is most pronounced for the larger 31 nm feature size morphology. Addition of more DIBSq always results in better EDE, though with

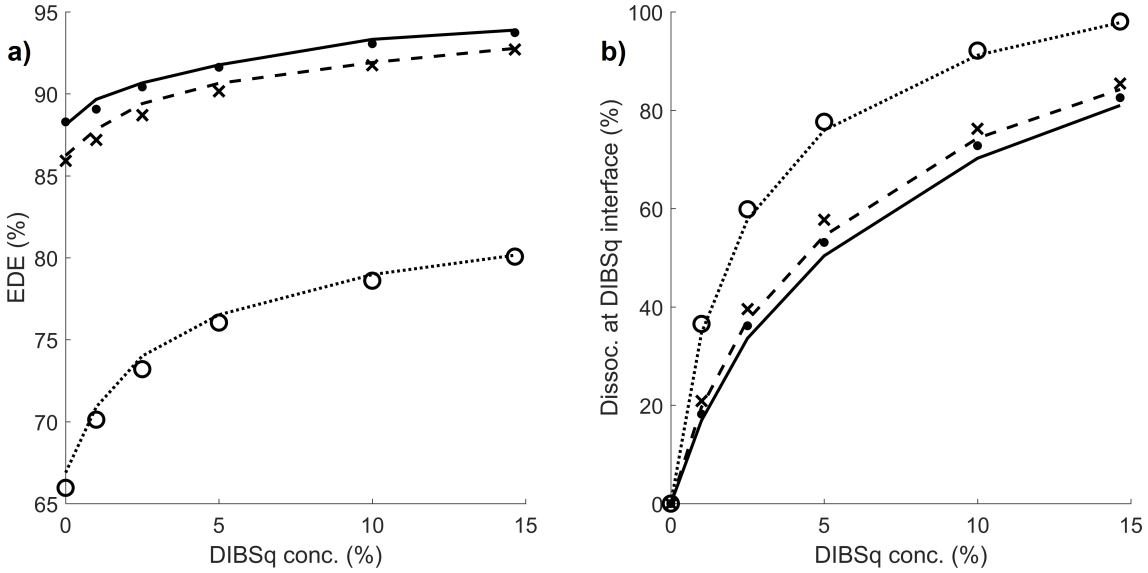

Figure 5.10: (a) Exciton dissociation efficiency (EDE) as a function of DIBSq content for ternary BHJs of P3HT:DIBSq:PCBM (markers) and PTNT:PCBM:DIBSq (lines) with feature sizes of 14 nm (dots, solid line), 15 nm (crosses, dashed line) and 31 nm (circles, dotted line). (b) Fraction of excitons that dissociated which did so at an interface with DIBSq.

diminishing returns.

To determine the importance of the energy cascade structure in ternary blends, the P3HT is replaced in the model with PTNT [141]. PTNT does not form a cascade structure with DIBSq and PCBM, eliminating an energy offset as illustrated in Figure 5.6b. An exciton in DIBSq cannot dissociate at an interface with PTNT as it can with P3HT as the HOMO offset for PTNT:DIBSq is only 10 meV, over an order of magnitude lower than the exciton binding energy. In this simulation, p for excitons on the DIBSq side of a PTNT:DIBSq is set to 0. A free hole, not bound with an electron, can still transfer from the DIBSq to the PTNT. In addition, an exciton on the PTNT side of the PTNT:DIBSq interface can still dissociate due to the large LUMO offset ∼500 meV.

Figure 5.10a shows no loss in EDE for the PTNT system as we might expect. While excitons in DIBSq cannot dissociate with the PTNT, the DIBSq domains are small enough for excitons to usually find an interface with PCBM where they can dissociate. This shows that a full cascade energy structure is not needed for an efficient ternary device.

The EDE improvement with addition of DIBSq can be explained by the Förster radius. As Table 5.2 shows, R_0 for homotransfer is 2.3 nm for P3HT and PTNT. These values contrasts with the very large Förster radii of 5 and 5.2 nm for heterotransfer from P3HT and PTNT respectively to DIBSq. Because the rate of Förster transfer is proportional to the sixth power of R_0, this results in a hop from either P3HT or PTNT to DIBSq being over 100 times faster than a homotransfer hop of the same distance. The large R_0 results in efficient, long range energy transfer from P3HT and PTNT to DIBSq, where the exciton soon dissociates due to the small domain size. The small domain sizes of DIBSq also explain the optimum content on that material being only <5% [130]. When a large amount of DIBSq is added, this

is likely to build up large domains of the material at the P3HT:PCBM interface. When the interface approaches saturation, it is possible that isolated domains of DIBSq may form in the bulk of the other materials, acting as traps as discussed earlier.

The intended advantage of adding a third material to an organic device is better light absorption leading to larger photocurrents. This is important as organic cells suffer from low photocurrents due to the bandgaps of most organic materials ($\sim$2 eV) being larger than the optimum bandgap calculated from the Shockley-Queisser limit ($\sim$1.4 eV). The trade-off is that open-circuit voltages in ternary organic devices are generally lower than in their binary counterparts due to the additional energy level offsets required to dissociate excitons. These results show that this trade-off may be made less severe or even eliminated completely if excitons can be moved from interfaces with small offsets to those with larger offsets. In the PTNT:DIBSq:PCBM case the movement was simply diffusion to the DIBSq:PCBM interface due to the small domain size of the DIBSq dye.

This can also be achieved with energy transfer. By selecting a dye so that hops from the other two materials to the dye have a large R_0, e.g. P3HT or PTNT to DIBSq, excitons would be efficiently funnelled from all over the device to the dye domains. Figure 5.10b demonstrates the importance that just a small amount of DIBSq has – around half of dissociating excitons do so at a DIBSq interface, even with just 5% DIBSq content. For BHJs with large feature sizes, this fraction rises to 80%. This means only the two offsets from the dye to the other materials need be large enough to dissociate excitons. If the domains of the dye are small, such as for DIBSq, only a single offset is needed. By minimising the energy offsets, we eliminate the disadvantage ternary cells have compared to binary in the lower photovoltage, but maintain the advantages of better light absorption.

Note that here we only consider the excitons in a BHJ. To calculate the internal quantum efficiency (IQE) of a device we must also consider the fraction of liberated charges that are successfully extracted before they recombine, the charge collection efficiency (CCE). Larger feature sizes are better for charge collection efficiency, but lead to worse exciton dissociation efficiency. As Figure 5.10 shows, the EDE improvement found by adding a small amount of DIBSq is largest for larger feature sizes. This is because long range heterotransfer allows excitons in the bulk of the P3HT or PTNT domains to make a large hop directly to the interfacial region. Excitons in morphologies with smaller feature sizes are highly likely to dissociate anyway, and so long range transfer does not have as great a benefit. The addition of DIBSq is most effective for BHJs with larger feature sizes, as this will mitigate the poor EDE while maintinaing the naturally good CCE.

5.5 Conclusion

The dissociation efficiency of excitons in organic solar cells has been simulated using a kinetic Monte Carlo model. Within the model, excitons may be generated by photon absorption, recombine, dissociate at an interface and diffuse throughout the simulation volume through Förster resonance energy transport (FRET). Both homotransfer between two sites of the same material and heterotransfer between two sites of different materials are considered. Using Förster radii and other material properties calculated from experiment, heterotransfer is found to be prevalent

in bulk heterojunctions consisting of either two or three materials. Heterotransfer is found to funnel excitons from the bulk of the energy donor material to interface sites of the energy acceptor, providing an efficient pathway for dissociation. Heterotransfer is particulary widespread in ternary devices of P3HT:DIBSq:PCBM and PTNT:DIBSq:PCBM, due to the particularly large Förster radius between the energy donors P3HT and PTNT and the energy acceptor DIBSq.

The efficient funnelling of excitons to DIBSq may be exploited in ternary systems to improve exciton dissociation efficiency (EDE). Improvement in EDE is strongest for bulk heterojunctions with a large feature size, which tend to suffer from lower EDE. One of the major shortfalls of ternary organic solar cells is the requirement for an additional set of significant band energy offsets, hindering maximum obtainable photovoltage. Förster heterotransfer relaxes this requirement, by providing an alternative path to dissociation. In short, Förster resonance energy transport of excitons between materials offers an enticing way to improve the performance of organic solar cells.

References

[1] K. Feron, J. M. Cave, M. N. Thameel, C. O'Sullivan, R. Kroon, M. R. Andersson, X. Zhou, C. J. Fell, W. J. Belcher, A. B. Walker, and P. C. Dastoor, "Utilizing energy transfer in binary and ternary bulk heterojunction organic solar cells," *ACS Appl. Mater. Interfaces*, vol. 8, pp. 20928–20937, 2016.

[2] S. E. J. O'Kane, G. Richardson, A. Pockett, R. G. Niemann, J. M. Cave, N. Sakai, G. E. Eperon, H. J. Snaith, J. M. Foster, P. J. Cameron, and A. B. Walker, "Measurement and modelling of dark current decay transients in perovskite solar cells," *J. Mater. Chem. C*, vol. 5, pp. 452–462, 2017.

[3] K. Yasuda and T. H. Okabe, "Solar-grade silicon production by metallothermic reduction," *J. Min. Met. Mat. S.*, vol. 62, pp. 94–101, 2010.

[4] J. Nelson, *The physics of solar cells*. Imperial College Press, London, UK, 2003.

[5] S. Rühle, "Tabulated values of the Shockley–Queisser limit for single junction solar cells," *Sol. Energy*, vol. 130, pp. 139–147, 2016.

[6] Z. Li, T. R. Klein, D. H. Kim, M. Yang, J. J. Berry, M. F. A. M. van Hest, and K. Zhu, "Scalable fabrication of perovskite solar cells," *Nat. Rev. Mater.*, vol. 3, p. 18017, 2018.

[7] A. Kojima, K. Teshima, Y. Shirai, and T. Miyasaka, "Organometal halide perovskites as visible-light sensitizers for photovoltaic cells," *J. Am. Chem. Soc.*, vol. 131, pp. 6050–6051, 2009.

[8] National Renewable Energy Laboratory, "NREL research cell record efficient chart," 2018.

[9] N. J. Jeon, H. Na, E. H. Jung, T.-Y. Yang, Y. G. Lee, G. Kim, H.-W. Shin, S. Il Seok, J. Lee, and J. Seo, "A fluorene-terminated hole-transporting material for highly efficient and stable perovskite solar cells," *Nat. Energy*, vol. 3, pp. 682–689, 2018.

[10] F. Sahli, J. Werner, B. A. Kamino, M. Bräuninger, R. Monnard, B. Paviet-Salomon, L. Barraud, L. Ding, J. J. Diaz Leon, D. Sacchetto, G. Cattaneo, M. Despeisse, M. Boccard, S. Nicolay, Q. Jeangros, B. Niesen, and C. Ballif, "Fully textured monolithic perovskite/silicon tandem solar cells with 25.2% power conversion efficiency," *Nat. Mater.*, 2018.

[11] B. O'Regan and M. Grätzel, "A low-cost, high-efficiency solar cell based on dye-sensitized colloidal TiO_2 films," *Nature*, vol. 353, pp. 737–740, 1991.

[12] N. Heo, Y. Jun, and J. H. Park, "Dye molecules in electrolytes: new approach for suppression of dye-desorption in dye-sensitized solar cells," *Sci. Rep.*, vol. 3, p. 1712, 2013.

[13] H. J. Snaith and L. Schmidt-Mende, "Advances in liquid-electrolyte and solid-state dye-sensitized solar cells," *Adv. Mater.*, vol. 19, pp. 3187–3200, 2007.

[14] S. Yun, P. D. Lund, and A. Hinsch, "Stability assessment of alternative platinum free counter electrodes for dye-sensitized solar cells," *Energy Environ. Sci.*, vol. 8, pp. 3495–3514, 2015.

[15] J.-H. Im, C.-R. Lee, J.-W. Lee, S.-W. Park, and N.-G. Park, "6.5% efficient perovskite quantum-dot-sensitized solar cell," *Nanoscale*, vol. 3, pp. 4088–4093, 2011.

[16] L. Schmidt-Mende, S. M. Zakeeruddin, and M. Grätzel, "Efficiency improvement in solid-state-dye-sensitized photovoltaics with an amphiphilic ruthenium-dye," *Appl. Phys. Lett.*, vol. 86, p. 013504, 2005.

[17] M. M. Lee, J. Teuscher, T. Miyasaka, T. N. Murakami, and H. J. Snaith, "Efficient hybrid solar cells based on meso-superstructured organometal halide perovskites," *Science*, vol. 338, pp. 643–647, 2012.

[18] M. Liu, M. B. Johnston, and H. J. Snaith, "Efficient planar heterojunction perovskite solar cells by vapour deposition," *Nature*, vol. 501, pp. 395–398, 2013.

[19] J. Even, L. Pedesseau, and C. Katan, "Analysis of multivalley and multibandgap absorption and enhancement of free carriers related to exciton screening in hybrid perovskites," *J. Phys. Chem. C*, vol. 118, pp. 11566–11572, 2014.

[20] Q. Lin, A. Armin, R. C. R. Nagiri, P. L. Burn, and P. Meredith, "Electro-optics of perovskite solar cells," *Nat. Photon.*, vol. 9, pp. 106–112, 2015.

[21] A. Miyata, A. Mitioglu, P. Plochocka, O. Portugall, J. T.-W. Wang, S. D. Stranks, H. J. Snaith, and R. J. Nicholas, "Direct measurement of the exciton binding energy and effective masses for charge carriers in organic-inorganic tri-halide perovskites," *Nat. Phys.*, vol. 11, pp. 582–587, 2015.

[22] Q. Jiang, Z. Chu, P. Wang, X. Yang, H. Liu, Y. Wang, Z. Yin, J. Wu, X. Zhang, and J. You, "Planar-structure perovskite solar cells with efficiency beyond 21%," *Adv. Mater.*, vol. 29, p. 1703852, 2017.

[23] M. Yang, Z. Li, M. O. Reese, O. G. Reid, D. H. Kim, S. Siol, T. R. Klein, Y. Yan, J. J. Berry, M. F. A. M. van Hest, and K. Zhu, "Perovskite ink with wide processing window for scalable high-efficiency solar cells," *Nat. Energy*, vol. 2, p. 17038, 2017.

[24] Y. Jiang, M. R. Leyden, L. Qiu, S. Wang, L. K. Ono, Z. Wu, E. J. Juarez-Perez, and Y. Qi, "Combination of hybrid CVD and cation exchange for upscaling Cs-substituted mixed cation perovskite solar cells with high efficiency and stability," *Adv. Funct. Mater.*, vol. 28, p. 1703835, 2017.

[25] M. Remeika, S. R. Raga, S. Zhang, and Y. Qi, "Transferrable optimization of spray-coated PbI_2 films for perovskite solar cell fabrication," *J. Mater. Chem. A*, vol. 5, pp. 5709–5718, 2017.

[26] N. L. Chang, A. W. Y. Ho-Baillie, P. A. Basore, T. L. Young, R. Evans, and R. J. Egan, "A manufacturing cost estimation method with uncertainty analysis and its application to perovskite on glass photovoltaic modules," *Prog. Photovolt.: Res. Appl.*, vol. 25, pp. 390–405, 2017.

[27] Y. Yang and J. You, "Make perovskite solar cells stable," *Nature*, vol. 544, pp. 155–156, 2017.

[28] T. Leijtens, G. E. Eperon, S. Pathak, A. Abate, M. M. Lee, and H. J. Snaith, "Overcoming ultraviolet light instability of sensitized TiO_2 with meso-superstructured organometal tri-halide perovskite solar cells," *Nat. Commun.*, vol. 4, p. 2885, 2013.

[29] S. K. Pathak, A. Abate, P. Ruckdeschel, B. Roose, K. C. Gödel, Y. Vaynzof, A. Santhala, S.-I. Watanabe, D. J. Hollman, N. Noel, A. Sepe, U. Wiesner, R. Friend, H. J. Snaith, and U. Steiner, "Performance and stability enhancement of dye-sensitized and perovskite solar cells by Al doping of TiO_2," *Adv. Funct. Mater.*, vol. 24, pp. 6046–6055, 2014.

[30] S. Ito, S. Tanaka, K. Manabe, and H. Nishino, "Effects of surface blocking layer of Sb_2S_3 on nanocrystalline TiO_2 for $CH_3NH_3PbI_3$ perovskite solar cells," *J. Phys. Chem. C*, vol. 118, pp. 16995–17000, 2014.

[31] B. Roose, J.-P. C. Baena, K. C. Gödel, M. Grätzel, A. Hagfeldt, U. Steiner, and A. Abate, "Mesoporous SnO_2 electron selective contact enables UV-stable perovskite solar cells," *Nano Energy*, vol. 30, pp. 517–522, 2016.

[32] J. A. Christians, P. A. Miranda Herrera, and P. V. Kamat, "Transformation of the excited state and photovoltaic efficiency of $CH_3NH_3PbI_3$ perovskite upon controlled exposure to humidified air," *J. Am. Chem. Soc.*, vol. 137, pp. 1530–1538, 2015.

[33] G. Niu, W. Li, F. Meng, L. Wang, H. Dong, and Y. Qiu, "Study on the stability of $CH_3NH_3PbI_3$ films and the effect of post-modification by aluminum oxide in all-solid-state hybrid solar cells," *J. Mater. Chem. A*, vol. 2, pp. 705–710, 2014.

[34] N. Aristidou, C. Eames, I. Sanchez-Molina, X. Bu, J. Kosco, M. Islam, and S. Haque, "Fast oxygen diffusion and iodide defects mediate oxygen-induced degradation of perovskite solar cells," *Nat. Commun.*, vol. 8, p. 15215, 2017.

[35] F. Bella, G. Griffini, J.-P. Correa-Baena, G. Saracco, M. Grätzel, A. Hagfeldt, S. Turri, and C. Gerbaldi, "Improving efficiency and stability of perovskite solar cells with photocurable fluoropolymers," *Science*, vol. 354, pp. 203–206, 2016.

[36] I. Hwang, I. Jeong, J. Lee, M. J. Ko, and K. Yong, "Enhancing stability of perovskite solar cells to moisture by the facile hydrophobic passivation," *ACS Appl. Mater. Interfaces*, vol. 7, pp. 17330–17336, 2015.

[37] J. You, L. Meng, T.-B. Song, T.-F. Guo, Y. M. Yang, W.-H. Chang, Z. Hong, H. Chen, H. Zhou, Q. Chen, Y. Liu, N. D. Marco, and Y. Yang, "Improved air stability of perovskite solar cells via solution-processed metal oxide transport layers," *Nat. Nanotechnol.*, vol. 11, pp. 75–81, 2016.

[38] J. Yang, B. D. Siempelkamp, D. Liu, and T. L. Kelly, "Investigation of $CH_3NH_3PbI_3$ degradation rates and mechanisms in controlled humidity environments using *in situ* techniques," *ACS Nano*, vol. 9, pp. 1955–1963, 2015.

[39] T. Leijtens, G. E. Eperon, N. K. Noel, S. N. Habisreutinger, A. Petrozza, and H. J. Snaith, "Stability of metal halide perovskite solar cells," *Adv. Energy Mater.*, vol. 5, p. 1500963, 2015.

[40] Y. Lin, Y. Bai, Y. Fang, Z. Chen, S. Yang, X. Zheng, S. Tang, Y. Liu, J. Zhao, and J. Huang, "Enhanced thermal stability in perovskite solar cells by assembling 2D/3D stacking structures," *J. Phys. Chem. Lett.*, vol. 9, pp. 654–658, 2018.

[41] J. A. Schwenzer, L. Rakocevic, R. Gehlhaar, T. Abzieher, S. Gharibzadeh, S. Moghadamzadeh, A. Quintilla, B. S. Richards, U. Lemmer, and U. W. Paetzold, "Temperature variation-induced performance decline of perovskite solar cells," *ACS Appl. Mater. Interfaces*, vol. 10, pp. 16390–16399, 2018.

[42] S. Nagane, D. Ghosh, R. L. Z. Hoye, B. Zhao, S. Ahmad, A. B. Walker, M. S. Islam, S. Ogale, and A. Sadhanala, "Lead-free perovskite semiconductors based on germanium–tin solid solutions: Structural and optoelectronic properties," *J. Phys. Chem. C*, vol. 122, pp. 5940–5947, 2018.

[43] V. Goldschmidt, "Die gesetze der krystallochemie," *Naturwissenschaften*, vol. 14, pp. 477–485, 1926.

[44] G. Kieslich, S. Sun, and A. K. Cheetham, "Solid-state principles applied to organic–inorganic perovskites: new tricks for an old dog," *Chem. Sci.*, vol. 5, pp. 4712–4715, 2014.

[45] D. Ghosh, P. Walsh Atkins, M. S. Islam, A. B. Walker, and C. Eames, "Good vibrations: Locking of octahedral tilting in mixed-cation iodide perovskites for solar cells," *ACS Energy Lett.*, vol. 2, pp. 2424–2429, 2017.

[46] D. Ghosh, A. R. Smith, A. B. Walker, and M. S. Islam, "Mixed A-cation perovskites for solar cells: Atomic-scale insights into structural distortion, hydrogen bonding, and electronic properties," *Chem. Mater.*, 2018.

[47] S. R. Pering, W. Deng, J. R. Troughton, P. S. Kubiak, D. Ghosh, R. G. Niemann, F. Brivio, F. E. Jeffrey, A. B. Walker, M. S. Islam, T. M. Watson, P. R. Raithby, A. L. Johnson, S. E. Lewis, and P. J. Cameron, "Azetidinium lead iodide for perovskite solar cells," *J. Mater. Chem. A*, vol. 5, pp. 20658–20665, 2017.

[48] H. J. Snaith, A. Abate, J. M. Ball, G. E. Eperon, T. Leijtens, N. K. Noel, S. D. Stranks, J. T.-W. Wang, K. Wojciechowski, and W. Zhang, "Anomalous hysteresis in perovskite solar cells," *J. Phys. Chem. Lett.*, vol. 5, pp. 1511–1515, 2014.

[49] G. E. Eperon, R. J. S. Giuseppe M. Paternò, A. A. H. Andrea Zampetti, F. Cacialli, and H. J. Snaith, "Inorganic caesium lead iodide perovskite solar cells," *J. Mater. Chem. A*, vol. 3, pp. 19688–19695, 2015.

[50] J. Beilsten-Edmands, G. E. Eperon, R. D. Johnson, H. J. Snaith, and P. G. Radaelli, "Non-ferroelectric nature of the conductance hysteresis in $CH_3NH_3PbI_3$ perovskite-based photovoltaic devices," *Appl. Phys. Lett.*, vol. 106, p. 173502, 2015.

[51] C. Eames, J. M. Frost, P. R. F. Barnes, B. C. O'Regan, A. Walsh, and M. S. Islam, "Ionic transport in hybrid lead iodide perovskite solar cells," *Nat. Commun.*, vol. 6, p. 7497, 2015.

[52] A. Walsh, D. O. Scanlon, S. Chen, X. G. Gong, and S.-H. Wei, "Self-regulation mechanism for charged point defects in hybrid halide perovskites," *Angew. Chem. Int. Ed.*, vol. 127, p. 1811, 2015.

[53] S. Meloni, T. Moehl, W. Tress, M. Franckevičius, M. Saliba, Y. H. Lee, P. Gao, M. K. Nazeeruddin, S. M. Zakeeruddin, U. Rothlisberger, and M. Grätzel, "Ionic polarization-induced current-voltage hysteresis in $CH_3NH_3PbX_3$ perovskite solar cells," *Nat. Commun.*, vol. 7, p. 10334, 2016.

[54] J. Haruyama, K. Sodeyama, L. Han, and Y. Tateyama, "First-principles study of ion diffusion in perovskite solar cell sensitizers," *J. Am. Chem. Soc.*, vol. 137, pp. 10048–10051, 2015.

[55] A. Senocrate, I. Moudrakovski, G. Y. Kim, T. Yang, G. Gregori, M. Grätzel, and J. Maier, "The nature of ion conduction in methylammonium lead iodide: A multimethod approach," *Angew. Chem. Int. Ed.*, vol. 56, pp. 7755–7759, 2017.

[56] H. Yuan, E. Debroye, K. Janssen, H. Naiki, C. Steuwe, G. Lu, M. Moris, E. Orgiu, H. Uji-i, F. D. Schryver, P. Samorì, J. Hofkens, and M. Roeffaers, "Degradation of methylammonium lead iodide perovskite structures through light and electron beam driven ion migration," *J. Phys. Chem. Lett.*, vol. 7, pp. 561–566, 2016.

[57] K. Domanski, B. Roose, T. Matsui, M. Saliba, S.-H. Turren-Cruz, J.-P. Correa-Baena, C. R. Carmona, G. Richardson, J. M. Foster, F. De Angelis, J. M. Ball, A. Petrozza, N. Mine, M. K. Nazeeruddin, W. Tress, M. Grätzel, U. Steiner, A. Hagfeldt, and A. Abate, "Migration of cations induces reversible performance losses over day/night cycling in perovskite solar cells," *Energy Environ. Sci.*, vol. 10, pp. 604–613, 2017.

[58] J. Zhao, Y. Deng, H. Wei, X. Zheng, Z. Yu, Y. Shao, J. E. Shield, and J. Huang, "Strained hybrid perovskite thin films and their impact on the intrinsic stability of perovskite solar cells," *Sci. Adv.*, vol. 3, 2017.

[59] G. Richardson, S. E. J. O'Kane, R. G. Niemann, T. A. Peltola, J. M. Foster, P. J. Cameron, and A. B. Walker, "Can slow-moving ions explain hysteresis in the current-voltage curves of perovskite solar cells?," *Energy Environ. Sci.*, vol. 9, pp. 1476–1485, 2016.

[60] P. Calado, A. M. Telford, D. Bryant, X. Li, J. Nelson, B. C. O'Regan, and P. R. Barnes, "Evidence for ion migration in hybrid perovskite solar cells with minimal hysteresis," *Nat. Commun.*, vol. 7, p. 13831, 2016.

[61] J. O'Dwyer, *The Theory of Electrical Conduction and Breakdown in Solid Dielectrics*. Clarendon Press, Oxford, 1973.

[62] D. W. Miller, G. E. Eperon, E. T. Roe, C. W. Warren, H. J. Snaith, and M. C. Lonergan, "Defect states in perovskite solar cells associated with hysteresis and performance," *Applied Physics Letters*, vol. 109, p. 153902, 2016.

[63] N. Aristidou, I. Sanchez-Molina, T. Chotchuangchutchaval, M. Brown, L. Martinez, T. Rath, and S. A. Haque, "The role of oxygen in the degradation of methylammonium lead trihalide perovskite photoactive layers," *Angew. Chem. Int. Ed.*, vol. 54, pp. 8208–8212, 2015.

[64] S. van Reenen, M. Kemerink, and H. J. Snaith, "Modeling anomalous hysteresis in perovskite solar cells," *J. Phys. Chem. Lett*, vol. 6, pp. 3808–3814, 2015.

[65] D. A. Jacobs, Y. Wu, H. Shen, C. Barugkin, F. J. Beck, T. P. White, K. Weber, and K. R. Catchpole, "Hysteresis phenomena in perovskite solar cells: the many and varied effects of ionic accumulation," *Phys. Chem. Chem. Phys.*, vol. 19, pp. 3094–3103, 2017.

[66] F. Brivio, K. T. Butler, A. Walsh, and M. van Schilfgaarde, "Relativistic quasiparticle self-consitent electronic structure of hybride halide perovskite photovoltaic absorbers," *Phys. Rev. B*, vol. 89, p. 155204, 2014.

[67] C. C. Stoumpos, C. D. Malliakas, and M. G. Kanatzidis, "Semiconducting tin and lead iodide perovskites with organic cations: Phase transitions, high mobilities, and near-infrared photoluminescent properties," *Inorg. Chem.*, vol. 52, pp. 9019–9038, 2013.

[68] P. Schulz, E. Edri, S. Kirmayer, G. Hodes, D. Cahen, and A. Kahn, "Interface energetics in organo-metal halide perovskite-based photovoltaic cells," *Energy Environ. Sci.*, vol. 7, pp. 1377–1381, 2014.

[69] P. Löper, M. Stuckelberger, B. Niesen, J. Werner, M. Filipič, S.-J. Moon, J.-H. Yum, M. Topič, S. De Wolf, and C. Ballif, "Complex refractive index spectra of $CH_3NH_3PbI_3$ perovskite thin films determined by spectroscopic ellipsometry and spectrophotometry," *J. Phys. Chem. Lett.*, vol. 6, pp. 66–71, 2015.

[70] D. W. deQuilettes, W. Zhang, V. M. Burlakov, D. J. Graham, T. Leijtens, A. Osherov, V. Bulović, H. J. Snaith, D. S. Ginger, and S. D. Stranks, "Photo-induced halide redistribution in organic–inorganic perovskite films," *Nat. Commun.*, vol. 7, p. 11683, 2016.

[71] E. Jones, T. Oliphant, P. Peterson, *et al.*, "SciPy: Open source scientific tools for Python," 2001. Online; accessed 2018-06-06.

[72] L. F. Shampine and M. W. Reichelt, "The MATLAB ODE suite," *SIAM J. Sci. Comput.*, vol. 18, pp. 1–22, 1997.

[73] MathWorks, Inc., "MATLAB online documentation for the `ode15s` solver," 2018.

[74] L. F. Shampine, M. W. Reichelt, and J. A. Kierzenka, "Solving index-1 DAEs in MATLAB and Simulink," *SIAM Rev.*, vol. 41, pp. 538–552, 1999.

[75] L. F. Shampine, "Ill-conditioned matrices and the integration of stiff ODEs," *J. Comput. Appl. Math.*, vol. 48, pp. 279–292, 1993.

[76] G. E. Forsythe and C. B. Moler, *Computer Solution of Linear Algebraic Systems*. Prentice-Hall, 1967.

[77] G. B. Arfken and H. J. Weber, *Mathematical Methods for Physicists*. Academic Press, 4 ed., 1995.

[78] Advanpix LLC, "Multiprecision Computing Toolbox for MATLAB."

[79] M. T. Weller, O. J. Weber, P. F. Henry, A. M. Di Pumpo, and T. C. Hansen, "Complete structure and cation orientation in the perovskite photovoltaic methylammonium lead iodide between 100 and 352 K," *Chem. Commun.*, vol. "51, pp. 4180–4183, 2015.

[80] D. Bryant, S. Wheeler, B. C. O'Regan, T. Watson, P. R. Barnes, D. Worsley, and J. Durrant, "Observable hysteresis at low temperature in "hysteresis free" organic-inorganic lead halide perovskite solar cells," *J. Phys. Chem. Lett.*, vol. 6, pp. 3190–3194, 2015.

[81] I. Levine, P. K. Nayak, J. T.-W. Wang, N. Sakai, S. Van Reenen, T. M. Brenner, S. Mukhopadhyay, H. J. Snaith, G. Hodes, and D. Cahen, "Interface-dependent ion migration/accumulation controls hysteresis in $MAPbI_3$ solar cells," *J. Phys. Chem. C*, vol. 120, pp. 16399–16411, 2016.

[82] W. Zhang, S. Pathak, N. Sakai, T. Stergiopoulos, P. K. Nayak, N. K. Noel, A. A. Haghighirad, V. M. Burlakov, D. W. deQuilettes, A. Sadhanala, W. Li, L. Wang, D. S. Ginger, R. H. Friend, and H. J. Snaith, "Enhanced optoelectronic quality of perovskite thin films with hypophosphorous acid for planar heterojunction solar cells," *Nat. Commun.*, vol. 6, p. 10030, 2015.

[83] B. Wang, K. Y. Wong, S. Yang, and T. Chen, "Crystallinity and defect state engineering in organo-lead halide perovskite for high-efficiency solar cells," *J. Mater. Chem. A*, vol. 4, pp. 3806–3812, 2016.

[84] N. K. Noel, A. Abate, S. D. Stranks, E. S. Parrott, V. M. Burlakov, A. Goriely, and H. J. Snaith, "Enhanced photoluminescence and solar cell performance via lewis base passivation of organic-inorganic lead halide perovskites," *ACS Nano*, vol. 8, pp. 9815–9821, 2014.

[85] C. Roldan-Carmona, P. Gratia, I. Zimmermann, G. Grancini, P. Gao, M. Graetzel, and M. K. Nazeeruddin, "High efficiency methylammonium lead triiodide perovskite solar cells: the relevance of non-stoichiometric precursors," *Energy Environ. Sci.*, vol. 8, pp. 3550–3556, 2015.

[86] M. Saliba, T. Matsui, J.-Y. Seo, K. Domanski, J.-P. Correa-Baena, M. K. Nazeeruddin, S. M. Zakeeruddin, W. Tress, A. Abate, A. Hagfeldt, and M. Grätzel, "Cesium-containing triple cation perovskite solar cells: improved stability, reproducibility and high efficiency," *Energy Environ. Sci.*, vol. 9, pp. 1989–1997, 2016.

[87] S. D. Stranks, G. E. Eperon, G. Grancini, C. Menelaou, M. J. P. Alcocer, T. Leijtens, L. M. Herz, A. Petrozza, and H. J. Snaith, "Electron-hole diffusion lengths exceeding 1 micrometer in an organometal trihalide perovskite absorber," *Science*, vol. 342, pp. 341–344, 2013.

[88] W. Nie, H. Tsai, R. Asadpour, J.-C. Blancon, A. J. Neukirch, G. Gupta, J. J. Crochet, M. Chhowalla, S. Tretiak, M. A. Alam, H.-L. Wang, and A. D. Mohite, "High-efficiency solution-processed perovskite solar cells with millimeter-scale grains," *Science*, vol. 347, pp. 522–525, 2015.

[89] S. A. L. Weber, I. M. Hermes, S.-H. Turren-Cruz, C. Gort, V. W. Bergmann, L. Gilson, A. Hagfeldt, M. Graetzel, W. Tress, and R. Berger, "How the formation of interfacial charge causes hysteresis in perovskite solar cells," *Energy Environ. Sci.*, 2018.

[90] T. W. Jones, A. Osherov, M. Alsari, M. Sponseller, B. C. Duck, Y.-K. Jung, C. Settens, F. Niroui, R. Brenes, C. V. Stan, Y. Li, M. Abdi-Jalebi, N. Tamura, J. E. Macdonald, M. Burghammer, R. H. Friend, V. Bulović, A. Walsh, G. J. Wilson, S. Lilliu, and S. D. Stranks, "Local strain heterogeneity influences the optoelectronic properties of halide perovskites," 2018.

[91] B. Charles, J. Dillon, O. J. Weber, M. S. Islam, and M. T. Weller, "Understanding the stability of mixed A-cation lead iodide perovskites," *J. Mater. Chem. A*, vol. 5, pp. 22495–22499, 2017.

[92] S. Olthof and K. Meerholz, "Substrate-dependent electronic structure and film formation of $MAPbI_3$ perovskites," *Sci. Rep.*, vol. 7, p. 40267, 2017.

[93] M. Scharber and N. Sariciftci, "Efficiency of bulk-heterojunction organic solar cells," *Prog. Polym. Sci.*, vol. 38, pp. 1929–1940, 2013.

[94] P. Cheng and X. Zhan, "Stability of organic solar cells: challenges and strategies," *Chem. Soc. Rev.*, vol. 45, pp. 2544–2582, 2016.

[95] G. Chamberlain, "Organic solar cells: A review," *Sol. Cells*, vol. 8, pp. 47–83, 1983.

[96] M. Jørgensen, K. Norrman, and F. C. Krebs, "Stability/degradation of polymer solar cells," *Sol. Energy Mater. Sol. Cells*, vol. 92, pp. 686–714, 2008.

[97] B. Azzopardi, C. J. M. Emmott, A. Urbina, F. C. Krebs, J. Mutale, and J. Nelson, "Economic assessment of solar electricity production from organic-based photovoltaic modules in a domestic environment," *Energy Environ. Sci.*, vol. 4, pp. 3741–3753, 2011.

[98] H. Hoppe and N. S. Sariciftci, "Organic solar cells: An overview," *J. Mater. Res.*, vol. 19, pp. 1924–1945, 2004.

[99] M. Pope and C. Swenberg, *Electronic processes in organic crystals*. Oxford University Press, 1982.

[100] E. Salpeter and H. Bethe, "A relativistic equation for bound-state problems," *Phys. Rev.*, vol. 84, pp. 1232–1242, 1951.

[101] M. Rohlfing and S. G. Louie, "Electron-hole excitations and optical spectra from first principles," *Phys. Rev. B*, vol. 62, pp. 4927–4944, 2000.

[102] M. Dvorak, S.-H. Wei, and Z. Wu, "Origin of the variation of exciton binding energy in semiconductors," *Phys. Rev. Lett.*, vol. 110, p. 016402, 2013.

[103] M. Knupfer and J. Fink, "Size and dispersion of excitons in organic semiconductors," *Synth. Met.*, vol. 141, pp. 21–27, 2004.

[104] B. A. Gregg, "Excitonic solar cells," *J. Phys. Chem. B*, vol. 107, pp. 4688–4698, 2003.

[105] P. W. Blom, V. D. Mihailetchi, L. J. A. Koster, and D. E. Markov, "Device physics of polymer:fullerene bulk heterojunction solar cells," *Adv. Mater.*, vol. 19, pp. 1551–1566, 2007.

[106] B. A. Gregg and M. C. Hanna, "Comparing organic to inorganic photovoltaic cells: Theory, experiment, and simulation," *J. Appl. Phys*, vol. 93, pp. 3605–3614, 2003.

[107] M. Knupfer, "Exciton binding energies in organic semiconductors," *Appl. Phys. A*, vol. 77, pp. 623–626, 2003.

[108] P. Peumans and S. R. Forrest, "Separation of geminate charge-pairs at donor-acceptor interfaces in disordered solids," *Chem. Phys. Lett.*, vol. 398, pp. 27–31, 2004.

[109] A. Liu, S. Zhao, S.-B. Rim, J. Wu, M. Könemann, P. Erk, and P. Peumans, "Control of electric field strength and orientation at the donor-acceptor interface in organic solar cells," *Adv. Mater.*, vol. 20, pp. 1065–1070, 2003.

[110] K. Feron, W. J. Belcher, C. J. Fell, and P. C. Dastoor, "Organic solar cells: Understanding the role of Förster resonance energy transfer," *Int. J. Mol. Sci.*, vol. 13, pp. 17019–17047, 2012.

[111] C. Tang, "Two-layer organic photovoltaic cell," *Appl. Phys. Lett.*, vol. 48, pp. 183–185, 1986.

[112] N. S. Sariciftci, L. Smilowitz, A. J. Heeger, and F. Wudl, "Photoinduced electron transfer from a conducting polymer to buckminsterfullerene," *Science*, vol. 258, pp. 1474–1476, 1992.

[113] A. A. Bakulin, A. Rao, V. G. Pavelyev, P. H. M. van Loosdrecht, M. S. Pshenichnikov, D. Niedzialek, J. Cornil, D. Beljonne, and R. H. Friend, "The role of driving energy and delocalized states for charge separation in organic semiconductors," *Science*, vol. 335, pp. 1340–1344, 2012.

[114] P. K. Nayak, K. L. Narasimhan, and D. Cahen, "Separating charges at organic interfaces: Effects of disorder, hot states, and electric field," *J. Phys. Chem. Lett.*, vol. 4, pp. 1707–1717, 2013.

[115] J.-L. Brédas, J. E. Norton, J. Cornil, and V. Coropceanu, "Molecular understanding of organic solar cells: The challenges," *Acc. Chem. Res.*, vol. 42, pp. 1691–1699, 2009.

[116] C. Deibel, T. Strobel, and V. Dyakonov, "Role of the charge transfer state in organic donor-acceptor solar cells," *Adv. Mater.*, vol. 22, pp. 4097–4111, 2010.

[117] S. H. Park, A. Roy, S. Beaupré, S. Cho, N. Coates, J. S. Moon, D. Moses, M. Leclerc, K. Lee, and A. J. Heeger, "Bulk heterojunction solar cells with internal quantum efficiency approaching 100%," *Nat. Photon.*, vol. 3, pp. 297–302, 2009.

[118] B. C. Thompson and J. M. Fréchet, "Polymer-fullerene composite solar cells," *Angew. Chem. Int. Ed.*, vol. 47, pp. 58–77, 2007.

[119] A. Facchetti, "π-conjugated polymers for organic electronics and photovoltaic cell applications," *Chem. Mater.*, vol. 23, pp. 733–758, 2011.

[120] T. Förster, "Transfer mechanisms of electronic excitation energy," *Radiat. Res. Suppl.*, vol. 2, pp. 326–339, 1960.

[121] A. R. Clapp, I. L. Medintz, and H. Mattoussi, "Förster resonance energy transfer investigations using quantum-dot fluorophores," *ChemPhysChem*, vol. 7, pp. 47–57, 2006.

[122] G. D. Scholes, "Long-range resonance energy transfer in molecular systems," *Annu. Rev. Phys. Chem.*, vol. 54, pp. 57–87, 2003.

[123] L. M. Loura, "Simple estimation of Förster resonance energy transfer (FRET) orientation factor distribution in membranes," *Int. J. Mol. Sci.*, vol. 13, pp. 15252–15270, 2012.

[124] R. R. Lunt, N. C. Giebink, A. A. Belak, J. B. Benziger, and S. R. Forrest, "Exciton diffusion lengths of organic semiconductor thin films measured by spectrally resolved photoluminescence quenching," *J. Appl. Phys.*, vol. 105, p. 053711, 2009.

[125] R. Marsh, C. Groves, and N. Greenham, "A microscopic model for the behavior of nanostructured organic photovoltaic devices," *J. Appl. Phys.*, vol. 101, p. 083509, 2007.

[126] P. K. Watkins, A. B. Walker, and G. L. B. Verschoor, "Dynamical monte carlo modelling of organic solar cells: The dependence of internal quantum efficiency on morphology," *Nano Lett.*, vol. 5, pp. 1814–1818, 2005.

[127] D. Veldman, S. C. J. Meskers, and R. A. J. Janssen, "The energy of charge-transfer states in electron donor–acceptor blends: Insight into the energy losses in organic solar cells," *Adv. Funct. Mater.*, vol. 19, pp. 1939–1948, 2009.

[128] R. A. J. Janssen and J. Nelson, "Factors limiting device efficiency in organic photovoltaics," *Adv. Mater.*, vol. 25, pp. 1847–1858, 2013.

[129] S. Honda, H. Ohkita, H. Benten, and S. Ito, "Selective dye loading at the heterojunction in polymer/fullerene solar cells," *Adv. Energy Mater.*, vol. 1, pp. 588–598, 2011.

[130] J.-S. Huang, T. Goh, X. Li, M. Y. Sfeir, E. A. Bielinski, S. Tomasulo, M. L. L. amd Nilay Hazari, and A. D. Taylor, "Polymer bulk heterojunction solar cells employing Förster resonance energy transfer," *Nat. Photon.*, vol. 7, pp. 479–485, 2013.

[131] A. M. Brouwer, "Standards for photoluminescence quantum yield measurements in solution (IUPAC technical report)," *Pure Appl. Chem.*, vol. 83, pp. 2213–2228, 2011.

[132] P. E. Shaw, A. Ruseckas, and I. D. W. Samuel, "Exciton diffusion measurements in poly(3-hexylthiophene)," *Adv. Mater.*, vol. 20, pp. 3516–3520, 2008.

[133] Q. An, F. Zhang, L. Li, J. Wang, J. Zhang, L. Zhou, and W. Tang, "Improved efficiency of bulk heterojunction polymer solar cells by doping low-bandgap small molecules," *ACS Appl. Mater. Interfaces*, vol. 6, pp. 6537–6544, 2014.

[134] H. Wang, Y. He, Y. Li, and H. Su, "Photophysical and electronic properties of five PCBM-like C_{60} derivatives: Spectral and quantum chemical view," *J. Phys. Chem. A*, vol. 116, pp. 255–262, 2012.

[135] S. Cook, A. Furube, R. Katoh, and L. Han, "Estimate of singlet diffusion lengths in PCBM films by time-resolved emission studies," *Chem. Phys. Lett.*, vol. 478, pp. 33–36, 2009.

[136] G. Wei, X. Xiao, S. Wang, K. Sun, K. J. Bergemann, M. E. Thompson, and S. R. Forrest, "Functionalized squaraine donors for nanocrystalline organic photovoltaics," *ACS Nano*, vol. 6, pp. 972–978, 2012.

[137] D. C. Coffey, B. W. Larson, A. W. Hains, J. B. Whitaker, N. Kopidakis, O. V. Boltalina, S. H. Strauss, and G. Rumbles, "An optimal driving force for converting excitons into free carriers in excitonic solar cells," *J. Phys. Chem. C*, vol. 116, pp. 8916–8923, 2012.

[138] K. Feron, X. Zhou, W. J. Belcher, and P. C. Dastoor, "Exciton transport in organic semiconductors: Förster resonance energy transfer compared with a simple random walk," *J. Appl. Phys.*, vol. 111, p. 044510, 2012.

[139] S. Cook, R. Katoh, and A. Furube, "Exciton splitting in nanoscale phase-separated polythiophene:fullerene solar cell blends," *J. Nanoelectron. Optoelectron.*, vol. 5, pp. 115–119, 2010.

[140] J. Piris, T. E. Dykstra, A. A. Bakulin, P. H. van Loosdrecht, W. Knulst, M. T. Trinh, J. M. Schins, and L. D. Siebbeles, "Photogeneration and ultrafast dynamics of excitons and charges in P3HT/PCBM blends," *J. Phys. Chem. C*, vol. 113, pp. 14500–14506, 2009.

[141] R. Kroon, A. Diaz de Zerio Mendaza, S. Himmelberger, J. Bergqvist, O. Bäcke, G. C. Faria, F. Gao, A. Obaid, W. Zhuang, D. Gedefaw, E. Olsson, O. Inganäs, A. Salleo, C. Müller, and M. R. Andersson, "A new tetracyclic lactam building block for thick, broad-bandgap photovoltaics," *J. Am. Chem. Soc.*, vol. 136, pp. 11578–11581, 2014.